Compensator Design for Model-in-the-Loop Testing

Hu, Jiayang

Award date:
2017

Awarding institution:
University of Bath

Compensator Design for Model-in-the-Loop Testing

Submitted by

Jiayang Hu

A thesis submitted for the degree of Doctor of Philosophy

University of Bath

Department of Mechanical Engineering

November 2017

COPYRIGHT

Abstract

Model-in-the-Loop (MiL) testing is a method in which the test object is split into a physical part and a simulated part, and these are connected with interfaces to form a combined physical-numerical system. It is introduced to combine the advantages of physical test and computer simulation: the part of the system which is difficult to implement physically can be put into the numerical subsystem to reduce the cost and complexity of the physical test, and the key components with unknown characteristics or with some characteristics which are difficult to model can form the physical subsystem. The simulated part also provides the flexibility to change the parameters during the test.

In this thesis, the structure and the characteristics of MiL systems are analysed. Detailed results are given using two example systems: a single mass-spring-damper MiL system, and a two Degree of Freedom (DOF) mass-spring-damper MiL system. The systems are defined, and a procedure for stability analysis is given. The influence of the actuator dynamics and the measurement noise introduced by the sensors is discussed. To compensate for the actuator dynamics, compensators are introduced to the MiL system. It is shown with simulation results that, when a compensator based on an inverse of the actuator dynamics is added to the MiL system, the high frequency measurement noise may be greatly amplified in the compensated signal, and therefore signal saturation may occur which leads to unacceptable testing results.

To design a compensator which can effectively compensate for the actuator dynamics, while reducing the tendency of signal saturation in the compensated actuator control signal at the same time, H_∞ optimization is applied. A general model is composed for the H_∞ optimization, where the target testing result is compared with that of an ideal reference model, and the error between them is minimized via H_∞ loop shaping. The principle of H_∞ loop shaping is presented in the thesis, and its use as a general MiL optimization procedure is proposed. The optimization method is verified with the example one and two DOF mass-spring-damper MiL systems. The simulation results show that, for both of the examples, the H_∞ optimized compensator can compensate

for the actuator dynamics accurately, and attenuate the response excited by the measurement noise in the compensated signal effectively. The balance between accuracy and high frequency noise attenuation can be adjusted by the weighting functions.

The effectiveness of the H_∞ optimized compensator is then verified with experimental results. A two-axis robotic arm based on a limb of the Italian Institute of Technology HyQ robot was used for the experiment. The H_∞ optimized compensator is compared with various alternative compensators, and the H_∞ optimized compensator show its advantages in terms of an appropriate balance between accuracy and saturation rejection.

Lastly, a performance envelope analysis is introduced to give a guide to choosing suitable hydraulic actuators and valves for a specific MiL test based on the actuator performance required to give desired test accuracy. Although the H_∞ optimized compensator can broaden the usable frequency range of the valve/actuator system, and will provide a larger margin for control signal saturation, an effective test system is only achievable if an actuation system of adequate performance is chosen.

Acknowledgement

I would like to express my deepest gratitude to my supervisor Professor Andrew Plummer for all his advice and guidance during my PhD study, and I should say thanks for his kindness and patience on me.

Thanks to the technical staff in department of Mechanical Engineering, who have helped me a lot during the experiment.

Many thanks to my parents for their unconditional support.

Thanks to my colleagues and friends in 8E for their company in these years.

Contents

Nomenclature

Variables

Symbol	Description
A	The driving area of the actuator
A_1, A_2	The piston area and the annulus area respectively
$A(s)$	The transfer function of the actuator model
$A_1(s)$	The transfer function of the Multi-Axis Simulation Table
$A_2(s)$	The transfer function of the slowed down Multi-Axis Simulation Table
$A_p(s)$	The transfer function representing the actual dynamics of the valve-actuator combination
C	The damping coefficient of the damper in the single mass-spring-damper MiL system
C_1	The damping coefficient of the damper between the reference ground and the first mass in the two DOF mass-spring-damper MiL system
C_2	The damping coefficient of the damper between the first mass and the second mass in the two DOF mass-spring-damper MiL system
$C(s)$	The transfer function for the compensator
$C_1(s)$	The transfer function of the PID controller
D	The amplitude of the displacement of the shoulder actuator
e	The error between the reference displacement and the displacement with actuator and compensator model
F	The amplitude of the force measured by the load cell
F_f	The friction force
f	The force between the actuator and the physical mass
I_1, I_2, I_3	The inertia for the upper arm, the forearm, and the hand respectively (with respect to their own centres of gravity)
I_{11}, I_{22}, I_{33}	The inertia for the upper arm, the forearm, and the hand respectively (with respect to point P1)
I_t	The overall rotational inertia of the robot arm (with respect to point P1)
i	The input signal

K	The stiffness of the spring in the single mass-spring-damper MiL system
K_1	The stiffness of the spring between the reference ground and the first mass in the two DOF mass-spring-damper MiL system
K_2	The stiffness of the spring between the first mass and the second mass in the two DOF mass-spring-damper MiL system
L_1, L_2	The low pass filters in the weighting functions
M	The mass in the single mass-spring-damper MiL system
M_1	The first mass in the two DOF mass-spring-damper MiL system
M_2	The second mass in the two DOF mass-spring-damper MiL system
M_{r1}, M_{r2}, M_{r3}	The mass of the upper arm, the forearm, and the hand respectively
M_{eq}	The actual equivalent mass
M_t	The overall mass of the robotic arm
$N(s)$	The transfer function of the filter to describe the noise n
n	The measurement noise
n_1, n_2	The user defined parameters to adjust the balance of H_∞ optimization
P	The maximum pressure the valve/actuator system can achieve
P_1, P_2	The pressure at the piston side and the annulus side of the actuator respectively
P_r	The pressure at which the rated flow rate is measured
P_s	The supply pressure
P_{m1}, P_{m2}, P_{m3}	The coordinates of the centre of gravity of the upper arm, the forearm, and the hand respectively
$P_1(s)$, $P_2(s)$	The transfer functions for the physical subsystem
p	The force applied to the vertically stretched out robot arm from the shoulder actuator, in the direction of the motion of the actuator
Q	The maximum flow rate of the valve/actuator system
Q_1, Q_2	The flow rate at the piston side and the annulus side of the actuator respectively
Q_r	The rated flow rate of the hydraulic valve
R	The ratio of the piston area to the annulus area
$R(s)$	The transfer function from the input signal i to the demand position r
S	The full stroke of the actuator

$S_1(s)$, $S_2(s)$	The transfer functions for the numerical subsystem
$\mathbf{T}$	The transfer function of the system constructed for H∞ optimization
$\mathbf{T}_1$	The transfer function of the weighted system
$\mathbf{T}_{11}$	The transfer function from z_0 to e
$\mathbf{T}_{22}$	The transfer function from n to z_{1c}
$U_i(s)$	The transfer function from the input signal i to the signal u
$U_n(s)$	The transfer function from the measurement noise n to the control signal u
u	The control signal
V	The achievable velocity amplitude
v	The disturbance force
$\mathbf{W}_{11}$, $\mathbf{W}_{22}$	The weighting functions for $\mathbf{T}_{11}$ and $\mathbf{T}_{22}$ respectively
x	The displacement of the shoulder actuator
z_0	The displacement of the reference ground
z_1	The displacement of the mass in the single mass-spring-damper MiL system; the displacement of the first mass in the two DOF mass-spring-damper MiL system
z_2	The displacement of the second mass in the two DOF mass-spring-damper MiL system
z_{1d}	The desired displacement of the actuator
z_{1c}	The compensated signal
z_{2r}	The reference displacement
$\overline{z_1}$	The open loop response to input z_1

Greek Symbols

Symbol	Description
γ	The achieved minimum norm after the H_∞ optimization
$\overline{\gamma_{11}}$, $\overline{\gamma_{22}}$	The original H_∞ norms for $\mathbf{T}_{11}$ and $\mathbf{T}_{22}$ before the optimization
θ_1, θ_2	The angle of rotation from the upright location of the shoulder joint and elbow joint respectively

λ	The saturation level for the control signal u
τ_1, τ_2, τ_3	The time constants defining the transfer function of the actuator model
τ_n, τ_d	Additional time constants to define the order of the compensator
ω	The frequency of the motion

Chapter 1

1 Introduction

1.1 Introduction to Model-in-the-Loop Testing

Model-in-the-Loop (MiL) testing is a method in which the test object is split into a physical part and a simulated part, and these are connected with interfaces to form a combined physical-numerical system [1]. In reality, it is often necessary to test a newly designed object physically before manufacturing, because there's possibly some design errors or unknown characteristics not revealed by theoretical analysis. However, it is usually very costly and time consuming to physically test objects, especially when the scale of the testing object is very large, for example, testing an aeroplane or a building. Model-in-the-Loop testing is thus introduced to combine the advantages of physical test and simulation, where only the critical parts are tested physically, and the rest of the system remains in the simulation. In different disciplines, MiL testing has also been called actuator based Hardware-in-the-Loop (HiL) testing, real-time hybrid testing, or substructuring. However, the basic idea is the same.

The advantages of Model-in-the-Loop testing are:

1. The part of the system with known characteristics, or the part of the system which is very difficult to implement physically, can be replaced by a real-time simulation, thus the cost and complexity of the physical testing rig can be greatly reduced.
2. The key components with unknown characteristics or with some characteristics that are difficult to model can form the physical test subsystem.
3. The simulated subsystem gives the flexibility to change its parameters during the test, which is much more convenient than replacing real components in a physical subsystem.

For applications in civil engineering such as earthquake testing, there have been a number of research studies about the compensation of the characteristics of the actuator. In mechanical engineering, the research is more often about implementation.

1.2 Examples of Application

Plummer provides a general framework for modelling MiL systems in [1]. Sensors, actuators and the real-time computing platform all exhibit non-ideal behaviour, and will be the source of errors in the whole system. Usually, the actuator dynamics and sensor measurement noise are the most significant error sources. Two examples are given to demonstrate the MiL test applications. One example is the real-time aerodynamic model with a Formula One car test rig (as illustrated in Figure 1.1). The modelling assumptions are verified by experimental results. Another example is a real-time tyre model in a similar MiL test rig (as shown in Figure 1.2). For this example, however, the experimental results show significant error. The question has been raised whether it is possible to optimize the performance of the actuators, sensors and controller to make the error as small as possible.

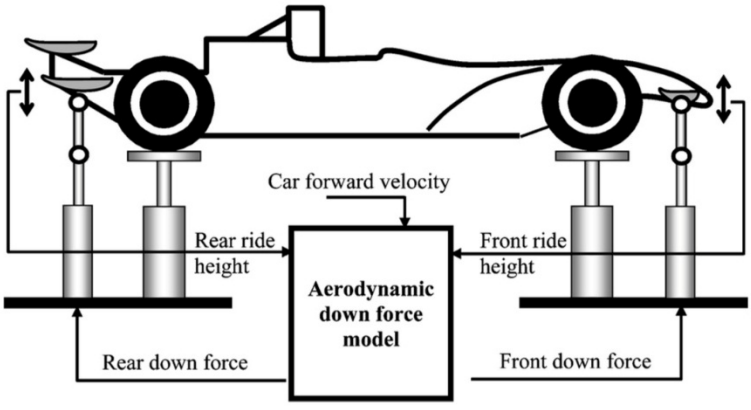

Figure 1.1 The aerodynamic MiL test for Formula One vehicle [1]

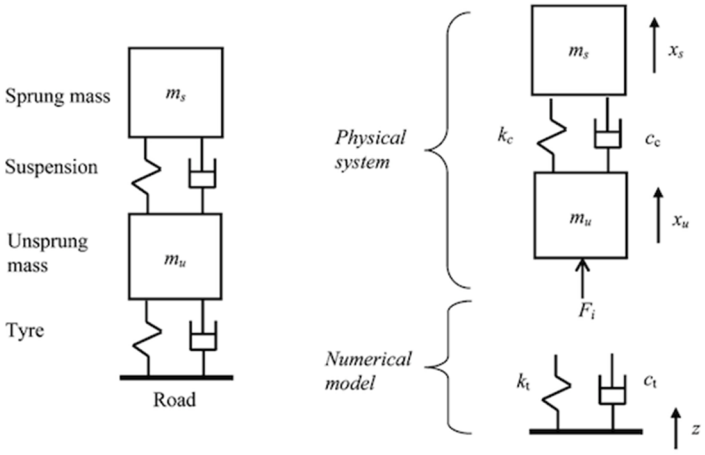

Figure 1.2 Tyre Model-in-the-Loop [1]

Fathy et al. reviewed the Hardware-in-the-Loop Simulation in the automotive area in [2]. In this review, the authors discussed the key utility of HiL simulation, before giving the applications of HiL simulation in automotive industry. The applications include helping the design of a hypothetical control system for a combined active/passive vehicle suspension, by way of testing the physical active suspension microcontroller against a virtual vehicle model to calibrate and validate it before real installation. Another application is to help to develop automotive brake and stability control systems. Such HiL systems do not required the addition of physical actuators and sensors to connect the physical and numerical parts and so do not suffer from the problems tackled in this thesis.

In [2], Fathy et al. also discussed the development of the Engine-in-the-Loop (EiL) simulation in which a physical engine system is tested in a virtual vehicle system. In such an arrangement, the application of sophisticated diagnostics are allowed, including ultra-fast emission analysers. The EiL simulation could provide detailed insight into the transient interactions between the powertrain components and their influence on transient emissions, but the actuation system required to apply the transmission torque onto the engine does present control problems in this case. The authors expect an increased application of HiL simulation for system design, and networked HiL simulation is predicted to be more used in the longer term.

Another application is in the area of aerospace industry. Montazeri-Gh et al. presented the structure and implementation of an actuator based HiL simulation for the test of a jet engine fuel control unit (FCU) in [3]. The system is built based on a sophisticated hydraulic test bench, and the actuator-based HiL simulation system creates operating conditions that are similar to real jet engine applications, in which the FCU performance can be tested.

In [4], Börner and Alam present one application example in ocean wave energy converters. Because pure simulation is very computationally costly, and pure physical experiment is limited by scaling difficulties and high cost, the authors investigate the hybrid testing method. The authors built the hybrid testing system based on a newly proposed wave energy conversion device called 'Wave Carpet'. In the testing system, the waves are emulated in the wave tank, thus the interaction of the 'Wave Carpet' and the waves is the physical part, and the power takeoff unit is modelled in the simulation part.

Chabaud provided an example of application in the testing of offshore floating wind turbines in [5]. As shown in Figure 1.3 [5], instead of testing the full scale system as illustrated in the left using the ocean wave basin and the wind tunnel at the same time, a real-time hybrid testing can be designed with a down-scaled (the scaling must be done according to the Froude number) floating chassis in the physical part and put into the ocean wave basin, and the aerodynamic loads are computationally simulated, Froude downscaled, and command the actuators to apply the forces to the chassis.

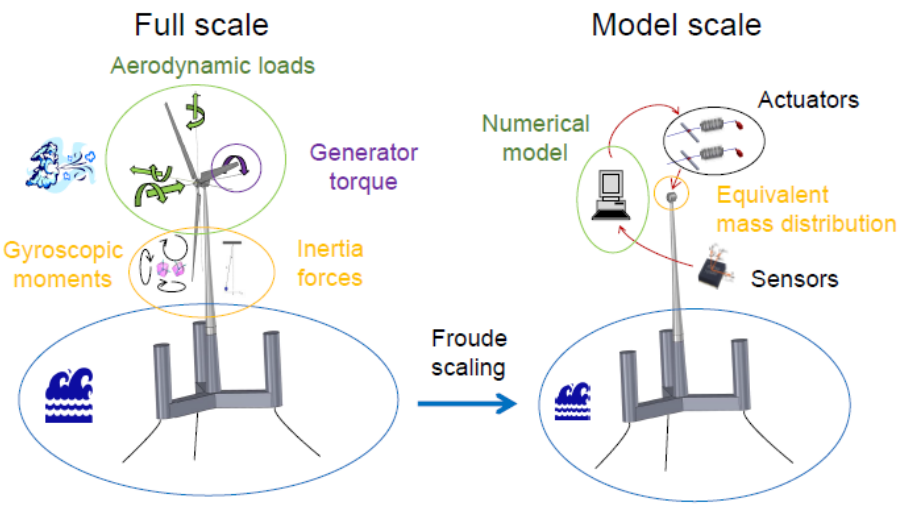

Figure 1.3 Concept of real-time hybrid model testing of a floating wind turbine [5]

1.3 Research Motivation

As demonstrated by the examples in Section 1.2, MiL testing can be applied in various areas, and it is a promising method by combining the advantages of computer simulation and physical testing.

In MiL testing, the whole test system is split in half, and connected back together. The "interface" between the physical part and the virtual part (including actuators and sensors) becomes the biggest source of disturbance and error, because:

1. Actuators naturally have some transfer dynamics. If the demand signal generated from the simulated subsystem is sent directly to the actuators, the displacement of the actuators will be inaccurate. To overcome the transfer dynamics of the actuators, a compensator needs to be added between the output of the simulated subsystem and the actuator to guarantee accurate test results.
2. In a MiL test system, sensors will measure the output from the physical subsystem, and feedback the signal to the simulated subsystem for simulation.

During this process, sensors will inevitably introduce measurement noise to the feedback signal, and the noise usually has very high frequency components. If a low-pass filter is added to filter out the high frequency measurement noise, the filter will introduce additional phase lag to the closed-loop system, which may affect the accuracy of the test results and the stability of the system.

3. The compensator may greatly amplify the high frequency signal in the closed-loop system (introduced by the measurement noise) due to the internal differentiation components in the compensator, and the amplified high frequency signal may lead to signal saturation problem. It's difficult to tune the balance between the accuracy of compensation and the ability of signal saturation denial. The requirements make the design of the compensator challenging.

In summary, a compensator is necessary in a MiL test system for more accurate test results, however, the measurement noise makes the compensator design challenging, because the problem of signal saturation may occur if the compensator is not designed properly. Hence a straight forward and effective method of compensator designing is much needed.

To solve the problem, a compensator designing scheme based on H_∞ loop shaping is proposed. The reasons for choosing the H_∞ loop shaping method is:

1. According to the design requirements, a general MiL system can be taken as a MIMO system: the demand signal and the measurement noise can be accounted as the 2 inputs, while the test result and the compensated signal taken as the 2 outputs. H_∞ loop shaping method can be easily applied to MIMO systems.
2. According to the design requirements, a balance needs to be achieved between the accuracy of the test results and the saturation denial ability in the compensated signal. These two requirements are easily translated to H_∞ loop shaping targets: optimize and balance the related transfer functions.

3. Because the 2 inputs of the system, the demand signal and the measurement noise usually have very different characteristics in frequency domain: the demand signal is generally in relatively low frequency range, while the measurement noise is mostly in a much higher frequency range, a lot of manipulations need to be done in the frequency domain. Because the nature of H_∞ loop shaping method is based on analysis in frequency domain, and the balance of the optimization can be simply adjusted by tuning the gains and the shapes of the weighting functions, H_∞ loop shaping scheme is perfect to be applied in this case.

And lastly, because there hasn't been any research about choosing suitable actuators for a specific MiL test yet, it is important to give an insight into this topic. In this thesis, performance envelope is introduced. The reason of applying performance envelope for the selection of actuators is that, the performance envelope is basically a graph showing the maximum speed an actuator can achieve in different frequency ranges, it could be directly compared to the velocity requirements for a specific MiL test.

1.4 Original Contribution

In this thesis, a general procedure for analysing and implementing a MiL test is proposed. The original contribution is summarized as follows:

1. The structure and the characteristics of MiL systems are analysed. In the analysis, the method of building a MiL test system based on the mathematical model of the whole system is shown. The process of stability analysis is presented, and the problems introduced by the actuator dynamics and measurement noise are examined.
2. A compensator design approach based on H_∞ loop shaping is presented. For the optimization, a two-input two-output system is constructed, with the unique

structure of comparing the target testing result and that of the ideal reference model. The effectiveness of the optimized compensator is verified by both simulation and MiL test.

3. A general approach is introduced to give a guide about choosing suitable hydraulic actuators and valves for a specific MiL test based on the performance envelope of the valve/actuator system and the maximum control signal level.

1.5 Structure of the Thesis

Chapter 1 is the introduction. The concept of Model-in-the-Loop testing is explained, and the motivation for the research is given. For better understanding of MiL testing, some examples of the application of MiL testing in different areas are provided.

Chapter 2 presents the literature review of the Model-in-the-Loop testing, including the first introduction of the concept, the analysis of the problems caused by the nature of MiL testing, and various ways of compensating for the lag in the system.

Chapter 3 presents the analysis of the MiL systems. The characteristics of the MiL testing systems are analysed using simplified mass-spring damper examples. The stability of the MiL systems and the influence of measurement noise and disturbances are analysed in this chapter.

Chapter 4 introduces the compensator design method with H_∞ optimization. In this chapter, the principles for the application of H_∞ optimization in the design of the controller in the MiL system are given, and an example of the optimization process is shown with MATLAB/Simulink.

Chapter 5 presents the experiment verification of the H_∞ optimized compensator. A realistic MiL testing system is generated with a robot arm, and the effectiveness of the

H_∞ optimized compensator is verified using the testing rig, and compared with other type of compensators.

Chapter 6 investigates the performance envelope of the valve/actuator system, and the method of determining whether a valve/actuator system is viable for a defined MiL test, with the assistance of the performance envelope and the control signal saturation level.

Chapter 7 is the conclusion of the thesis.

Chapter 2

2 Literature Review

In this chapter, an overview of the remarkable research in the area of MiL testing is provided, and it is also pointed out that there's a lack of research in some important topics in the area of MiL testing, leading to the motivation of the research presented in this thesis.

2.1 Early research on MiL systems

Horiuchi et al. described the problem of actuator lag in hybrid testing in [6]. All the analysis and conclusions are based on the assumption that the dynamics of the actuator in the hybrid testing system is a pure time delay. The time delay of the actuator is compared to a negative damping c_{eq} in the system; the equivalent negative damping is shown as follows (k is the stiffness of the spring, and δt is the actuator delay):

$$c_{eq} = -k\delta t \tag{2.1}$$

If the value of the negative damping gets higher than the inherent structural damping, the testing system will go unstable.

Horiuchi et al. then proposed a simple algorithm to compensate for the characteristics of the actuator, by first predicting the displacement of the actuator after the response delay time, then modifying the prediction parameters to match the realistic conditions.

The predicted value x' (the displacement after the actuator delay time, and is used as the control signal to the actuator) was calculated by extrapolating an nth order polynomial function. The equation is shown as follows:

$$x' = \sum_{i=0}^{n} a_i x_i \tag{2.2}$$

where x_i is the calculated displacement i samples ago. This compensation method is verified by real-time experiments, and the hybrid testing results are similar to that of full physical shaking table experiments, which confirmed the effectiveness of the compensation method.

Horiuchi and Konno updated the compensation method in [7]. It is pointed out that for the compensation method proposed in [6], when the natural frequency of the structure inspected is high, or when the actuator lag is large, the testing system becomes unstable. For the system with a numerical mass of M, and a physical excitation mass of m, the stability condition is:

$$\frac{m}{M} < \frac{1}{|H|} \tag{2.3}$$

where $|H|$ is the sum of the absolute values of the coefficients a_i. To increase the stability margin, a new compensation method is introduced, based on linear prediction of the acceleration, and the displacement is calculated accordingly. With analysis, it is shown that the compensation algorithm in [7] has 40% larger critical frequency than that in [6]. The effectiveness and the criteria of stability of the algorithm is verified by experiments.

In summary, the group provided a good initial insight into the area, but restricted by the assumption that the actuator dynamic is pure time delay, the accuracy and application area is limited.

2.2 Research about Transfer Dynamics Cancellation

In [8], Chen and Ricles compared the compensation method by Horiuchi and Konno [7], Jung and Shing [9], together with the method proposed by Chen and Ricles [8] in discrete form. The transfer functions of the three compensating methods are discretized, and the frequency responses are compared. The method proposed in [8] is based on the assumption that the characteristics of the actuator in the hybrid testing system is simplified to a first order transfer function, thus the inverse of the transfer function is used for actuator lag compensation. The three compensation methods have different amplitude and phase characteristics in the frequency response. Sine sweep tests are also applied to the discretized compensation algorithms, with same value of actuator delay. All the methods are proved to be effective in real testing. However, according to the graphs by the author, the inverse compensation method by Chen and Ricles [8] seems to be slightly better in terms of accuracy.

However, the effectiveness of the inverse compensation method depends on a known accurate value for the actuator delay. Chen and Ricles [10] proposed a dual compensation scheme based on inverse compensation method to solve the problem. The block diagram of dual compensation scheme is illustrated in Figure 2.1:

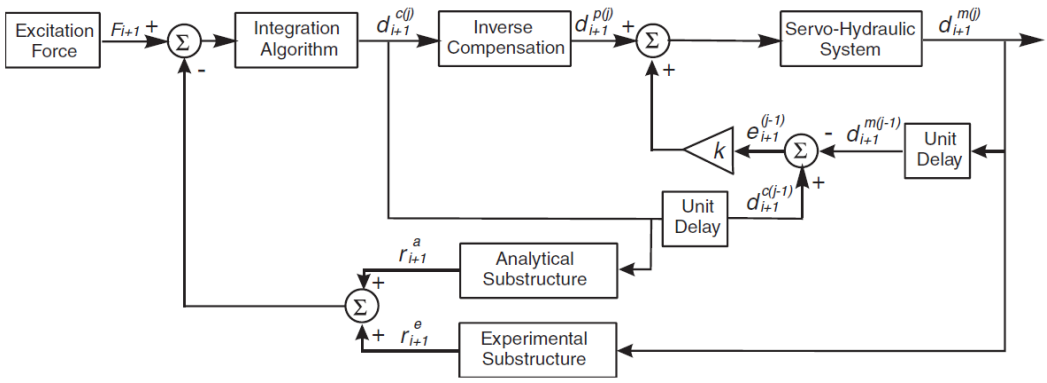

Figure 2.1 Block diagram of dual compensation scheme [10]

As shown in Figure 2.1, inverse compensation method is the main compensation method. In addition, the difference between the command displacement of the previous loop $d_{i+1}^{c(j-1)}$ and the actuator measured displacement of the previous loop $d_{i+1}^{m(j-1)}$ (that is, the actuator control error $e_{i+1}^{(j-1)}$ multiplied by a proportional gain *k*), is the secondary compensation.

The experiment results show that, when the time delay of the testing system is estimated inaccurately (in the experiment the error of the estimated time delay is ±50%), the actuator control error is reduced significantly in the dual compensation scheme.

Chen and Ricles then modified the inverse compensation method to an adaptive scheme in [11]. The original discrete transfer function of the inverse compensation is written in equation (2.6), where α is a value greater than 1 to indicate the time delay in the actuator response.

$$G_c(z) = \frac{X^p(z)}{X^c(z)} = \frac{\alpha \cdot z - (\alpha - 1)}{z} \tag{2.6}$$

In [11], the transfer function is modified to:

$$G_c(z) = \frac{X^p(z)}{X^c(z)} = \frac{(\alpha_{es} + \Delta\alpha) \cdot z - (\alpha_{es} + \Delta\alpha - 1)}{z} \tag{2.7}$$

where α_{es} is the estimated actuator delay, and $\Delta\alpha$ is an evolutionary variable. The details about the equations for updating the value of $\Delta\alpha$ can be found in [11].

The experimental results prove that the accuracy is greatly improved with adaptive inverse compensation method.

In [12], du Bois et al. focused on the modelling of the transfer dynamics of hydraulic actuators and controllers, and discussed the cancellation of the dynamics of the transfer systems based on the transfer function. Using a hybrid test based on a two mass system with a damper in the physical subsystem, the authors give examples of 1st and 2nd order

transfer systems, and investigated inverse model compensation. The authors suggest to implement the time delay compensation methods together with the inverse model compensation, because pure time delay could not be inverted.

2.3 Research about Computational Methods

Many authors published their research about the influence of the computational methods to the MiL test results. However, it is necessary to point out that the research is often not only about numerical implementation methods, but also involves some contents of transfer dynamics cancellation as mentioned in the previous section.

Darby et al. studied the behaviour and accuracy of the numerical substructure, in particular the discretization methods [13]. The analysis and the experimental results show that, although the central difference method is easily applied in time stepping routines, when it is used in real-time substructuring test, the results are very poor, especially when used in the test of multi-degree-of-freedom systems. A first-order-hold method is described in [13], which, compared to central difference method, is much more accurate without compromising stability in this particular case.

Darby et al. also suggests in [13] that, firstly, the input can be modified to the integral form of the original signal, which will reduce the high frequency noise and the truncation errors, secondly, the output can be interpolated to get a smoother output.

In [14], Darby et al. found that the stability margin of the testing systems can be really small, even in very simple systems. In addition, the testing system may have nonlinear characteristics, which means the delay of the system will change with the varying stiffness. To solve the problem, a method of predicting the delay is proposed.

The estimation of the delay for the *n*th time step δ_n is estimated with the delay of the previous step:

$$\delta_n = \delta_{n-1} + \Delta\delta = \delta_{n-1} + C_p \tanh\left(C_v \frac{\left(x_{c_n} - x_{c_{n-1}}\right)}{T} \right)\left(x_{c_{n-1}} - x_{m_{n-1}}\right) \tag{2.9}$$

In equation (2.9), T is the time step, C_v is the velocity gain, and C_p is the proportional gain, $x_{c_{n-1}}$ is the calculated desired displacement for time step n-1, $x_{m_{n-1}}$ is the measured displacement for time step n-1, and x_{c_n} is the calculated desired displacement for time step n. It is tested that, when C_v is about ten times the value of C_p, the algorithm gives good prediction.

The experiments show that the prediction converges gradually to the accurate time delay, but the speed of convergence is slow. This method cannot be applied to rapidly changing nonlinear systems.

Ahmadizadeh et al. developed another method of online measurement of the time delay [15], by simply comparing the desired displacement and the measured displacement histories, as shown in Figure 2.2.

The distance is measured by using linear fits to the last three data of each signal. The delay at step n can be calculated by equation (2.10).

$$\tau_n = \tau_{n-1} + 2G\Delta t \frac{u_n^{ad} - u_n^{am}}{u_n^m - u_{n-2}^m} \tag{2.10}$$

where $u_n^{ad} = \frac{u_n^d + u_{n-1}^d + u_{n-2}^d}{3}$, and $u_n^{am} = \frac{u_n^m + u_{n-1}^m + u_{n-2}^m}{3}$

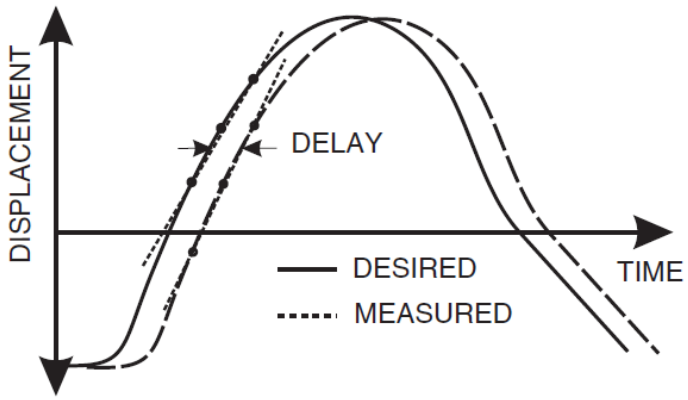

Figure 2.2 Direct estimation of delay using desired and measured displacement histories [15]

In equation (2.10), u_{n-2}^{d}, u_{n-1}^{d} and u_{n}^{d} are the desired displacements for time step *n*-2, *n*-1 and *n* respectively, while u_{n-2}^{m}, u_{n-1}^{m} and u_{n}^{m} are the measured displacements for time step *n*-2, *n*-1 and *n* respectively. *G* is the learning gain, which should be set properly. The optimal value of *G* should be the largest value which do not make the estimation highly oscillatory, and have to be calibrated for each particular case.

However, in the example given by the authors, the rise time of the delay prediction is nearly 1 second, which is unlikely to be suitable for the measurement of a rapidly changing nonlinear system.

Ahmadizadeh et al. also compared different delay compensation methods [15]. The methods are classified into 2 groups: 1. Modification of the command displacement, and 2. Correction of the force measurements.

For modification of the command displacement type, various methods are analyzed and compared including the methods by Horiuchi et al. [6] [7] and a method proposed by the authors using kinematic expressions, with the assumption of constant acceleration. The proposed method was successfully implemented, which shows advantage over polynomial extrapolation methods in force measurements during earthquake tests, because it is less sensitive to high frequency noise.

The other approach of compensation is to correct the measured force by seeking the corresponding force when the desired displacement is achieved, that is, correction of the force measurements. Because this method does not need an accurate estimation of the delay, it can be used in combination with displacement extrapolation procedures to obtain a satisfactory compensation before the estimated delay converges.

The authors also introduced variable gain and a moving window averaging procedure to solve the problems of undershooting in displacement reversals and large variation of the calculated gain.

Zhu et al. presented a comparison of different explicit integration algorithms for real-time hybrid simulation in [16]. The authors compared seven explicit integration algorithms, the methods are analysed with discrete-time root locus, and the theoretical findings are verified by real-time hybrid test based on a multiple story shear frame. It is found by the authors that the stability of the system is mostly determined by the time delay of the system itself, while the accuracy of the real-time hybrid testing is mainly influenced by the inherent characteristics of the integration algorithms. As a conclusion, the authors suggest to apply the integration methods with better accuracy in the real-time hybrid simulation, because the algorithms with unconditionally stability may not guarantee the stability of the system anyway.

In real-time hybrid simulation (RTHS), the numerical subsystem needs very fast calculation to maintain the hard real-time constraints, and it is especially computational costly for higher order finite element models. To be able to use more complex numerical models in RTHS, Maghareh et al. introduced a scheme in [17] called adaptive multi-rate interface (AMRI), which enables the numerical subsystem to be run at a lower sampling rate, while coupling with the physical substructure run at a higher sampling rate. The effectiveness of AMRI is verified with experiment. The authors found that the proposed multi-rate method has a smaller global error compared with the result of the test with simplified numerical model, and that the modelling error in the numerical substructure considerably affect the accuracy of the global response.

2.4 Novel Compensation Methods

In [18], Nikzad et al. proposed a method for compensating the actuator dynamics and computational delay, based on a 23 layer feedforward neurocontroller. The effectiveness of the trained feedforward neurocontroller is examined with a two-degree-of-freedom electrohydraulic system, compared with the conventional feedforward controller (the structure of the conventional feedforward controller can be found in [18]). The simulation results show that the neurocontroller has advantages over the conventional feedforward controller in high frequency noise reduction from the measured signal and better computational time delay compensation. However, the presented results of the proposed neurocontroller are only based on simulation, and not checked by experiment. Because the presented controller is based on a linearized and simplified model, due to the inevitable modelling error, there may be some difficulties in experimental implementation.

Wagg and Stoten [19] proposed an adaptive control method to be applied in real-time substructuring testing, the adaptive minimal control synthesis (MCS) algorithm. The MCS algorithm is already developed [20] and transformed to be used in substructure testing.

The basic control signal of MCS algorithm is:

$$u(t) = K(t)x(t) + K_r(t)r(t) \tag{2.11}$$

where $r(t)$ is the reference signal, $K(t)$ is the feedback adaptive gain and $K_r(t)$ is the feedforward adaptive gain.

Neild et al. tested the MCS method introduced by Wagg and Stoten [19] in [21] with a single-degree-of-freedom substructuring experiment. It is shown that for the first 13 seconds of the experiment, the MCS algorithm worked well, however, after 13 seconds, noticeable error occurs for a period of about 4 seconds, during which time the adaptive gains are observed to be highly oscillatory. With a series of tests, it is concluded that

the problem is caused by the increase of phase lag between the ground excitation r and the numerical model output x_m. The conclusion is verified by mathematical analysis.

To overcome the problem of rapid adaptive gain variation, Neild et al. suggested a modification of the MCS algorithm, where the numerical substructure output is written in terms of force feedback. The experimental results show that the modified MCS algorithm is accurate and stable, and the previous problem is not observed.

P.A. Bonnet et al. [22] investigated further into the modified MCS scheme. In this paper, a real-time hybrid testing system is constructed with nonlinear characteristics in both numerical and physical subsystems. Newmark explicit scheme is introduced in modeling and solving the nonlinear behaviour in the numerical subsystem, while the MCS with modified demand is used to compensate for the actuator delay. Because of the very different nature and calculation requirements of the two substructures, a multi-tasking strategy has been employed.

The experiment results, with a 5 degree-of-freedom system, show great agreement with the desired output and simulation results. However, if the coupling stiffness between the substructures is high (about 425 N/mm in the example given by the authors), the testing system will become very oscillatory. A stability analysis of the testing system is given in the paper.

Li et al. developed a procedure to apply model predictive control (MPC) to solve the saturation problem in dynamically substructured systems in [23]. A quasi-motorcycle suspension system is made into a real time hybrid test, and implemented as a case study. To deal with the measurement noise, a reduced order Kalman-Bucy observer is applied. The authors also proposed a cost function considering the actuator slew rate limit. The effectiveness of the proposed method is verified by experiments. However, the authors find that the application of the cost function mitigating the slew rate and the observer with a higher order will increase the computation time, and therefore affect the maximum sampling rate of the test.

In a more recent research by Li et al. [24], the authors applied a novel robust disturbance rejection antiwindup technique based on linear H_∞ controller to deal with the actuator saturation problem in dynamically substructured systems. In the proposed control scheme, H_∞ controller works as a basis to maintain the robustness, and antiwindup is used as the main compensation method. The techniques are again implemented in the hydraulically actuated quasi-motorcycle testing rig. Several antiwindup procedures are compared in [24], and the Disturbance Rejection antiwindup (DRAW) approach shows its advantage in the reduction of substructuring errors.

Ou et al. proposed an innovative actuator control algorithm called the robust integrated actuator control (RIAC) strategy in [25]. The control system consists of feedback control based on H_∞ optimization, a linear-quadratic-estimation block for minimizing noise, and a feedforward component to attenuate residual lag. The proposed control scheme is implemented using a 3 DOF building frame as the real-time hybrid simulation example. For both the full-scaled high capacity actuator and the down-scaled high speed actuator, the proposed control algorithm is effective in accuracy and measurement noise reduction. The research looks promising, however, the potential of H_∞ optimization is not fully explored. The authors combine several methods in the solution, but minimizing noise and compensating lag to improve accuracy could actually be realized by a single unified H_∞ optimisation approach.

2.5 Concluding Remarks

Judging by the contents of the existing literatures (as presented in Chapter 1 and Chapter 2), there are still some important topics which haven’t been investigated or not been researched thoroughly enough in the area of MiL testing, which are listed as follows:

1. A lot of the literatures are written in an application focused presentation. There's still a lack of analysis of the MiL test system in general, for example the method of constructing a MiL test system from the mathematical model of the whole system, and stability analysis of the constructed MiL system.
2. Plenty of literatures have pointed out that the lag introduced by the actuators will affect the accuracy of the test results. However, in most of the presented research, the modelling of the actuator lag is not accurate enough. In most of the literatures, the actuator lag is either treated as a pure time delay or a 1^{st} order transfer function, which may be incompetent to accurately represent the behaviour of the actuators in real life.
3. Because in a lot of the literatures, the research is based on the assumption of much simplified actuator dynamics, one main challenge when designing a compensator for a MiL system hasn't been addressed enough: the problem of signal saturation caused by the interaction of high frequency measurement noise and the high order compensator.
4. To achieve accurate testing results, a lot of compensation methods have been proposed to compensate for the actuator dynamics. However, most of the methods are not accurate enough because of the much simplified actuator dynamics. Some recent research has shown some novel compensation methods that look promising, but the methods are usually complicated. The compensation method for the actuator lag generally needs further investigation.
5. There isn't any research to date concerning the methods of choosing suitable actuators for some specific MiL test. It will be helpful to give some insight in how to choose the appropriate hardware before a MiL test system is built.

The research presented in this thesis is focused on providing a thorough investigation into the listed topics.

Chapter 3

3 Analysis of MiL Systems

In MiL testing, the “interface” between the physical part and the virtual part becomes the biggest source of disturbance and error. Generally, the “interface” includes actuators, sensors, and filters. It is challenging to adjust the “interface” reasonably to minimize the disturbance and get a satisfactory testing result.

In this chapter, a general procedure of analysing the characteristics of the MiL testing systems is presented, using two simplified mass-spring-damper examples. This chapter is divided into 6 sections:

3.1 Methodology

3.2 Example MiL Systems

3.3 Stability Analysis

3.4 Sensor Noise and Disturbances

3.5 MiL System with Inverse Model Compensator

3.6 Concluding Remarks

3.1 Methodology

In this section, a general guideline for a general analysis of a MiL test system is presented. Throughout Chapter 3, the proposed general method is presented using two typical examples: single mass-spring-damper system, and two DOF mass-spring-damper system. The reason of choosing the two example systems is that, firstly, the examples are very typical and have a wide application; and secondly, the method can be generalised, and so systems with more degrees of freedom can be analysed with the same approach.

The procedures for a general analysis of a MiL test system are listed as follows:

1. Based on the mathematical model of the whole test system, determine the location of splitting the whole system in half, and find the signals which connect the simulated subsystem and the physical subsystem.
2. Derive the transfer function for the simulated subsystem and the physical subsystem respectively.
3. Obtain the transfer function for the actuator model, and add the model between the output of the simulated subsystem and the input of the physical subsystem.
4. Obtain the open loop transfer function of the MiL test system, and bode plot the open loop transfer function to observe the stability margins, and determine if the system is stable.
5. Design a compensator for the MiL system based on the transfer function of the actuator model, and add the compensator model between the output of the simulated subsystem and the actuator model. (The procedure will be discussed in-depth in Chapter 4.)
6. Consider the measurement noise in the signal measured in the physical subsystem, which is fed back to the simulated subsystem, check the signal from the output of the compensator model, and determine, with the measurement noise added, if the compensated signal will saturate.

3.2 Example MiL Systems

3.2.1 Single Mass-spring-damper MiL System

An example of a simple one-degree-of-freedom mass-spring-damper is used to study the characteristics and limits of MiL testing, as illustrated in Figure 3.1.

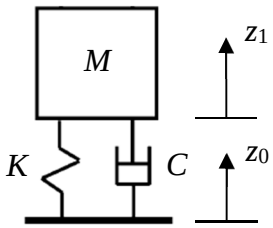

Figure 3.1 Mass on spring and damper model

The mathematical model of the system shown in Figure 3.1 is:

$$-K(z_1 - z_0) - C(\dot{z}_1 - \dot{z}_0) = M\ddot{z}_1 \tag{3.1}$$

Assume that a MiL test is designed, with the spring and damper model in the virtual part, and the mass in the physical part. The simulated displacement calculated from the spring and damper model becomes the input signal for an actuator, and the actuator is attached to the physical mass, while the force between the actuator and the physical mass is measured by a sensor, and is fedback to the virtual part.

Let:

$$-K(z_1 - z_0) - C(\dot{z}_1 - \dot{z}_0) = M\ddot{z}_1 = f \tag{3.2}$$

where *f* is the force between the actuator and the physical mass, measured by the sensor.

Using '*s*' as the differential operator, equation (3.2) can be written as equation (3.3).

$$-K(z_1 - z_0) - Cs(z_1 - z_0) = Ms^2 z_1 = f \tag{3.3}$$

$$Ms^2 z_1 = f \tag{3.4}$$

It can be shown that:

$$-(Cs + K)(z_1 - z_0) = f \tag{3.5}$$

$$z_1 = z_0 - \frac{1}{Cs + K} f \tag{3.6}$$

Equation (3.4) is the mathematical model of the physical subsystem, and equation (3.6) is the model of the numerical subsystem.

3.2.2 Two DOF Mass-spring-damper MiL System

An example of a two degree-of-freedom mass-spring-damper system is also given to have a more challenging study of the Model-in-the-Loop system. The system is shown in Figure 3.2.

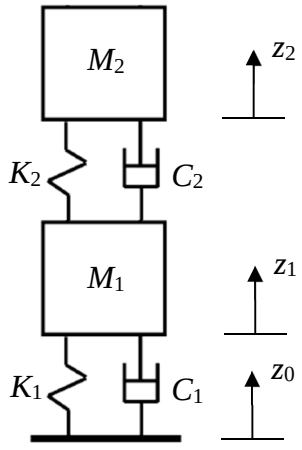

Figure 3.2 Two DOF mass-spring-damper model

An example of the application of the two DOF model is to test the interaction between the running vehicle engine (M_2) supported on different engine mounts (C_2, K_2) and the vehicle suspension and chassis (M_1, K_1, and C_1). It is important to notice that only the vertical direction is considered in this example.

The application is illustrated in Figure 3.3 and Figure 3.4, where Figure 3.3 shows the all physical testing example, such as commonly used in engine mount testing [26], and Figure 3.4 shows the testing example using MiL method, where the vibration of the suspension and chassis is simulated and the actuators follows the simulated motion. The interaction between the engine and the chassis is observed whilst the engine is running, and also with simulated vertical road displacement inputs representative of road roughness.

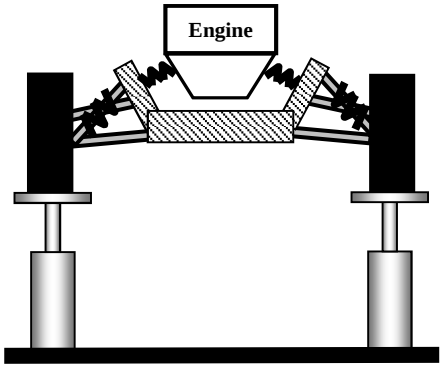

Figure 3.3 Vehicle engine-chassis vibration testing

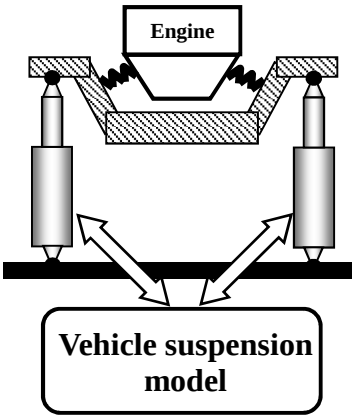

Figure 3.4 Vehicle engine-chassis vibration testing using MiL method

The mathematical model of the system shown in Figure 3.2 can be expressed as:

$$-K_2(z_2 - z_1) - C_2(\dot{z}_2 - \dot{z}_1) = M_2\ddot{z}_2 \tag{3.7}$$

$$K_2(z_2 - z_1) + C_2(\dot{z}_2 - \dot{z}_1) - K_1(z_1 - z_0) - C_1(\dot{z}_1 - \dot{z}_0) = M_1\ddot{z}_1 \tag{3.8}$$

Assume a MiL test is designed similar to that described in Section 3.2.1, with M_1, C_1, and K_1 in the numerical subsystem, and M_2, C_2, and K_2 in the physical subsystem. The simulated displacement calculated from M_1, C_1, and K_1 becomes the input signal for an actuator, and the actuator is attached to the physical part, where M_2, C_2, and K_2 are included, while the force between the actuator and the physical part is measured by a sensor, and is feedback to the virtual part.

Let:

$$-K_2(z_2 - z_1) - C_2(\dot{z}_2 - \dot{z}_1) = M_2\ddot{z}_2 = f \tag{3.9}$$

It can be shown that:

$$f = -(C_2 s + K_2)(z_2 - z_1) \tag{3.10}$$

And:

$$-f - (C_1 s + K_1)(z_1 - z_0) = M_1 s^2 z_1 \tag{3.11}$$

Equation (3.10) is the mathematical model of the physical subsystem, and equation (3.11) is the model of the numerical subsystem.

3.2.3 Actuator and Sensor in the MiL System

For the MiL test system described in Section 3.2.1 and Section 3.2.2, the actuator and the sensor are the "interface" between the physical part and the virtual part. Because the actuator and the sensor are not ideal, they will reduce the test accuracy. The most common problems introduced by the actuator and the sensor are that, the actuator will have a limited dynamic response (often described as a time delay in the literature), and the sensor will introduce some high frequency noise to the system.

The model described above can be illustrated by Figure 3.5.

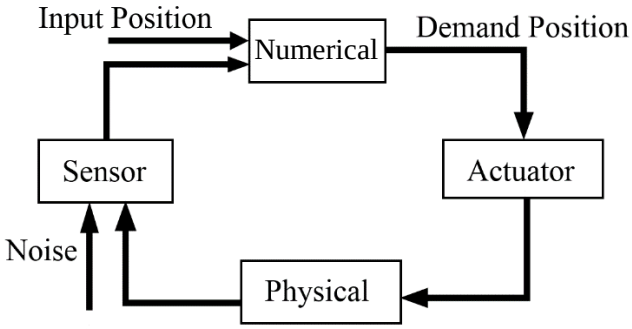

Figure 3.5 Model-in-the-Loop system

To compensate for the characteristics of the actuator, a compensator can be added between the virtual model and the actuator. Denoting the transfer function of the actuator as $A(s)$, if the compensator is set to be the inverse of the actuator model, $1/A(s)$, theoretically the compensator can totally cancel out the lag of the actuator. However this will not work in reality because:

1. This compensator design method requires an accurate actuator model $A(s)$, which may not be available.
2. high frequency measurement noise linked to the implicit differentiation in the compensator means the system will become very noisy, and the actuator drive signal will saturate;

3. Some characteristics of the actuator may be very difficult or even impossible to compensate, for example, some non-linear behaviours, pure time delay, and non-minimum phase behaviour giving an unstable inverse.

In conclusion, it is often very challenging to design a compensator which can attenuate the lag caused by the actuator well enough, without making the system overly noisy or unstable.

3.3 Stability Analysis

The block diagram of a typical uncompensated MiL system is shown in Figure 3.6. In this block diagram, the noise and other non-ideal characteristics introduced by the sensor are ignored, for the convenience of analysis.

In Figure 3.6, S stands for the numerical subsystem, A stands for the actuator model, and P represents the physical subsystem.

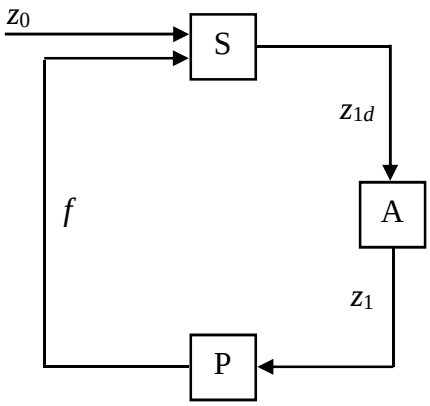

Figure 3.6 The block diagram of a typical uncompensated MiL system

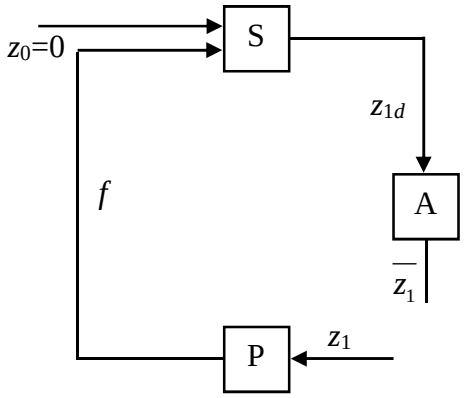

Figure 3.7 The block diagram for stability analysis

Breaking the closed loop of the MiL model in the point between the actuator model and the physical model, and setting the input signal z_0 to zero, the system becomes as shown in Figure 3.7.

To analyse the stability of the MiL system, the transfer function from z_1 to $\overline{z_1}$ needs to be found.

3.3.1 Stability Analysis for the Single Mass-spring-damper System

The equation for the numerical subsystem is:

$$z_{1d} = z_0 - \frac{1}{Cs + K} f \tag{3.12}$$

Let z_0=0, it can be shown that:

$$\frac{z_{1d}}{f} = -\frac{1}{Cs + K} \tag{3.13}$$

From equation (3.4), the equation for the physical subsystem is:

$$\frac{f}{z_1} = Ms^2 \tag{3.14}$$

If the mathematical model of the actuator can be represented by transfer function $A(s)$:

$$\frac{\overline{z_1}}{z_{1d}} = A(s) \tag{3.15}$$

The transfer function from z_1 to $\overline{z_1}$ can be calculated as shown in equation (3.16).

$$\frac{\overline{z_1}}{z_1} = \frac{f}{z_1}\frac{z_{1d}}{f}\frac{\overline{z_1}}{z_{1d}} = -\frac{Ms^2}{Cs+K}A(s) \tag{3.16}$$

It is important to notice from Figure 3.6 and Figure 3.7 that, the MiL system is a system with positive feedback. For the convenience of stability analysis, a negative sign is multiplied to the open loop transfer function to change it to a negative feedback system.

So the open loop transfer function used for stability analysis is:

$$-\frac{\overline{z_1}}{z_1} = \frac{Ms^2}{Cs+K}A(s) \tag{3.17}$$

An example of the stability analysis of the single mass-spring-damper system is given as follows:

In this example, the transfer function of the actuator $A(s)$ is third order, which is obtained by a linearized estimation of the frequency response measurement of a hydraulic robot arm. Details about the structure, the frequency response measurement, and the transfer function estimation of the robot arm will be discussed in Chapter 5.

The estimated transfer function of the actuator is:

$$A(s) = \frac{1}{0.00006079s^3 + 0.005046s^2 + 0.0812s + 1} \tag{3.18}$$

The parameters are set to: M = 400 kg, C = 1000 Ns/m, K = 16000 N/m.

The Bode plot of the open loop transfer function of the MiL system is illustrated in Figure 3.8. It is notable that although the stability of the system could also be judged by other means, for example by judging the poles of the closed loop transfer function, frequency analysis is used in this thesis because of the interest in the gain margins and phase margins.

It can be seen from the figure that, the phase is not crossing -180˚, which means the system is stable.

The simulation result of the unit step response of the MiL system generated with Simulink is shown in Figure 3.9. The diagram of the Simulink model can be found in Appendix 3.1.1. The simulation result verified the conclusion that this specific system in this example is stable.

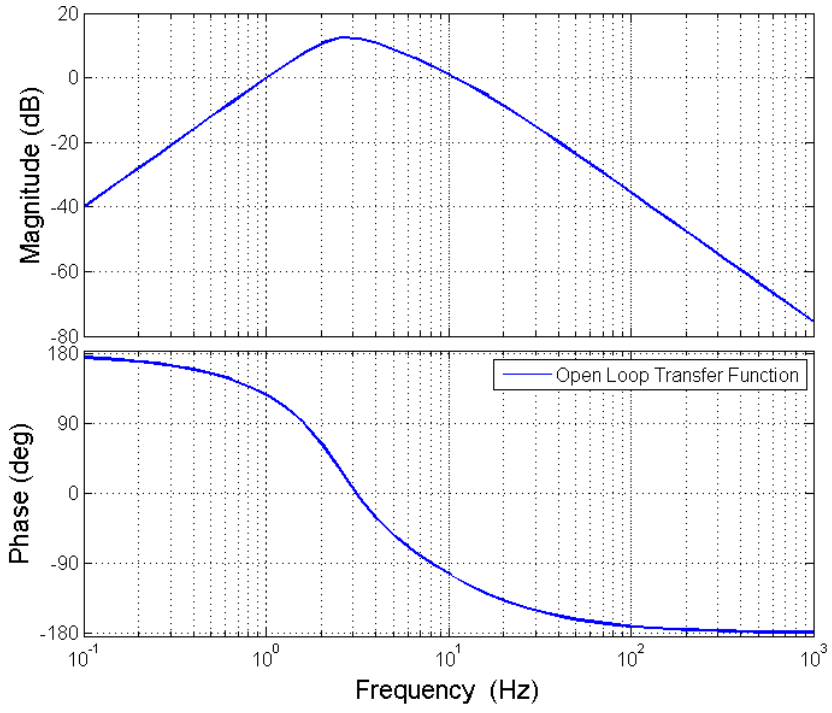

Figure 3.8 Bode diagram of the open loop transfer function of the single mass-spring-damper based MiL system

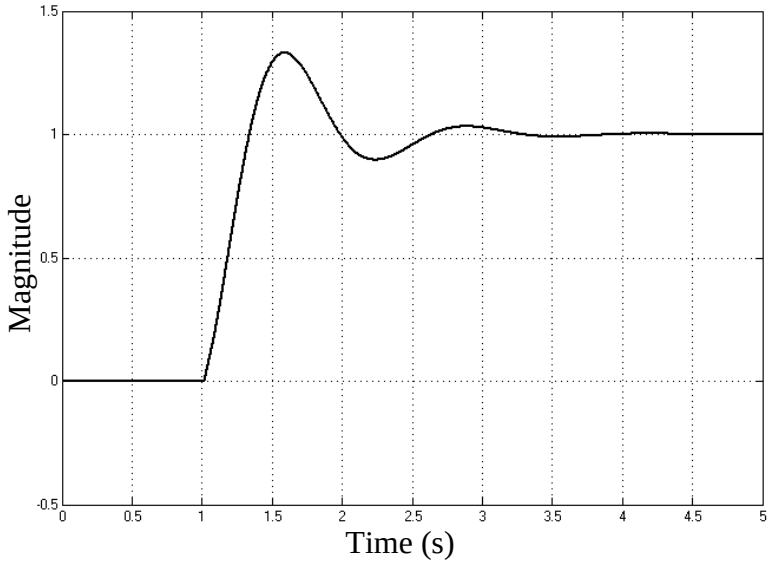

Figure 3.9 The simulation result of the unit step response of the first MiL system

3.3.2 Stability Analysis for the Two DOF Mass-spring-damper System

The equation for the numerical subsystem is:

$$-f-(C_1 s+K_1)(z_{1d}-z_0)=M_1 s^2 z_{1d} \tag{3.19}$$

Let z_0=0, the transfer function from f to z_{1d} can be derived:

$$\frac{z_{1d}}{f}=-\frac{1}{M_1 s^2+C_1 s+K_1} \tag{3.20}$$

From equation (3.9), it can be shown that the equation for the physical subsystem is:

$$-(C_2 s+K_2)(z_2-z_1)=M_2 s^2 z_2=f \tag{3.21}$$

$$z_2 = \frac{C_2 s + K_2}{M_2 s^2 + C_2 s + K_2} z_1 \tag{3.22}$$

Substitute equation (3.22) into equation (3.21):

$$\frac{M_2 s^2 (C_2 s + K_2)}{M_2 s^2 + C_2 s + K_2} z_1 = f \tag{3.23}$$

$$\frac{f}{z_1} = \frac{M_2 s^2 (C_2 s + K_2)}{M_2 s^2 + C_2 s + K_2} \tag{3.24}$$

The mathematical model of the actuator is represented by transfer function $A(s)$.

The transfer function from z_1 to $\overline{z_1}$ can be calculated as follows:

$$\frac{\overline{z_1}}{z_1} = \frac{f}{z_1} \frac{z_{1d}}{f} \frac{\overline{z_1}}{z_{1d}} = -\frac{M_2 s^2 (C_2 s + K_2)}{(M_1 s^2 + C_1 s + K_1)(M_2 s^2 + C_2 s + K_2)} A(s) \tag{3.25}$$

The same as described in Section 3.3.1, for the convenience of stability analysis, this transfer function is negated to change it to a negative feedback system.

So the open loop transfer function used for stability analysis is:

$$-\frac{\overline{z_1}}{z_1} = \frac{M_2 s^2 (C_2 s + K_2)}{(M_1 s^2 + C_1 s + K_1)(M_2 s^2 + C_2 s + K_2)} A(s) \tag{3.26}$$

An example of the stability analysis of the two DOF mass-spring-damper system with realistic parameters for the engine mount testing application is given as follows:

In this example, the transfer function of the actuator $A(s)$ is third order, which is obtained by a linearized estimation of the frequency response measurement of a Multi-Axis Simulation Table in the vertical direction [27].

The estimated transfer function of the Multi-Axis Simulation Table is:

$$A(s) = \frac{1}{(0.011s+1)(0.0053s+1)(0.0018s+1)} \tag{3.27}$$

The parameters are set to: M_1 = 415 kg, C_1 = 1000 Ns/m, K_1 = 20000 N/m, M_2 = 100 kg, C_2 = 150 Ns/m, and K_2 = 20000 N/m.

The Bode plot of the open loop transfer function of the MiL system is given in Figure 3.10.

It can be observed from Figure 3.10 that, at the frequency which the phase crosses -180˚, the magnitude is negative. This means the system is stable.

The Nyquist diagram of the open loop transfer function of the MiL system is plotted in Figure 3.11.

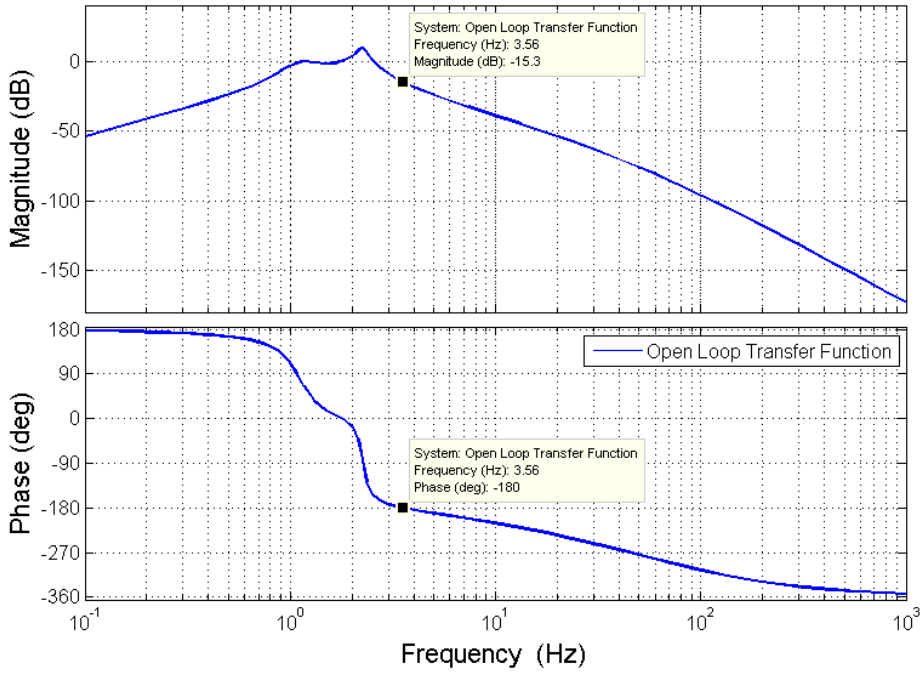

Figure 3.10 Bode diagram of the open loop transfer function of the two DOF mass-spring-damper based MiL system

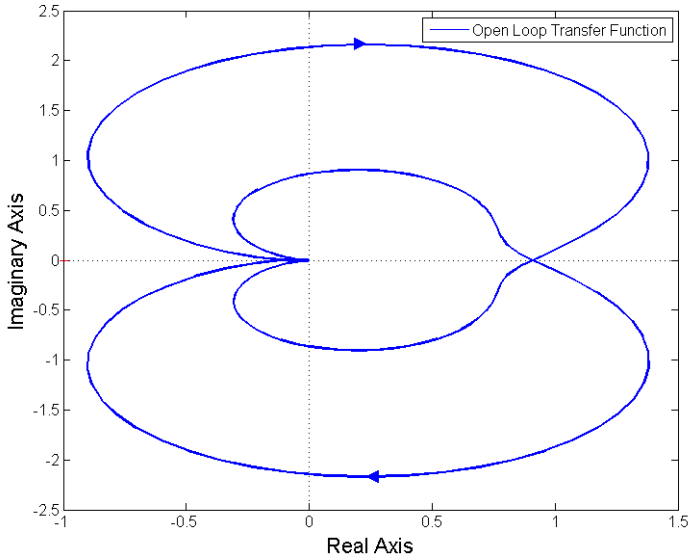

Figure 3.11 Nyquist diagram of the open loop transfer function of the second MiL system

According to the Nyquist stability criterion, this specific system is stable.

The simulation result of the unit step response of the specified MiL system generated with Simulink is shown in Figure 3.13. The diagram of the Simulink model can be found in Appendix 3.1.2. The simulation result verified the conclusion that this specific system in this example is stable.

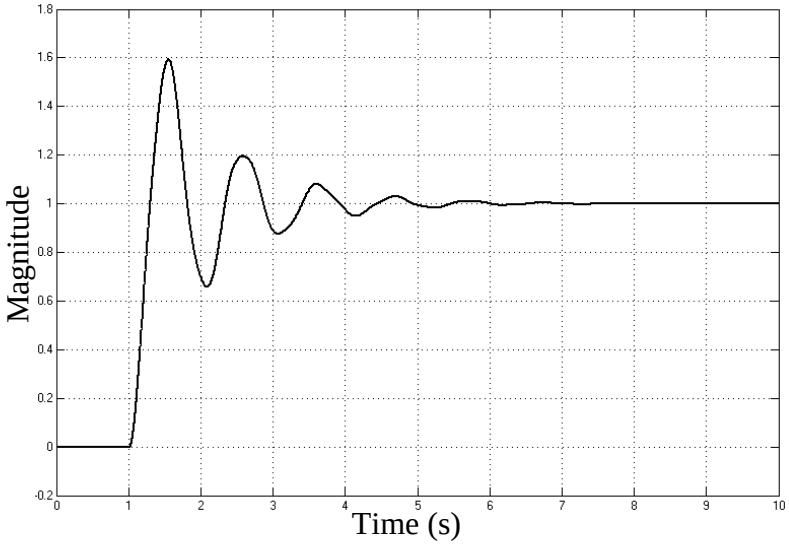

Figure 3.12 The simulation result of the unit step response of the two DOF mass-spring-damper based MiL system

Another example is given, showing that with some variation of the parameters, the MiL system can be unstable, where the parameter C_2 is modified to 20 Ns/m, and all other parameters remain the same. In summary, the parameters are set to: M_1 = 415 kg, C_1 = 1000 Ns/m, K_1 = 20000 N/m, M_2 = 100 kg, C_2 = 20 Ns/m, and K_2 = 20000 N/m.

The Bode plot of the open loop transfer function of the MiL system is shown in Figure 3.13.

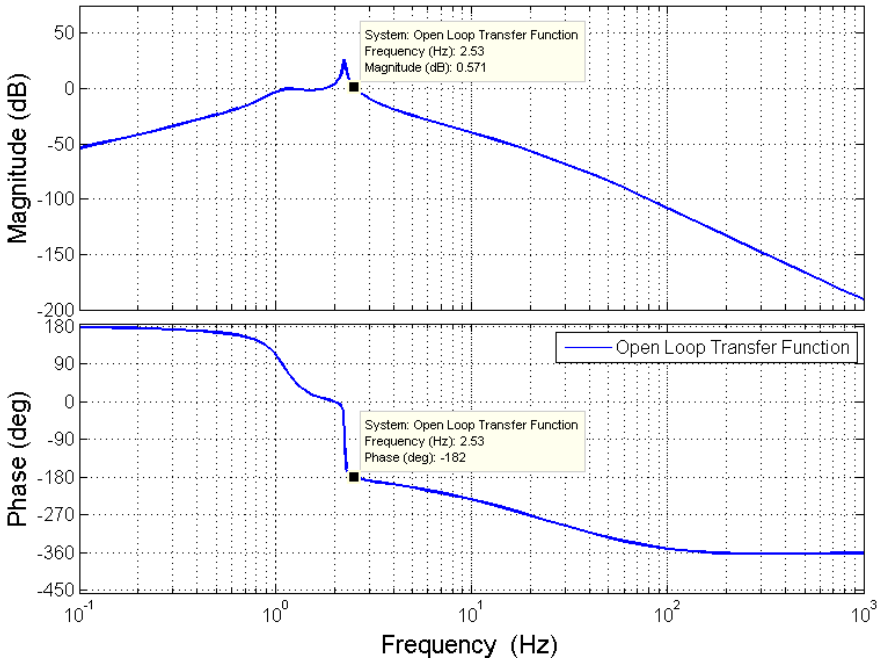

Figure 3.13 Bode diagram of the open loop transfer function of the two DOF mass-spring-damper based MiL system with reduced damping

It can be observed from Figure 3.13 that, at the frequency which the phase crosses -180˚, the magnitude is greater than one. This means the system is unstable.

The Nyquist diagram of the open loop transfer function of the MiL system is plotted in Figure 3.14.

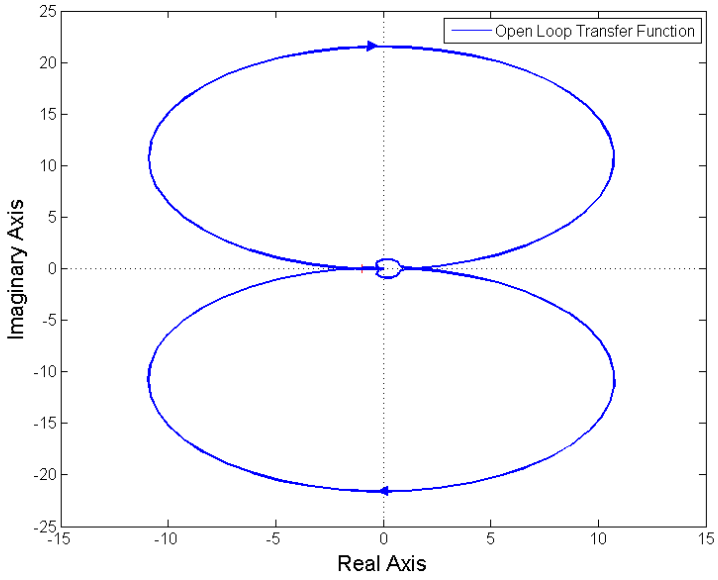

Figure 3.14 Nyquist diagram of the open loop transfer function of the two DOF mass-spring-damper based MiL system with reduced damping

To see the plot more clearly, the Nyquist diagram is zoomed in around the point (-1, *j*0), which is shown in Figure 3.15.According to the Nyquist stability criterion, this specific system is unstable. According to the Nyquist stability criterion, this specific system is unstable.

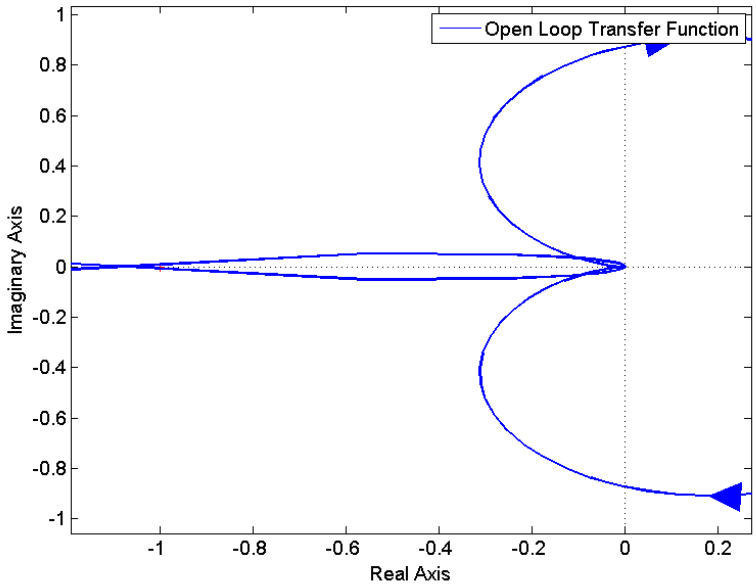

Figure 3.15 Nyquist diagram of the open loop transfer function of the two DOF mass-spring-damper based MiL system with reduced damping, zoomed in

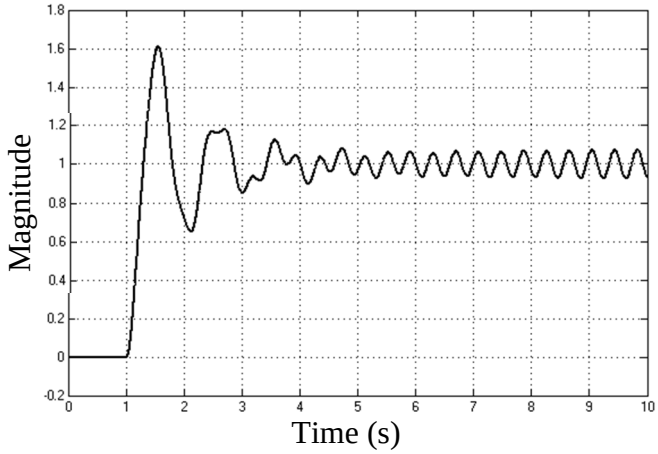

Figure 3.16 The simulation result of the unit step response of the two DOF mass-spring-damper based MiL system with reduced damping

The simulation result of the unit step response of the MiL system with low damping value in the physical part generated with Simulink is illustrated in Figure 3.16. The simulation result verified the conclusion that this specific system in this example is unstable.

3.4 Measurement Noise and Disturbances

In reality, there is measurement noise introduced to the testing loop during the test. In some applications, there is possibly high frequency disturbances other than the measurement noise, for example, the engine vibration in the example discussed in Section 3.2.2. The power of the noise and the disturbances may be amplified in the loop, thus the testing results are affected seriously. Consequently, it is important to study the sensitivity of the whole system to noise and disturbances.

For any MiL system with position control and force feedback structure similar to that described in Section 3.2, the noise is most likely generated in the force feedback path to the numerical model. An independent noise signal n is added into the system, as shown in Figure 3.17.

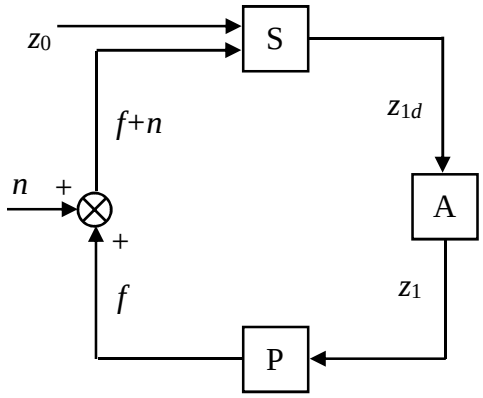

Figure 3.17 MiL system with noise added in the force feedback

3.4.1 Noise in the Single Mass-spring-damper MiL System

In this section, the influence of the electrical noise n to the displacement z_1 is analysed and compared to the influence from the input signal z_0. The equations for the MiL system built from a single mass-spring-damper system are shown as follows:

$$-(Cs+K)(z_{1d}-z_0)=f+n \tag{3.28}$$

$$f=Ms^2z_1 \tag{3.29}$$

$$\frac{z_1}{z_{1d}}=A(s) \tag{3.30}$$

To find the transfer function from the noise n to the displacement z_1, let $z_0 = 0$:

$$-(Cs+K)z_{1d}=f+n \tag{3.31}$$

Substitute equations (3.29) and (3.30) into equation (3.31):

$$-(Cs+K)\frac{z_1}{A(s)}=Ms^2z_1+n \tag{3.32}$$

$$\frac{z_1}{n} = -\frac{A(s)}{Ms^2A(s) + Cs + K} \tag{3.33}$$

To find the transfer function from the input displacement z_0 to the displacement z_1, let $n = 0$:

$$-(Cs + K)(z_{1d} - z_0) = f \tag{3.34}$$

Substitute equations (3.29) and (3.30) into equation (3.34):

$$-(Cs + K)\left(\frac{z_1}{A(s)} - z_0\right) = Ms^2 z_1 \tag{3.35}$$

$$\frac{z_1}{z_0} = \frac{(Cs + K)A(s)}{Ms^2A(s) + Cs + K} \tag{3.36}$$

An example is given to compare the transfer functions of $\frac{z_1}{n}$ and $\frac{z_1}{z_0}$ with the specified parameters.

The parameters' values and the actuator model are the same as that in Section 3.3.1.

The bode diagram of the transfer functions of $\frac{z_1}{n}$ and $\frac{z_1}{z_0}$ with the specified parameters are plotted in Figure 3.18.

It can be observed from Figure 3.18 that the magnitude of the transfer function from z_0 to z_1 is much larger than that of the transfer function from n to z_1. This is because the steady state gain of $\frac{z_1}{z_0}$ is K times larger than that of $\frac{z_1}{n}$. With a larger value of K, the noise transmitted to the displacement z_1 will be comparatively smaller.

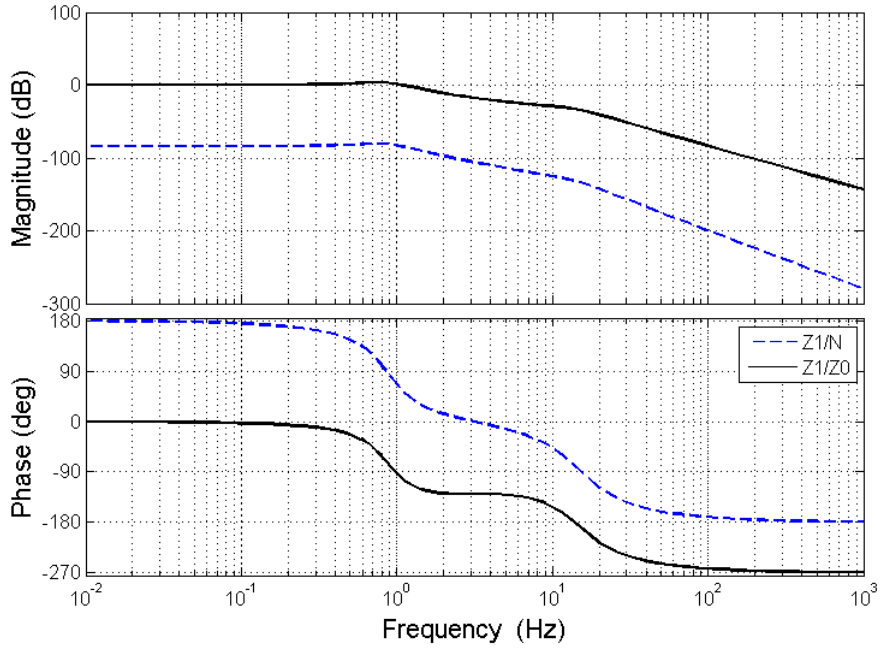

Figure 3.18 Comparing transfer functions $\frac{z_1}{n}$ and $\frac{z_1}{z_0}$

However, it is very important to point out, in reality the magnitude of the noise *n* might be very large, while the magnitude of the displacement input z_0 might be really small, so the real influence of the noise *n* to the testing target z_1 needs to be studied bearing this in mind.

Assume a filter *N*(*s*) is defined to describe the magnitude of the noise *n* at different frequencies, and another filter *Z*(*s*) is defined to describe the amplitude of the displacement input z_0 at different frequencies, then the transfer functions $N(s)\frac{z_1}{n}$ and $Z(s)\frac{z_1}{z_0}$ needs to be compared to determine the real influence of the noise *n* to the testing result.

3.4.2 Noise and Disturbance in the Two DOF Mass-spring-damper MiL System

The equations for the MiL system built from a two DOF mass-spring-damper system are shown as follows:

$$-\left(f+n\right)-\left(C_1 s+K_1\right)\left(z_{1d}-z_0\right)=M_1 s^2 z_{1d} \tag{3.37}$$

$$-\left(C_2 s+K_2\right)\left(z_2-z_1\right)=M_2 s^2 z_2=f \tag{3.38}$$

$$\frac{z_1}{z_{1d}}=A(s) \tag{3.39}$$

To find the transfer function from the noise n to the displacement z_1, let $z_0 = 0$:

$$-\left(f+n\right)-\left(C_1 s+K_1\right)z_{1d}=M_1 s^2 z_{1d} \tag{3.40}$$

It can be shown that:

$$-\left(C_2 s+K_2\right)\left(z_2-z_1\right)=M_2 s^2 z_2 \tag{3.41}$$

$$z_2=\frac{C_2 s+K_2}{M_2 s^2+C_2 s+K_2} z_1 \tag{3.42}$$

Substitute equations (3.38) and (3.39) into equation (3.40):

$$-\left(M_2 s^2 z_2+n\right)-\left(C_1 s+K_1\right)\frac{z_1}{A(s)}=M_1 s^2 \frac{z_1}{A(s)} \tag{3.43}$$

$$-A(s)\left(M_2 s^2 z_2+n\right)-\left(C_1 s+K_1\right)z_1=M_1 s^2 z_1 \tag{3.44}$$

Substitute equation (3.42) into equation (3.44):

$$-A(s)\left(\frac{M_2 s^2(C_2 s+K_2)}{M_2 s^2+C_2 s+K_2}z_1+n\right)-(C_1 s+K_1)z_1=M_1 s^2 z_1 \tag{3.45}$$

$$\frac{z_1}{n}=-\frac{A(s)(M_2 s^2+C_2 s+K_2)}{(M_1 s^2+C_1 s+K_1)(M_2 s^2+C_2 s+K_2)+A(s)M_2 s^2(C_2 s+K_2)} \tag{3.46}$$

To find the transfer function from the input displacement z_0 to the displacement z_1, let $n = 0$:

$$-f-(C_1 s+K_1)(z_{1d}-z_0)=M_1 s^2 z_{1d} \tag{3.47}$$

Substitute equations (3.38) and (3.39) into equation (3.47):

$$-M_2 s^2 z_2-(C_1 s+K_1)\left(\frac{z_1}{A(s)}-z_0\right)=M_1 s^2\frac{z_1}{A(s)} \tag{3.48}$$

Substitute equation (3.42) into equation (3.48):

$$-\frac{M_2 s^2(C_2 s+K_2)}{M_2 s^2+C_2 s+K_2}z_1-\frac{C_1 s+K_1}{A(s)}z_1+(C_1 s+K_1)z_0=\frac{M_1 s^2}{A(s)}z_1 \tag{3.49}$$

$$A(s)(C_1 s+K_1)z_0=(M_1 s^2+C_1 s+K_1)z_1+\frac{A(s)M_2 s^2(C_2 s+K_2)}{M_2 s^2+C_2 s+K_2}z_1 \tag{3.50}$$

$$\frac{z_1}{z_0}=\frac{A(s)(C_1 s+K_1)(M_2 s^2+C_2 s+K_2)}{(M_1 s^2+C_1 s+K_1)(M_2 s^2+C_2 s+K_2)+A(s)M_2 s^2(C_2 s+K_2)} \tag{3.51}$$

An example is shown below to compare the transfer functions of $\frac{z_1}{n}$ and $\frac{z_1}{z_0}$ with the specified parameters.

The parameters' values and the actuator model are the same as that in Section 3.3.2.

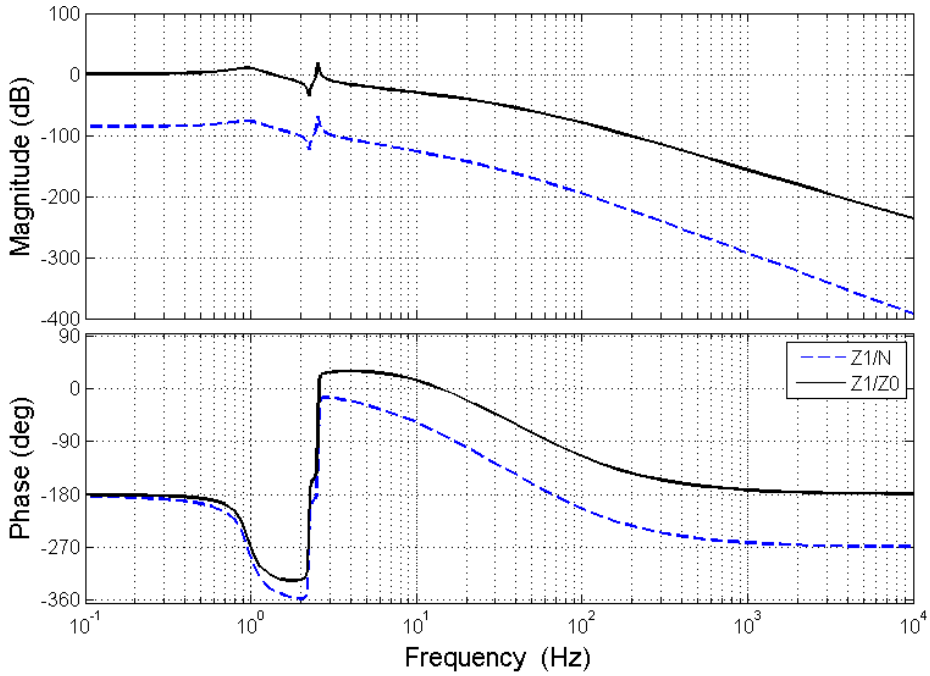

Figure 3.19 Comparing transfer functions $\frac{z_1}{n}$ and $\frac{z_1}{z_0}$ of the two DOF MiL system

The transfer functions of of $\frac{z_1}{n}$ and $\frac{z_1}{z_0}$ with the specified parameters are plotted in Figure 3.19.

Similar to Section 3.4.1, a conclusion can be drawn that the magnitude of the transfer function from z_0 to z_1 is much larger than that of the transfer function from n to z_1. This is because the steady state gain of $\frac{z_1}{z_0}$ is K_1 times larger than that of $\frac{z_1}{n}$. The larger the value of K_1 is, the less the noise will be transmitted to the displacement z_1, which is the testing target that needs to be accurately reproduced.

Similarly, assume a filter $N(s)$ is defined to describe the magnitude of the noise n at different frequencies, and another filter $Z(s)$ is defined to describe the amplitude of the displacement input z_0 at different frequencies, then the transfer functions $N(s)\frac{z_1}{n}$ and

$Z(s)\frac{z_1}{z_0}$ needs to be compared to determine the real influence of the noise *n* to the testing result.

As stated in the beginning of this chapter, there are possibly disturbances other than the measurement noise, for instance, in the engine-chassis vibration test example, the vibration of the vehicle engine.

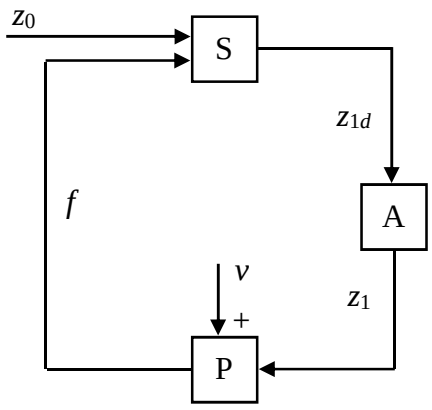

Figure 3.20 MiL system with disturbance force applied to the physical mass

The force generated by the engine vibration can be denoted by a disturbance force *v* directly applied to the physical mass M_2, as illustrated in Figure 3.20.

The equations for the described MiL system are listed as follows.

$$-f-(C_1 s+K_1)(z_{1d}-z_0)=M_1 s^2 z_{1d} \tag{3.52}$$

$$-(C_2 s+K_2)(z_2-z_1)-v=M_2 s^2 z_2=f \tag{3.53}$$

$$\frac{z_1}{z_{1d}}=A(s) \tag{3.54}$$

By solving the equations, the transfer function from the vibration force *v* to the displacement z_1 can be found in equation (3.55).

$$\frac{z_1}{v} = \frac{M_2 s^2 A(s)}{(M_1 s^2 + C_1 s + K_1)(M_2 s^2 + C_2 s + K_2) + A(s) M_2 s^2 (C_2 s + K_2)} \tag{3.55}$$

Compared with the transfer function from the measurement noise n to the displacement z_1:

$$\frac{z_1}{v} = -\frac{M_2 s^2}{M_2 s^2 + C_2 s + K_2} \frac{z_1}{n} \tag{3.56}$$

The details of the derivation of equations (3.55) and (3.56) are given in Appendix 3.2.1.

The influence of the measurement noise n and the disturbance v will be further analysed in the presence of an actuator dynamics compensator in Chapter 3.4.

3.5 Sensor Noise and Disturbances in the MiL System with Inverse Model Compensator

For the MiL system illustrated in Figure 3.6, the actuator will have a limited dynamic response, thus the accuracy of the testing results will be affected.

To compensate for the characteristics of the actuator, a compensator can be added between the virtual model and the actuator, as is shown in Figure 3.21.

Denoting the transfer function of the actuator as $A(s)$, if the compensator is set to be the inverse of the actuator model, $1/A(s)$, theoretically the compensator can totally cancel out the lag of the actuator. However, in reality this will not work, as described in Section 3.2.3.

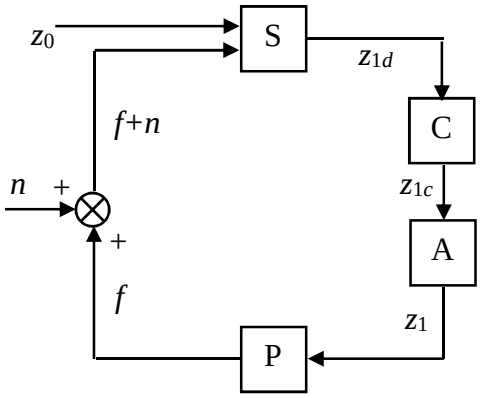

Figure 3.21 MiL system with compensator

3.5.1 Inverse Model Compensator in the Single Mass-spring-damper MiL System

The equations for the MiL system built from a single mass-spring-damper system are shown as follows:

$$-(Cs+K)(z_{1d}-z_0)=f+n \tag{3.57}$$

$$f=Ms^2z_1 \tag{3.58}$$

$$\frac{z_{1c}}{z_{1d}}=\frac{1}{A(s)} \tag{3.59}$$

$$\frac{z_1}{z_{1c}}=A(s) \tag{3.60}$$

To find the transfer functions from the noise n to the desired displacement z_{1d} and the compensated signal z_{1c}, let $z_0 = 0$:

$$-(Cs+K)z_{1d}=f+n \tag{3.61}$$

Substitute equations (3.58), (3.59) and (3.60) into equation (3.61):

$$-(Cs+K)z_{1d} = Ms^2 z_{1d} + n \tag{3.62}$$

$$\frac{z_{1d}}{n} = -\frac{1}{Ms^2 + Cs + K} \tag{3.63}$$

$$\frac{z_{1c}}{n} = -\frac{1}{(Ms^2 + Cs + K)A(s)} \tag{3.64}$$

It is noticeable that because theoretically the compensator can compensate for the dynamics of the actuator perfectly, so in this analysis, the desired displacement z_{1d} is equal to the actual displacement z_1.

An example is given to compare the transfer functions of $\frac{z_{1d}}{n}$ and $\frac{z_{1c}}{n}$ with the specified parameters.

The parameters' values and the actuator model are the same as that in Section 3.3.1.

The transfer functions of of $\frac{z_{1d}}{n}$ and $\frac{z_{1c}}{n}$ with the specified parameters are plotted in Figure 3.22.

It can be concluded from Figure 3.23 that, in the compensated signal z_{1c}, the noise signal n is amplified significantly, especially in the high frequency range. This is because, as stated before, the implicit differentiation in the inverse model compensator will emphasize the high frequency signal greatly.

The conclusion is checked with simulation results using Simulink. The diagram of the Simulink model can be found in Appendix 3.1.3.

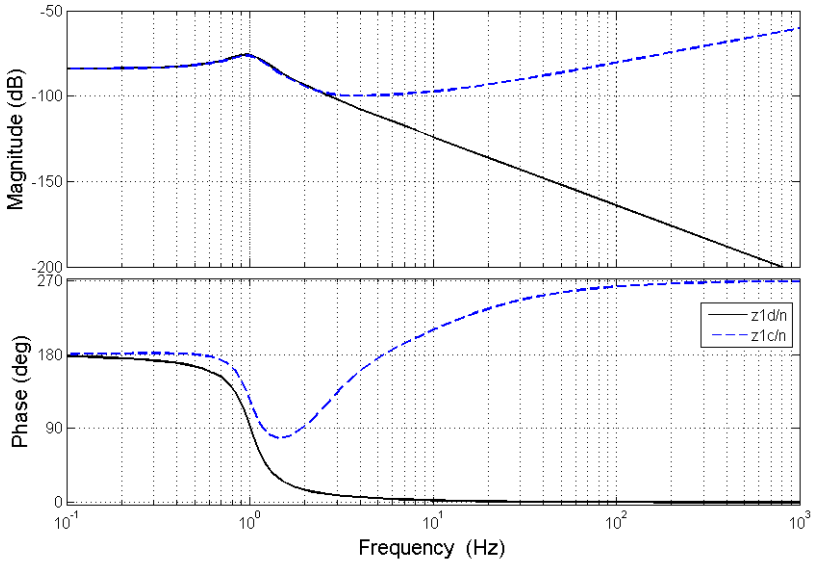

Figure 3.22 Comparing transfer functions $\frac{z_{1d}}{n}$ and $\frac{z_{1c}}{n}$

Figure 3.23 compares the feedback force with and without added sensor noise in Simulink. The black line shows the feedback force with no additional noise, while the blue line shows the feedback force with pink noise signal (which is a band-limited white noise filtered by a Butterworth high-pass filter) added to the force. The input displacement z_0 is a chirp signal.

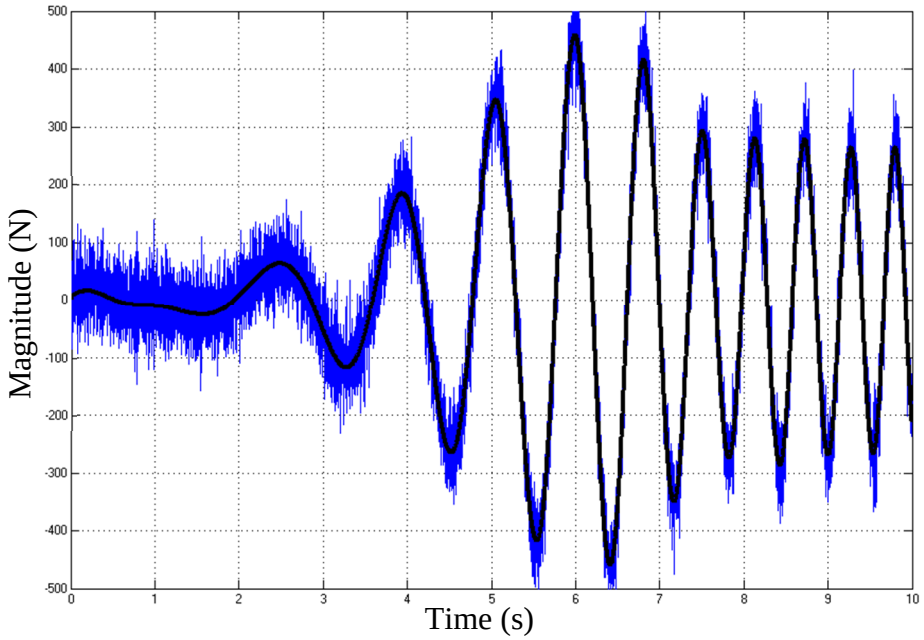

Figure 3.23 Feedback force with (blue) and without (black) the added noise

The simulation results comparing the compensated signal z_{1c} with and without the added noise is shown in Figure 3.24, where the black solid line represents the compensated signal z_{1c} with no noise added to the system, and the blue solid line shows the compensated signal z_{1c} with additional noise in the system. The root mean square value of the noise shown in Figure 3.24 is 0.0035.

From the simulation result, it can be concluded that the high frequency noise is amplified in the compensated signal. The large amplitude and rapid change of the signal may possibly lead to saturation in the compensated signal.

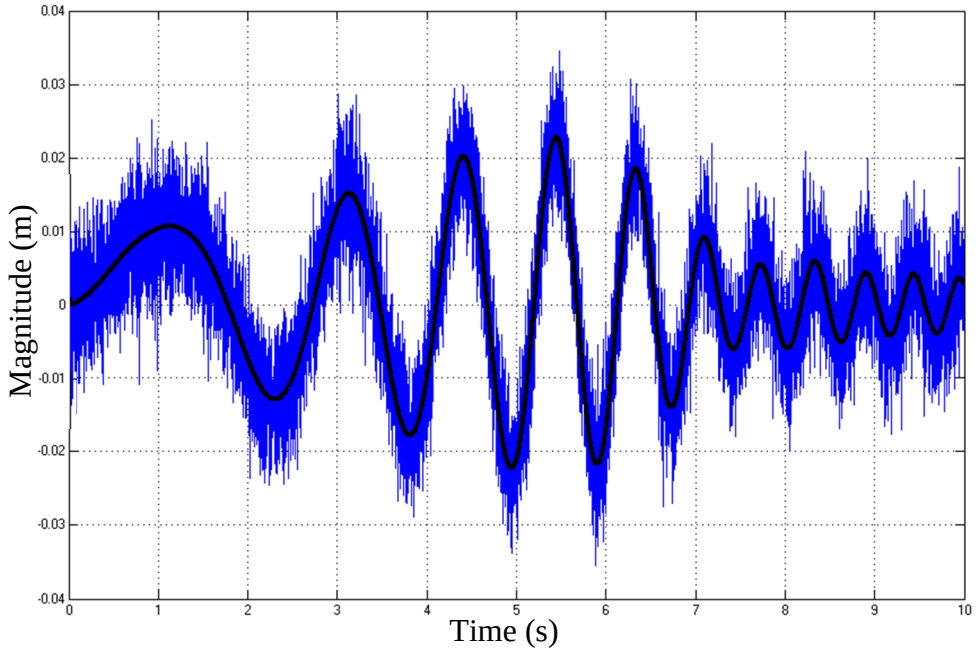

Figure 3.24 Compensated signal z_{1c} with (blue) and without (black) the added noise

3.5.2 Inverse Model Compensator in the Two DOF Mass-spring-damper MiL System

The equations for the MiL system built from a two DOF mass-spring-damper system are shown as follows:

$$-(f+n)-(C_1 s+K_1)(z_{1d}-z_0)=M_1 s^2 z_{1d} \tag{3.65}$$

$$-(C_2 s+K_2)(z_2-z_1)=M_2 s^2 z_2 = f \tag{3.66}$$

$$\frac{z_{1c}}{z_{1d}}=\frac{1}{A(s)} \tag{3.67}$$

$$\frac{z_1}{z_{1c}}=A(s) \tag{3.68}$$

The transfer function from the measurement noise n to the compensated signal can be found using the similar method as Section 3.4.2.

$$\frac{z_{1d}}{n}=-\frac{M_2 s^2+C_2 s+K_2}{(M_1 s^2+C_1 s+K_1)(M_2 s^2+C_2 s+K_2)+M_2 s^2(C_2 s+K_2)} \tag{3.69}$$

$$\frac{z_{1c}}{n}=-\frac{M_2 s^2+C_2 s+K_2}{((M_1 s^2+C_1 s+K_1)(M_2 s^2+C_2 s+K_2)+M_2 s^2(C_2 s+K_2))A(s)} \tag{3.70}$$

The details of the equation derivation is given in Appendix 3.2.2.

As stated in Section 3.4.2, there is possibly disturbances other than the measurement noise, for example the vibration of the vehicle engine in the engine-chassis vibration test example.

The force generated by the engine vibration can be denoted by a disturbance force *v* directly applied to the physical mass M_2, as illustrated in Figure 3.25.

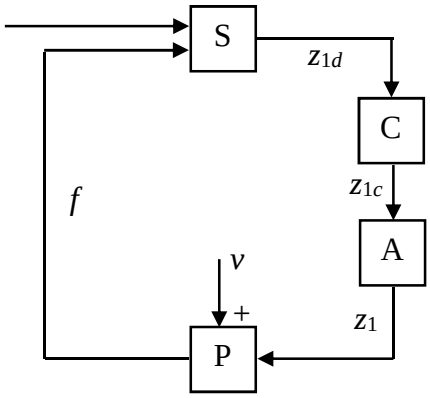

Figure 3.25 MiL system with compensator and disturbance force added to the physical mass

The equations for the MiL system in this example is listed as follows.

$$-f-(C_1 s+K_1)(z_{1d}-z_0)=M_1 s^2 z_{1d} \tag{3.71}$$

$$-(C_2 s+K_2)(z_2-z_1)-v=M_2 s^2 z_2=f \tag{3.72}$$

$$\frac{z_{1c}}{z_{1d}}=\frac{1}{A(s)} \tag{3.73}$$

$$\frac{z_1}{z_{1c}}=A(s) \tag{3.74}$$

The transfer function from the vibration force v to the compensated signal z_{1c} can be shown to be:

$$\frac{z_{1c}}{v}=\frac{M_2 s^2}{\left((M_1 s^2+C_1 s+K_1)(M_2 s+C_2+K_2)+M_2 s^2(C_2 s+K_2)\right)A(s)} \tag{3.75}$$

Compared with the transfer function from the measurement noise n to the compensated signal z_{1c}:

$$\frac{z_{1c}}{v} = -\frac{M_2 s^2}{M_2 s^2 + C_2 s + K_2} \frac{z_{1c}}{n} \tag{3.76}$$

The details of the derivation of equations (3.75) and (3.76) are shown in Appendix 3.2.3.

The transfer function shown in equation (3.76) is plotted in Figure 3.26, using the parameters M_2 = 100 kg, C_2 = 150 Ns/m, and K_2 = 20000 N/m.

By observing Figure 3.26, it can be concluded that, the magnitude of the two transfer functions $\frac{z_{1c}}{n}$ and $\frac{z_{1c}}{v}$ are very close in high frequency range, especially when the frequency is larger than about 10 Hz, with these parameters. The 180° phase difference is actually meaningless, because the direction of the engine vibration force *v* and the noise *n* is user defined.

Because the engine vibration signal is in the high frequency range in this example, the engine vibration *v* can be approximated by a noise *n* in the force feedback.

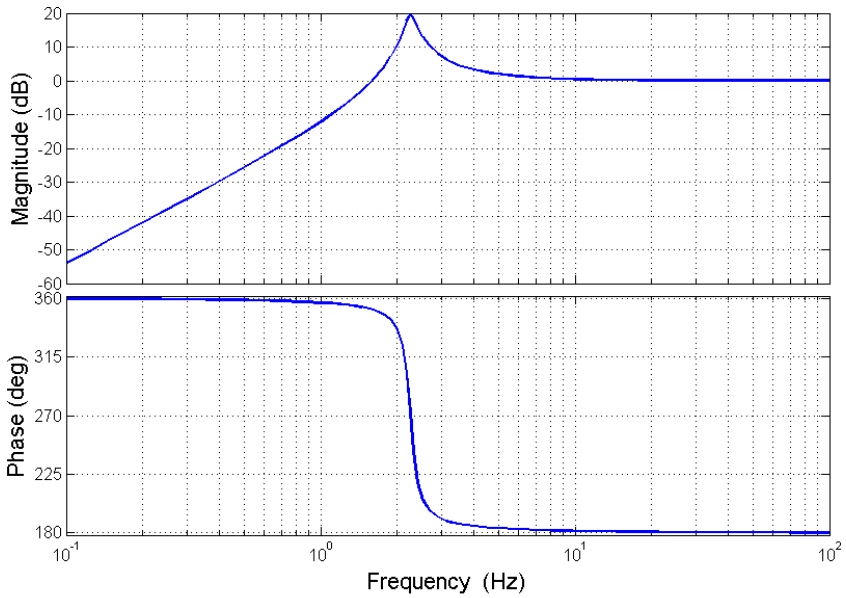

Figure 3.26 Difference between transfer functions $\frac{z_{1c}}{n}$ and $\frac{z_{1c}}{v}$

In the previous examples for the two DOF based MiL system, the characteristics of the MiL system are studied with a very fast “actuator”, the Multi-Axis Simulation Table. However, it may not be necessary to use such a good and expensive actuator for the test. In this section, a brief study of the influence of the dynamic response of the actuator on the performance of the MiL system is given.

Two actuators with different dynamic characteristics are used to analyse the MiL system and to give a comparison.

The transfer functions of the two actuators are given as follows. $A_1(s)$ is the transfer function of the original Multi-Axis Simulation Table, and $A_2(s)$ is simply a “slowed down” version of the MAST.

$$A_1(s) = \frac{1}{(\tau_1 s + 1)(\tau_2 s + 1)(\tau_3 s + 1)} \tag{3.77}$$

$$A_2(s) = \frac{1}{(4\tau_1 s + 1)(4\tau_2 s + 1)(4\tau_3 s + 1)} \tag{3.78}$$

where $\tau_1 = 0.011$, $\tau_2 = 0.0053$, $\tau_3 = 0.0018$.

The frequency response of the transfer functions $A_1(s)$ and $A_2(s)$ is compared in Figure 3.27.

The transfer function of $\frac{z_{1d}}{n}$ and the transfer functions $\frac{z_{1c}}{n}$ with different actuators are plotted in Figure 3.28. It can be concluded from Figure 3.28, in the compensated signal z_{1c}, the noise signal n (or the high frequency vibration force v) is amplified significantly, especially in the high frequency range. With a slower actuator $A_2(s)$, the noise signal n (or the high frequency vibration force v) is more amplified. It is important to notice that this conclusion is based on the condition of compensating the lag of the actuators using an inverse model compensator.

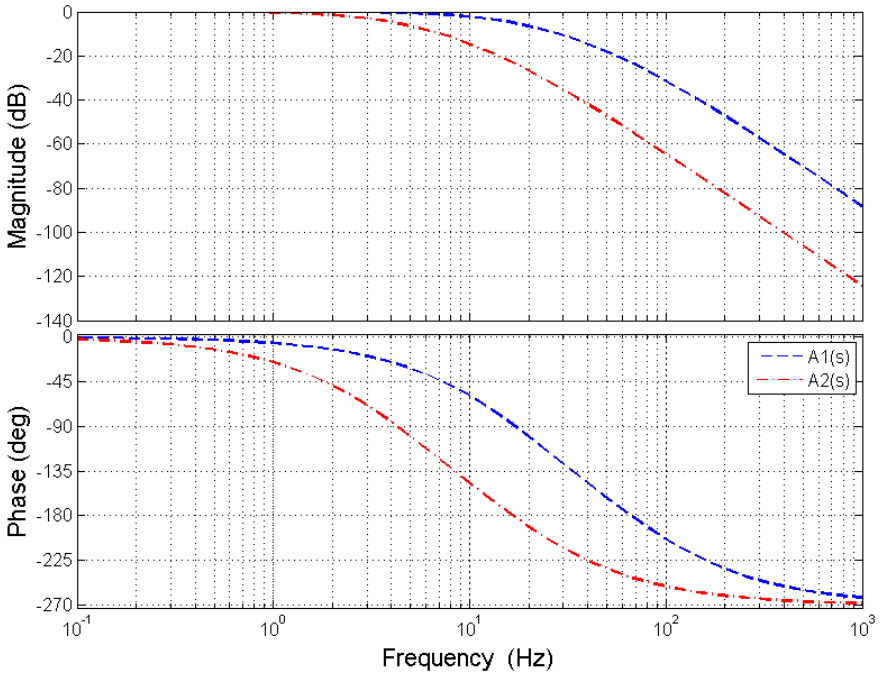

Figure 3.27 Comparing the frequency response of $A_1(s)$ and $A_2(s)$

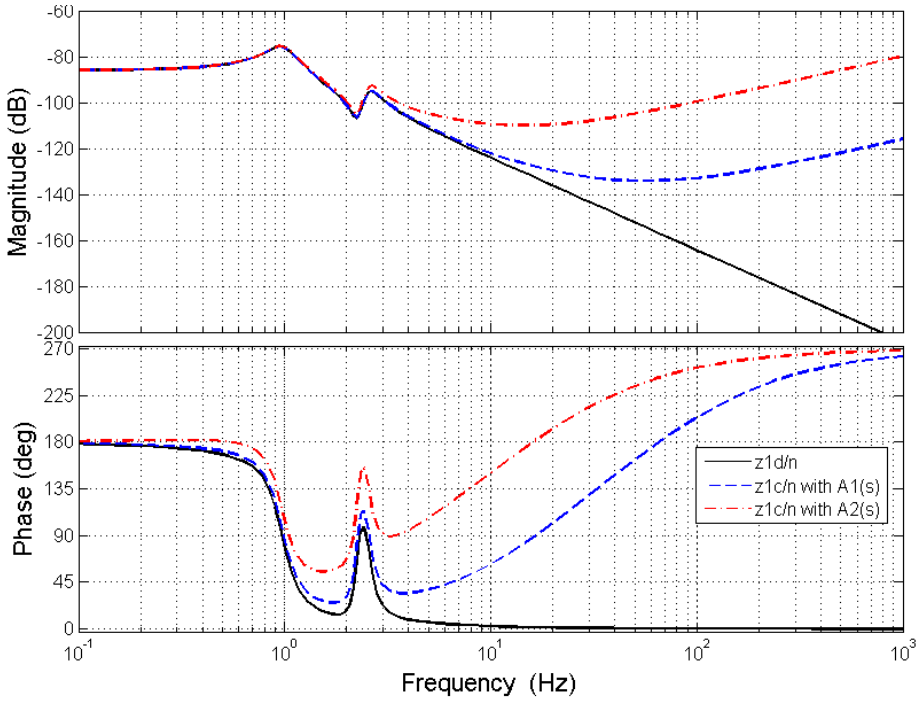

Figure 3.28 Comparing transfer functions $\frac{z_{1d}}{n}$ and $\frac{z_{1c}}{n}$ of the two DOF MiL system

The conclusion is checked with simulation results using Simulink. The diagram of the Simulink model can be found in Appendix 3.1.4. In the simulation, the displacement input z_0 is an integrated white noise to mimic the rough and uneven surface of the road profile while the vehicle is moving, and the noise n (which, as proved earlier in this chapter, can approximate the high frequency engine vibration force in this case) added to the feedback force is a sine wave signal with a magnitude of 10000 N, and with a frequency of 50 Hz (3000 rpm).

The simulation result showing the compensated signal z_{1c} for the system using actuator $A_1(s)$ is illustrated in Figure 3.29.

A zoomed-in graph of the compensated signal z_{1c} for the system using actuator $A_1(s)$ is shown in Figure 3.30.

The simulation result showing the compensated signal z_{1c} for the system using the "slowed down" actuator $A_2(s)$ is presented in Figure 3.31.

A zoomed-in graph of the compensated signal z_{1c} for the system using actuator $A_2(s)$ is shown in Figure 3.32.

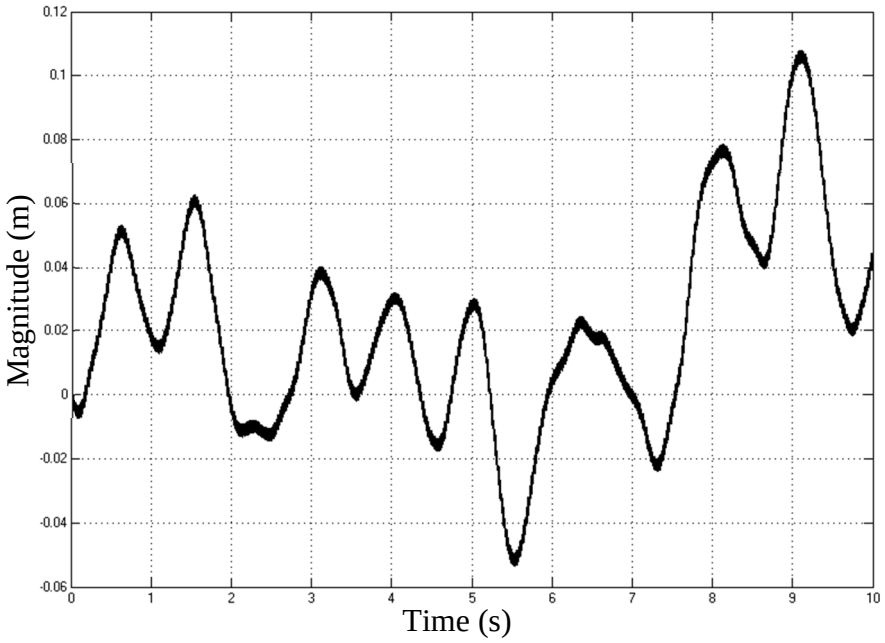

Figure 3.29 Compensated signal z_{1c} in the MiL system using actuator $A_1(s)$

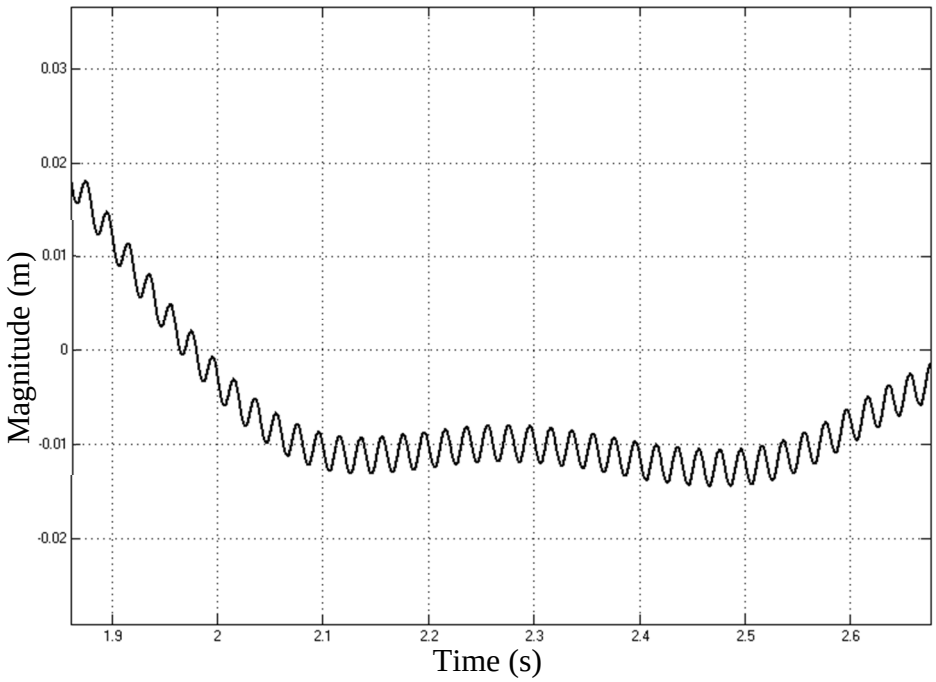

Figure 3.30 Compensated signal z_{1c} in the MiL system using actuator $A_1(s)$, zoomed in

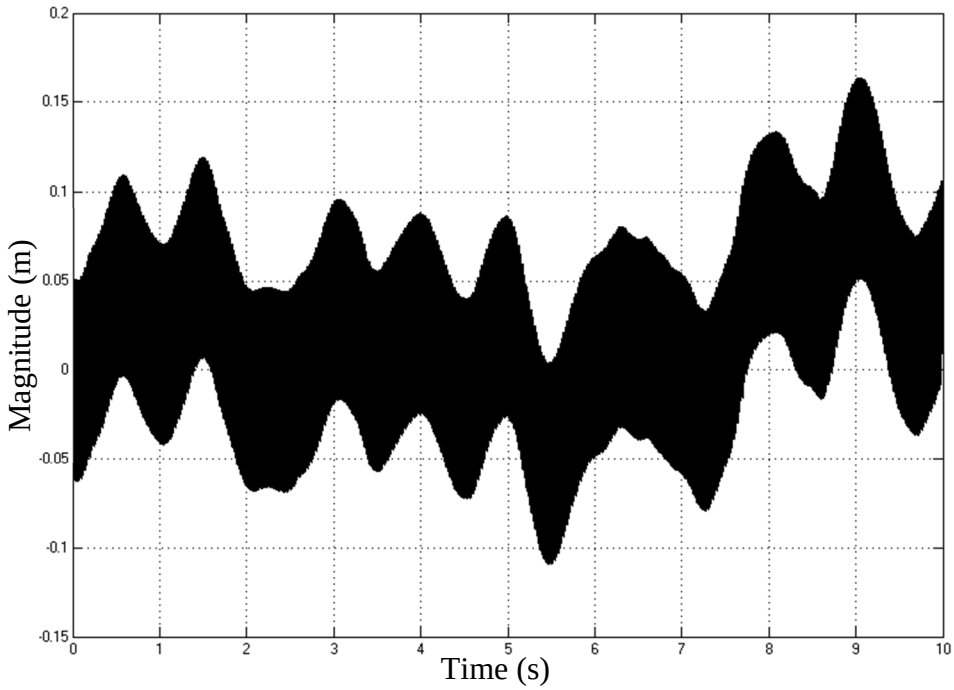

Figure 3.31 Compensated signal z_{1c} in the MiL system using actuator $A_2(s)$

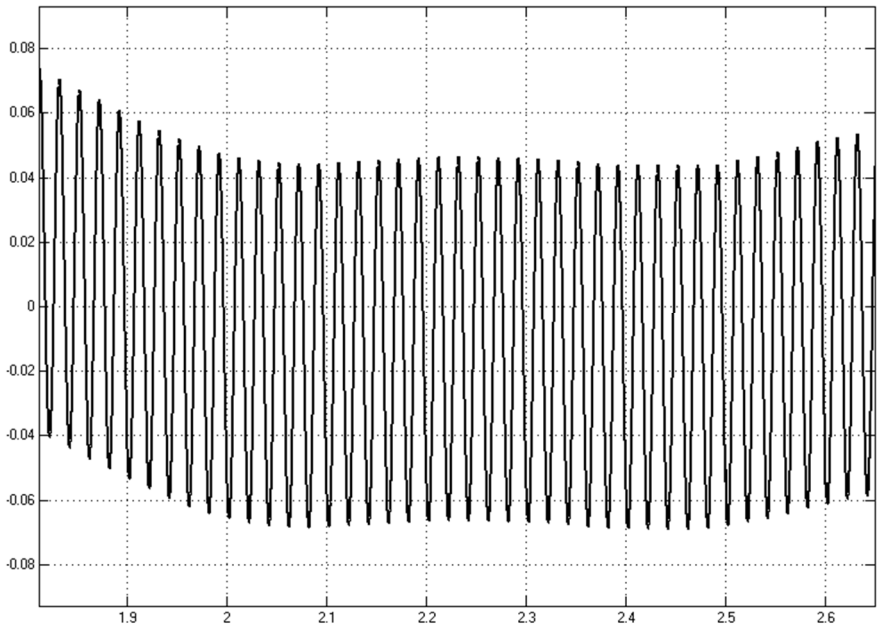

Figure 3.32 Compensated signal z_{1c} in the MiL system using actuator $A_2(s)$, zoomed in

From the simulation result, it can be concluded that in the MiL system using the "faster" actuator $A_1(s)$, the high frequency disturbance force is not magnified very much in the compensated signal, however, for the MiL system with the "slowed down" actuator $A_2(s)$, the high frequency disturbance force is significantly amplified in the compensated signal. The large amplitude and the steep slope of the signal may possibly lead to actuator saturation.

3.6 Concluding Remarks

In this chapter, a general procedure is demonstrated to analyse the MiL test system. The method is presented with two example systems: a single mass-spring-damper MiL system, and a two DOF mass-spring-damper MiL system. Although only these two examples are used for the examples of the analysis, the method can be generalised, and so systems with more degrees of freedom can be analysed with the same approach.

In the analysis, the method of building a MiL test system based on the mathematical model of the whole system is shown: where to split the system, and what signals to use to link the physical subsystem and the numerical subsystem back together. The process of stability analysis is presented for checking the stability margin of the MiL system. The problems introduced by the actuator dynamics and measurement noise are examined. It is shown in simulation that with a relatively slow actuator and realistic measurement noise level, the design of the compensator is challenging, because for a relatively slow actuator, the response to high frequency command signal is more attenuated, hence in the compensator, more high frequency compensation is required for accurate motion of the actuator. Due to the existence of the high frequency measurement noise in the feedback path, saturation of control signal may easily occur. It is difficult to tune the balance between the accuracy of compensation and saturation prevention.

Chapter 4

4 Compensator Design with H_∞ Loop Shaping

As stated in Chapter 3, with a comparably slow actuator, the problem of noise and disturbance amplification may occur in the compensated signal.

A compensator should be designed that is not just the inverse of the mathematical model of the actuator, but has the following characteristics:

1. Keep the sensitivity and accuracy of the system response to the primary input signal z_0.
2. Attenuate the sensitivity to the supplementary disturbance signal v and the unwanted noise n to avoid the problem of actuator saturation.

With such compensator design, the effect of actuators for a specific test can be better understood.

However, the two design targets of the compensator may be contradictory. In some cases, assuming that the frequency spectrums of the primary and supplementary signals are close, if the sensitivity to the frequency domain of the supplementary signal is significantly attenuated, it will inevitably affect the accuracy of the reproduction of the primary signal.

To design a compensator as stated above, H_∞ optimization is introduced. This chapter is divided into 4 sections:

4.1 Principle of H_∞ Loop Shaping for MiL Systems

4.2 Transfer Function Derivation

4.3 H_∞ Loop Shaping with MATLAB/Simulink

4.4 Simulation Results and Discussion

4.5 Concluding Remarks

4.1 Principle of H_∞ Loop Shaping for MiL Systems

In this section, the principle of the application of H_∞ loop shaping to optimize the compensator in the MiL system will be introduced.

The block diagram of a general MiL system with compensator is shown in Figure 4.1.

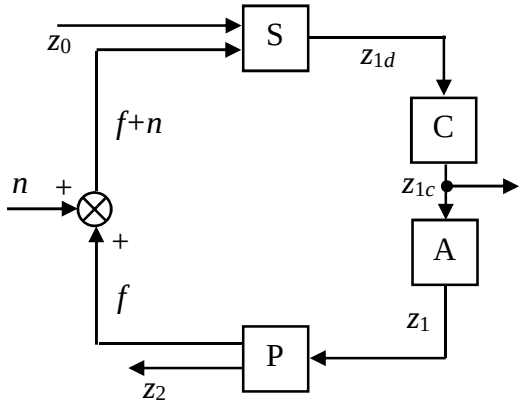

Figure 4.1 MiL system with compensator

In this system, the displacement in the physical subsystem z_2 is defined as the major signal that needs to be accurately reproduced. It can be observed from Figure 4.1 that it is a MIMO system with 2 inputs and 2 outputs. The inputs are the displacement input z_0 and the noise n respectively, and the outputs are the compensated signal z_{1c} and the displacement output z_2.

The target of the H_∞ optimization is to design a compensator C to attenuate the gain of the transfer function $\frac{z_{1c}}{n}$, in the meantime, the controller should allow z_2 to respond to the input z_0 with acceptable accuracy.

To indicate how accurately the MiL system behaves, a reference model is introduced and compared with the MiL system with compensator and actuator models. In the reference model, the numerical model and the physical model are connected directly together (which means the actuator is ideal), as illustrated in Figure 4.2.

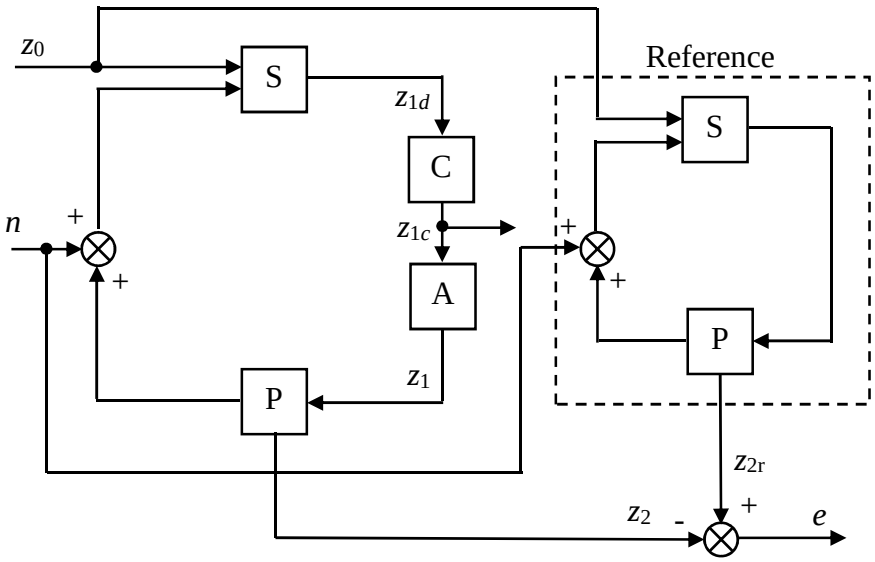

Figure 4.2 MiL model used for H_∞ optimization with reference

The system shown in Figure 4.2 is a 2-input 2-output system. Input 1 is the position input z_0, input 2 is the measurement noise input n. The error e is obtained by comparing the reference displacement z_{2r} to the mass displacement with actuator and compensator model z_2, and the error e is output 1 of the MIMO system, while the compensated signal z_{1c} is taken as output 2 of the system.

The transfer function of system is in the form:

$$\begin{bmatrix} e \\ z_{1c} \end{bmatrix} = \begin{bmatrix} \mathbf{T}_{11} & \mathbf{T}_{21} \\ \mathbf{T}_{12} & \mathbf{T}_{22} \end{bmatrix} \begin{bmatrix} z_0 \\ n \end{bmatrix} \tag{4.1}$$

To simplify the problem, the off-diagonal terms will not be optimized. This means the transfer functions $\frac{z_{1c}}{z_0}$ and $\frac{e}{n}$ will not be taken into account during the H_∞ optimization.

Thus the system for optimization is:

$$\mathbf{T} = \begin{bmatrix} \mathbf{T}_{11} & 0 \\ 0 & \mathbf{T}_{22} \end{bmatrix} \tag{4.2}$$

The H_∞ norm of the system **T** is:

$$\|\mathbf{T}\|_\infty = \left\| \begin{bmatrix} \mathbf{T}_{11} & 0 \\ 0 & \mathbf{T}_{22} \end{bmatrix} \right\|_\infty = \max\left(\|\mathbf{T}_{11}\|_\infty, \|\mathbf{T}_{22}\|_\infty \right) \tag{4.3}$$

Before the H_∞ optimization, the system **T** needs to be weighted, which is a process called loop shaping. [28]

In this example, the two inputs z_0 and n have different characteristics in frequency domain, z_0 has larger energy in low frequency domain, while the energy of n is mainly in relatively high frequency.

Considering the different frequency characteristics of the two inputs, the target of the H_∞ optimization is to determine a compensator C to:

1. Minimize $\mathbf{T}_{11}$, especially in low frequency domain. (To make the error between the H_∞ optimized system and the reference system small)
2. Minimize $\mathbf{T}_{22}$, especially in high frequency domain. (To make the compensated signal less sensitive to the noise)

The weighting function **W** can be defined as a diagonal matrix, which is shown in equation 4.4.

$$\mathbf{W} = \begin{bmatrix} \mathbf{W}_{11} & 0 \\ 0 & \mathbf{W}_{22} \end{bmatrix} \tag{4.4}$$

The weighted system is:

$$\mathbf{T}_1 = \mathbf{W}\mathbf{T} = \begin{bmatrix} \mathbf{W}_{11} & 0 \\ 0 & \mathbf{W}_{22} \end{bmatrix} \begin{bmatrix} \mathbf{T}_{11} & 0 \\ 0 & \mathbf{T}_{22} \end{bmatrix} = \begin{bmatrix} \mathbf{W}_{11}\mathbf{T}_{11} & 0 \\ 0 & \mathbf{W}_{22}\mathbf{T}_{22} \end{bmatrix} \tag{4.5}$$

The H_∞ norm of this system is:

$$\left\|\mathbf{T}_1\right\|_\infty = \left\|\begin{bmatrix} \mathbf{W}_{11}\mathbf{T}_{11} & 0 \\ 0 & \mathbf{W}_{22}\mathbf{T}_{22} \end{bmatrix}\right\|_\infty = \max\left(\left\|\mathbf{W}_{11}\mathbf{T}_{11}\right\|_\infty, \left\|\mathbf{W}_{22}\mathbf{T}_{22}\right\|_\infty\right) \tag{4.6}$$

If after the H_∞ optimization, the achieved minimum norm is:

$$\left\|\mathbf{T}_1\right\|_\infty = \gamma \tag{4.7}$$

It can be deduced that:

$$\max\left(\left\|\mathbf{W}_{11}\mathbf{T}_{11}\right\|_\infty, \left\|\mathbf{W}_{22}\mathbf{T}_{22}\right\|_\infty\right) = \gamma$$

$$\left\|\mathbf{W}_{11}\mathbf{T}_{11}\right\|_\infty \le \gamma \;\&\; \left\|\mathbf{W}_{22}\mathbf{T}_{22}\right\|_\infty \le \gamma$$

$$\left|\mathbf{W}_{11}\mathbf{T}_{11}\right| \le \gamma \;\&\; \left|\mathbf{W}_{22}\mathbf{T}_{22}\right| \le \gamma, \forall\omega$$

$$\left|\mathbf{T}_{11}\right| \le \left|\frac{\gamma}{\mathbf{W}_{11}}\right| \;\&\; \left|\mathbf{T}_{22}\right| \le \left|\frac{\gamma}{\mathbf{W}_{22}}\right|, \forall\omega \tag{4.8}$$

It can be concluded from equation (4.8) that, the inverse of the weighting functions $\left|\frac{1}{\mathbf{W}_{11}}\right|$ and $\left|\frac{1}{\mathbf{W}_{22}}\right|$ define the loop shapes for the transfer functions $\mathbf{T}_{11}$ and $\mathbf{T}_{22}$, and the inverse of the weighting functions multiplied by the achieved minimum H_∞ norm, $\left|\frac{\gamma}{\mathbf{W}_{11}}\right|$ and $\left|\frac{\gamma}{\mathbf{W}_{22}}\right|$, is the real upper boundary limit for $\mathbf{T}_{11}$ and $\mathbf{T}_{22}$.

4.2 Derivation of Transfer Functions

In this section, the method of the derivation of the transfer functions of a generalized MiL system for H_∞ optimization is proposed.

The model as shown in Figure 4.2 is adapted to the model indicated in Figure 4.3, where the numerical model S and the physical testing model P are both split into 2 blocks, for the convenience of transfer function derivation.

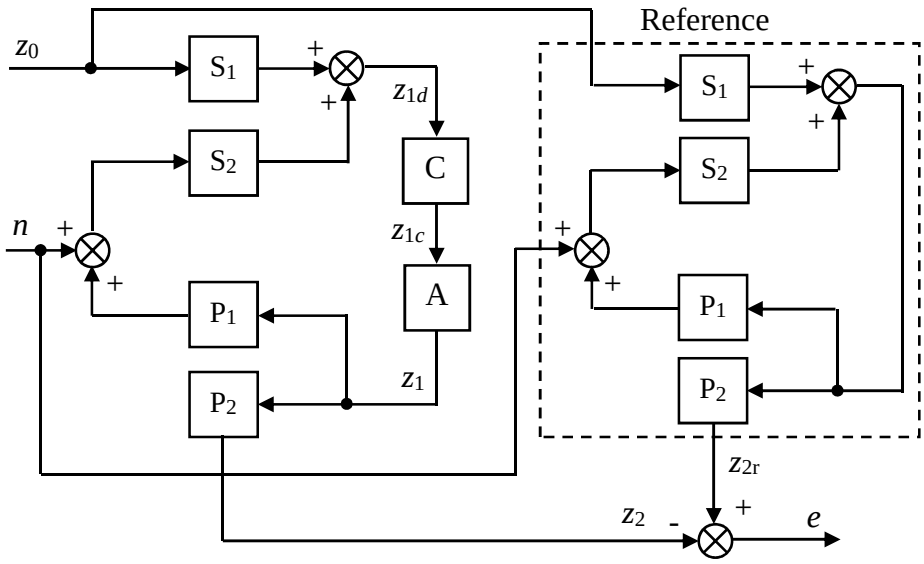

Figure 4.3 MiL model for the transfer function derivation for H_∞ optimization

With the transfer functions of blocks S_1, S_2, P_1, P_2, C and A, the transfer functions $\frac{e}{z_0}$ and $\frac{z_{1c}}{n}$ can be calculated as follows:

$$\mathbf{T}_{11} = \frac{e}{z_0} = \frac{S_1(s)P_2(s)}{1 - S_2(s)P_1(s)} - \frac{C(s)A(s)S_1(s)P_2(s)}{1 - C(s)A(s)S_2(s)P_1(s)} \tag{4.9}$$

$$\mathbf{T}_{22} = \frac{z_{1c}}{n} = \frac{S_2(s)C(s)}{1 - C(s)A(s)S_2(s)P_1(s)} \tag{4.10}$$

4.2.1 Transfer Function Derivation for the Single Mass-spring-damper MiL System

As already proved in Section 3.1.1, the transfer function for the numerical subsystem is given in equation (4.11).

$$z_1 = z_0 - \frac{1}{Cs + K} f \tag{4.11}$$

The transfer functions for blocks S_1 and S_2 is shown as follows:

$$S_1(s) = \frac{z_{1d}}{z_0} = 1 \tag{4.12}$$

$$S_2(s) = \frac{z_{1d}}{f} = -\frac{1}{Cs + K} \tag{4.13}$$

The transfer function for the physical subsystem is given in equation (4.14).

$$Ms^2 z_1 = f \tag{4.14}$$

The transfer function for blocks P_1 and P_2 can be calculated as follows:

$$P_1(s) = \frac{f}{z_1} = Ms^2 \tag{4.15}$$

Because in this specific example, the displacement z_1 is defined as the major signal that needs to be accurately reproduced, so the transfer function for block P_2 is simply:

$$P_2(s) = 1 \tag{4.16}$$

The transfer functions for H_∞ optimization can then be calculated with equations (4.9) and (4.10), using $S_1(s)$, $S_2(s)$, $P_1(s)$, $P_2(s)$, and any compensator and actuator models $C(s)$ and $A(s)$.

4.2.2 Transfer Function Derivation for the Two DOF Mass-spring-damper MiL System

As already proved in Section 3.1.2, the transfer function for the numerical subsystem is given in equation (4.17).

$$-f-(C_1 s+K_1)(z_{1d}-z_0)=M_1 s^2 z_{1d} \tag{4.17}$$

For block S_1, let $f=0$:

$$-(C_1 s+K_1)(z_{1d}-z_0)=M_1 s^2 z_{1d} \tag{4.18}$$

$$S_1(s)=\frac{z_{1d}}{z_0}=\frac{C_1 s+K_1}{M_1 s^2+C_1 s+K_1} \tag{4.19}$$

For block S_2, let $z_0=0$:

$$-f-(C_1 s+K_1)z_{1d}=M_1 s^2 z_{1d} \tag{4.20}$$

$$S_2(s)=\frac{z_{1d}}{f}=-\frac{1}{M_1 s^2+C_1 s+K_1} \tag{4.21}$$

The equation for the physical testing subsystem is:

$$M_2 s^2 z_2=-(C_2 s+K_2)(z_2-z_1)=f \tag{4.22}$$

For block P_1:

$$z_2=\frac{1}{M_2 s^2}f \tag{4.23}$$

Substitute equation (4.23) into equation (4.22):

$$f = -\frac{C_2 s + K_2}{M_2 s^2} f + (C_2 s + K_2) z_1 \tag{4.24}$$

$$P_1(s) = \frac{f}{z_1} = \frac{M_2 C_2 s^3 + M_2 K_2 s^2}{M_2 s^2 + C_2 s + K_2} \tag{4.25}$$

For block P_2, let $f = 0$:

$$M_2 s^2 z_2 = -(C_2 s + K_2)(z_2 - z_1) \tag{4.26}$$

$$P_2(s) = \frac{z_2}{z_1} = \frac{C_2 s + K_2}{M_2 s^2 + C_2 s + K_2} \tag{4.27}$$

The transfer functions for H_∞ optimization can then be calculated with equations (4.9) and (4.10), using $S_1(s)$, $S_2(s)$, $P_1(s)$, $P_2(s)$, and any compensator and actuator models $C(s)$ and $A(s)$.

4.3 H_∞ Loop Shaping with MATLAB/Simulink

In this section, an H_∞ optimization method for a general MiL system is proposed, using existing MATLAB/Simulink tools.

The procedure for the H_∞ loop shaping of the MiL system is as follows:

1. Define the structure of the compensator, the transfer function of which needs to be at least one order higher than the mathematical model of the actuator.
2. Obtain the transfer functions $\mathbf{T}_{11}$ and $\mathbf{T}_{22}$ of the MiL system and construct system $\mathbf{T}$ with the method proposed in Section 4.2, notice that $\mathbf{T}_{12} = \mathbf{T}_{21} = 0$
3. Calculate the original H_∞ norms for $\mathbf{T}_{11}$ and $\mathbf{T}_{22}$, named by $\overline{\gamma_{11}}$ and $\overline{\gamma_{22}}$ respectively.

4. Weight the system **T**:

$$\mathbf{T}_1 = \mathbf{WT} = \begin{bmatrix} \mathbf{W}_{11} & 0 \\ 0 & \mathbf{W}_{22} \end{bmatrix} \begin{bmatrix} \mathbf{T}_{11} & 0 \\ 0 & \mathbf{T}_{22} \end{bmatrix} = \begin{bmatrix} \mathbf{W}_{11}\mathbf{T}_{11} & 0 \\ 0 & \mathbf{W}_{22}\mathbf{T}_{22} \end{bmatrix}$$

5. Tune the compensator with MATLAB function hinfstruct.

   The hinfstruct function is intended for tuning fixed-structure controllers. The advantage of fixed-structure H_∞ tuning is that, the structure and the order of the controller is defined by the user, while with the traditional H_∞ synthesis, the optimized controller can be of very high order, making it difficult to implement.

As an example of choosing the weights in step 4, consider the 2 DOF mass-spring-damper system.

Here $\mathbf{W}_{11} = \frac{n_1}{\gamma_{11}} L_1$, where L_1 is a low-pass filter, with a steady state gain of 1, describing the frequency response of the road profile input z_0, and n_1 is a user defined parameter to indicate how much difference is allowed between the H_∞ optimized system and the ideal system. By default n_1 is set to be 1, however sometimes it can be assigned to a value smaller than 1 to relax the boundary limit.

And $\mathbf{W}_{22} = \frac{n_2}{\gamma_{22}} L_2$, where L_2 is a high-pass filter, the gain of which converges to 1 when the frequency approaches infinity, defining the frequency range of the measurement noise n or the high frequency disturbance force v, and n_2 is a user defined parameter to adjust the magnitude of attenuation of the compensated signal z_{1c}. The larger the value of n_2, the more the signal fluctuation excited by the noise n or the high frequency disturbance force v is attenuated.

The inverse of the original H_∞ norms $\frac{1}{\gamma_{11}}$ and $\frac{1}{\gamma_{22}}$ is multiplied to the weighting functions, in order to make the H_∞ optimization equally sensitive to the two design targets of making the error between the H_∞ optimized system and the reference system

small, and making the compensated signal less sensitive to the high frequency disturbances and the measurement noise.

Examples of the MATLAB code for H_∞ tuning of the MiL systems are provided in Appendix 4.1 and 4.2. In Appendix 4.1, the example is for the H_∞ optimization of the single mass-spring-damper based MiL system, and in Appendix 4.2, the example is for the H_∞ optimization of the two DOF mass-spring-damper based MiL system.

4.4 Simulation Results and Discussion

4.4.1 Simulation Results for the Single Mass-spring-damper MiL System

In this section, the H_∞ loop shaping method for the optimization of the compensator is verified by simulation results using the MiL system built from the single mass-spring-damper example.

The parameters are set to: M = 400 kg, C = 4000 Ns/m, K = 16000 N/m. Note that the emulated system has a natural frequency of 1Hz, and damping ratio of 0.79.

And the actuator model is the same as that shown in section 3.2.1:

$$A(s) = \frac{1}{0.00006079s^3 + 0.005046s^2 + 0.0812s + 1} \tag{4.28}$$

The initial configuration for the compensator is inverse model based:

$$C(\mathrm{s}) = \frac{\left(0.00006079s^3 + 0.005046s^2 + 0.0812s + 1\right)\left(\tau_n + 1\right)}{\left(\tau_d s + 1\right)^4} \tag{4.29}$$

It can be seen from equation (4.29) that the initial condition of the compensator C is the inverse model of the actuator $\left(0.00006079s^3 + 0.005046s^2 + 0.0812s + 1\right)$

multiplied by one added zero and 4 additional poles, where $\tau_n = \tau_d = 0.01$. Note that the additional zero cancels one of the poles, and they are only there to define the order of the compensator. The transfer function of the compensator needs to be at least one order higher than the mathematical model of the actuator. This has been found to be necessary in order to give enough flexibility in the adjustment of the compensator. In this specific example, the actuator is 3rd-order, so additional zero and poles are added to the compensator model to make it 4th-oder.

The MATLAB code for the H_∞ optimization of the compensator can be found in Appendix 4.1.1, and the block diagram of the Simulink model used for the verification of the optimized compensators can be found in Appendix 4.2.1.

First of all, the frequency response of the transfer function of $\mathbf{T}_{11}$ (which is the transfer function from the input displacement z_0 to the error e) before and after the optimization is plotted from Figure 4.4 to Figure 4.7.

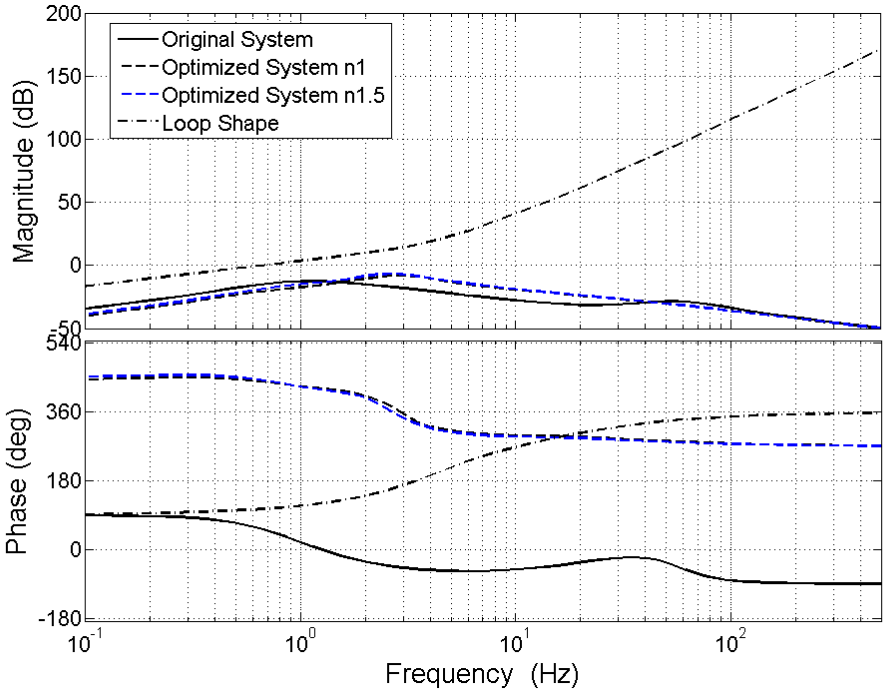

Figure 4.4 The H_∞ optimization results for $\mathbf{T}_{11}$ with different settings of n_2, and loop shape $\frac{1}{\mathbf{W}_{11}}$

In Figure 4.4, the black solid line indicates the frequency response of T_{11} before the H_∞ optimization, the black dash-dotted line shows the frequency response of the inverse of the weighting function $\left|\frac{1}{\mathbf{W}_{11}}\right|$. $\mathbf{W}_{11}$ remains unchanged during the simulation. The black dash line and the blue dash line show the frequency response of $\mathbf{T}_{11}$ after the optimization, with n_2 (which is as defined in Section 4.3) equal to 1 and 1.5 respectively.

To make a clearer observation of the change of the transfer function of $\mathbf{T}_{11}$ with different optimization settings, Figure 4.4 is zoomed in and shown in Figure 4.5.

It can be observed that, although the weighting function $\mathbf{W}_{11}$ remains unchanged, the error increases slightly with the increasing number of n_2. (Recall that n_2 indicates how much the high frequency signal excited by the measurement noise n in the compensated signal z_{1c} is attenuated) This is reasonable because with more high frequency signal attenuated in the compensated signal z_{1c}, it is inevitable that the error between the H_∞ optimized system and the reference signal will increase.

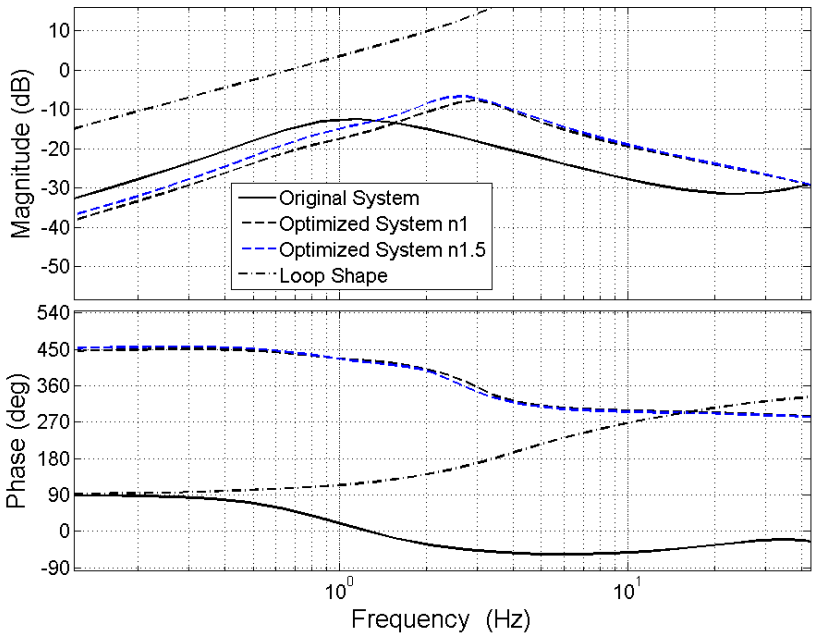

Figure 4.5 The H_∞ optimization results for $\mathbf{T}_{11}$ with different settings of n_2, and loop shape $\frac{1}{\mathbf{W}_{11}}$, zoomed in

In Figure 4.6, the black solid line and all the dash lines are the same with those of Figure 4.4, while the black dash-dotted line and the blue dash-dotted line show the frequency responses of real upper boundary limits, with n_2 equal to 1 and 1.5 respectively.

To make a clearer observation of the change of the transfer function of $\mathbf{T}_{11}$ with different optimization settings, Figure 4.6 is zoomed in and shown in Figure 4.7.

It can be observed from Figure 4.7 that the supremum of $\mathbf{T}_{11}$ locates on the real upper boundary limit $\left|\frac{\gamma}{\mathbf{W}_{11}}\right|$ for each setting of n_2.

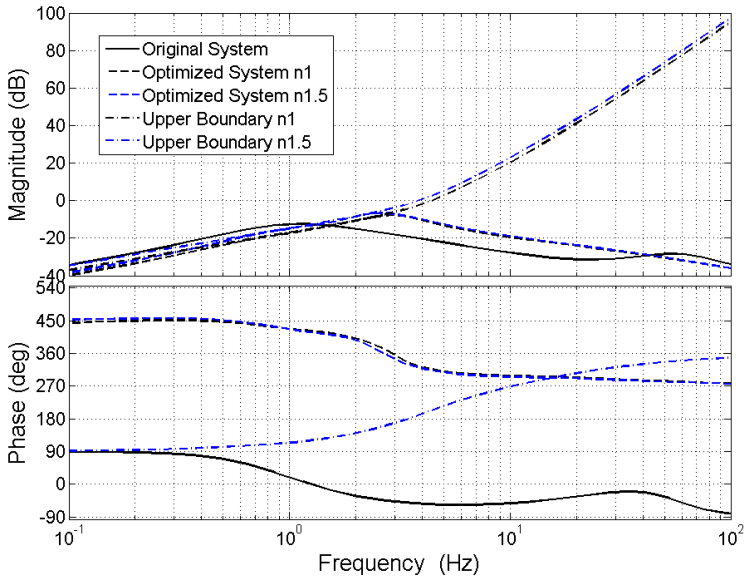

Figure 4.6 The H_∞ optimization results for $\mathbf{T}_{11}$ with different settings of n_2, and upper boundaries $\frac{\gamma}{\mathbf{W}_{11}}$

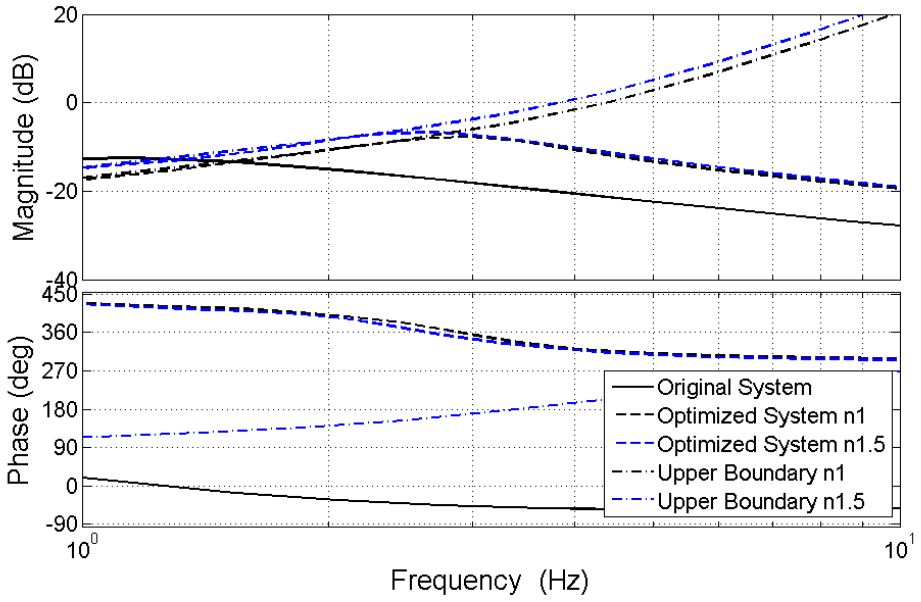

Figure 4.7 The H_∞ optimization results for T_{11} with different settings of n_2, and upper boundaries $\frac{\gamma}{\mathbf{W}_{11}}$, zoomed in

The frequency response of the transfer function of $\mathbf{T}_{22}$ (which is the transfer function from the measurement noise n to the compensated signal z_{1c}) before and after the optimization is plotted in Figure 4.8 and Figure 4.9.

In Figure 4.8, the black solid line indicates the frequency response of $\mathbf{T}_{22}$ before the H_∞ optimization, the black dash-dotted line and the blue dash-dotted line indicate the frequency responses of the inverse of the weighting functions $\left|\frac{1}{\mathbf{W}_{22}}\right|$, with n_2 equal to 1 and 1.5 respectively. The black dash line and the blue dash line show the frequency responses of T_{22} after the optimization, with n_2 equal to 1 and 1.5 respectively.

It is observable that, with larger number of n_2, the signal in high frequency range will be more attenuated.

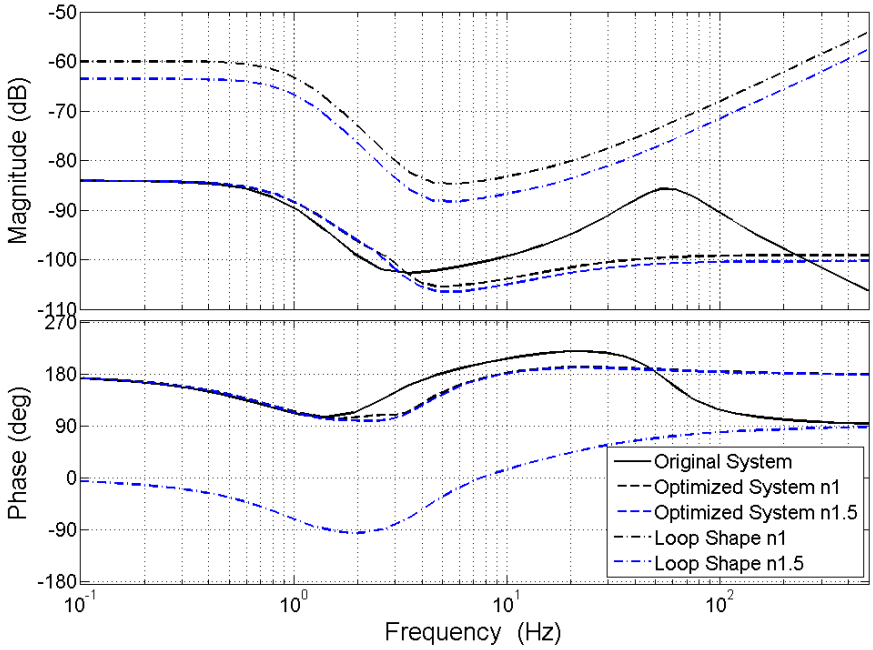

Figure 4.8 The H_∞ optimization results for T_{22} with different settings of n_2, and loop shapes $\frac{1}{\mathbf{W}_{22}}$

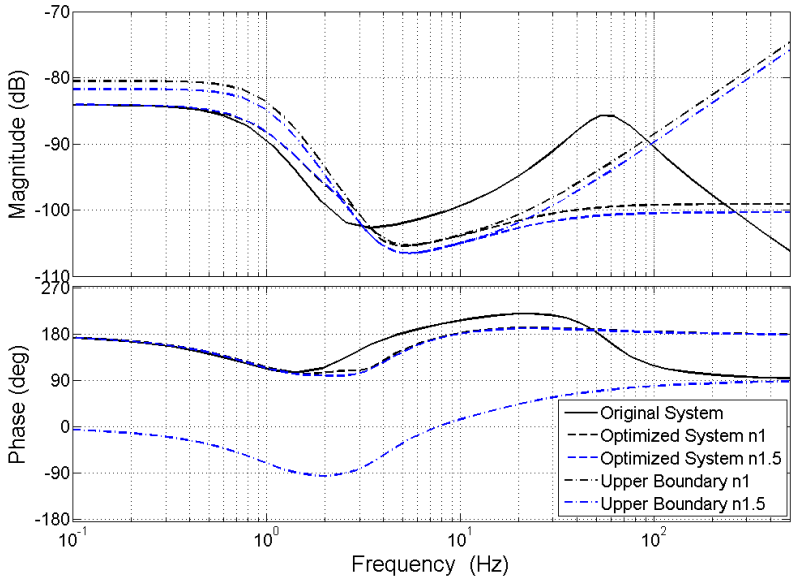

Figure 4.9 The H_∞ optimization results for T_{22} with different settings of n_2, and upper boundaries $\frac{\gamma}{\mathbf{W}_{22}}$

In Figure 4.9, the black solid line and all the dash lines are the same with those of Figure 4.8, while the black dash-dotted line and the blue dash-dotted line show the frequency responses of real upper boundary limits $\left|\frac{\gamma}{\mathbf{W}_{22}}\right|$, with n_2 equal to 1 and 1.5 respectively. It can be observed from Figure 4.9 that the supremum of $\mathbf{T}_{22}$ is on the real upper boundary limit $\left|\frac{\gamma}{\mathbf{W}_{22}}\right|$ for each setting of n_2.

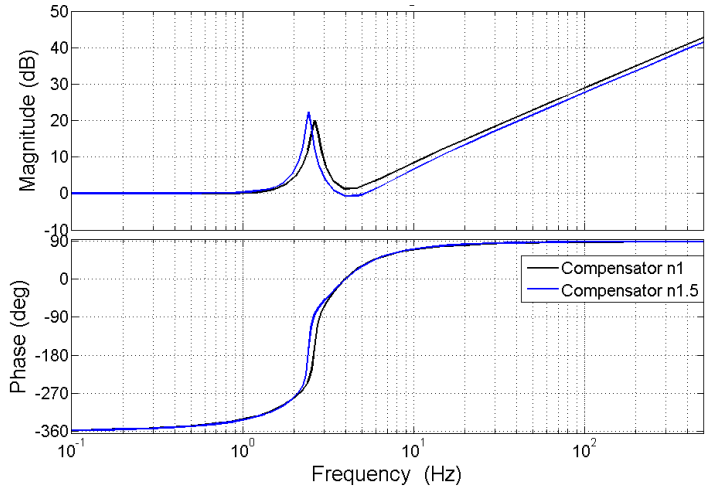

Figure 4.10 The frequency responses of the H_∞ tuned compensators

The frequency responses of the two H_∞ tuned compensators are compared in Figure 4.10.

The effectiveness of the optimized compensators is examined with Simulink, compared with the inverse model compensator, the transfer function of which is:

$$C(s) = 0.00006079s^3 + 0.005046s^2 + 0.0812s + 1 \tag{4.29}$$

The simulation results comparing the compensated signal z_{1c} with and without the added noise to the feedback force using the inverse model compensator was shown in Figure 3.25, it was concluded in section 3.4.1 that the high frequency noise is significantly amplified in the compensated signal.

The simulation results comparing the compensated signal z_{1c} with and without the added noise using the H_∞ optimized compensators are shown from Figure 4.11 to Figure 4.14.

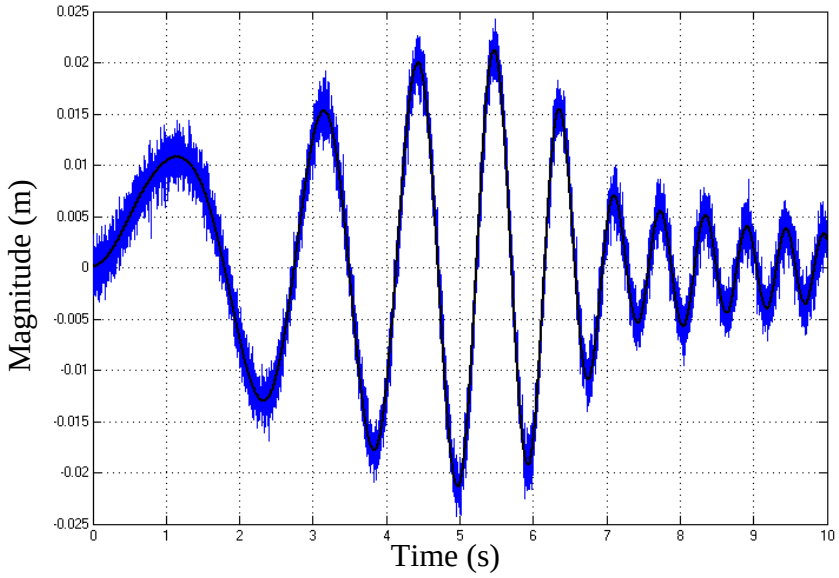

Figure 4.11 Compensated signal z_{1c} with and without the added noise using the H_∞ optimized compensator with $n_2 = 1$

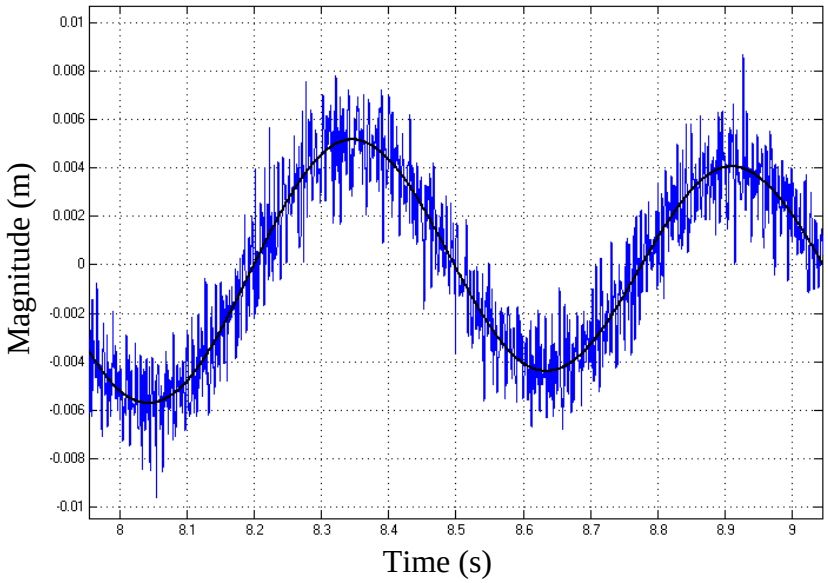

Figure 4.12 Compensated signal z_{1c} with and without the added noise using the H_∞ optimized compensator with $n_2 = 1$, zoomed in

In Figure 4.11, the simulation results are shown with the system using the H_∞ optimized compensator, when the parameter $n_2 = 1$. The black solid line represents the compensated signal z_{1c} with no noise added to the system, and the blue solid line shows the compensated signal z_{1c} with additional noise in the system. The specification of the noise is exactly the same as that in the simulation for the inverse model compensator.

To clearly observe the magnitude of the compensated signal, Figure 4.11 is zoomed in and shown in Figure 4.12. The root mean square value of the noise shown in Figure 4.11 and Figure 4.12 is 0.0014.

From Figure 4.11 and Figure 4.12, it can be concluded, the high frequency noise excited by the measurement noise in the force feedback path is significantly attenuated in the system with the H_∞ optimized compensator, compared with the system using the inverse model compensator. (Recall that when using the inverse model compensator, the root mean spare value of the noise is 0.0035.)

In Figure 4.13, the simulation results are shown with the system using the H_∞ optimized compensator, when the parameter $n_2 = 1.5$.

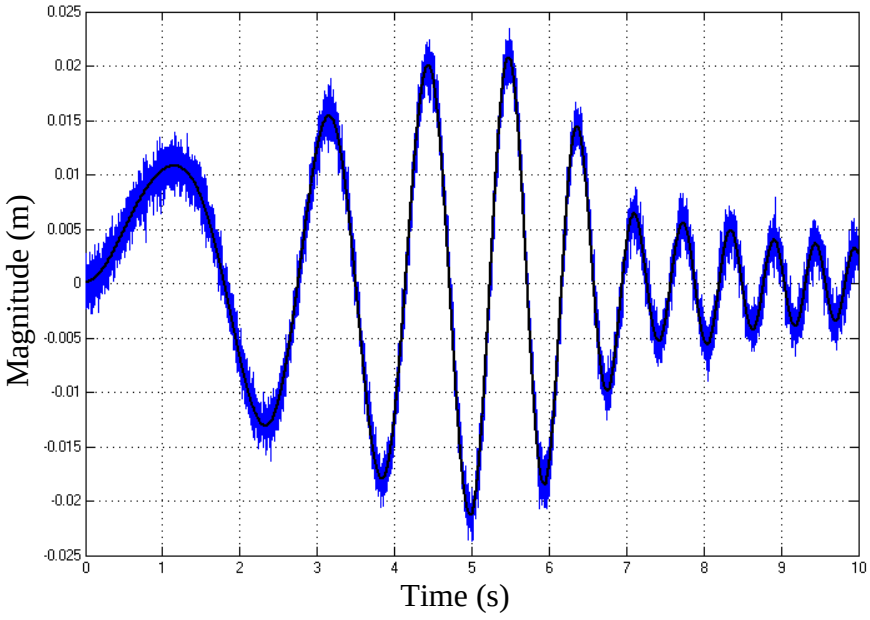

Figure 4.13 Compensated signal z_{1c} with and without the added noise using the H_∞ optimized compensator with $n_2 = 1.5$

In Figure 4.13, the black solid line represents the compensated signal z_{1c} with no noise added to the system, and the blue solid line shows the compensated signal z_{1c} with additional noise in the system. The specification of the noise is exactly the same as that in the simulation for the inverse model compensator and the H_∞ optimized compensator with $n_2 = 1$.

To clearly observe the magnitude of the compensated signal, Figure 4.13 is zoomed in and shown in Figure 4.14. The root mean square value of the noise shown in Figure 4.13 and Figure 4.14 is 0.0011.

It can be concluded from Figure 4.13 and Figure 4.14 that, the high frequency noise excited by the measurement noise in the force feedback path is further attenuated in the system with the H_∞ optimized compensator using the larger value of n_2.

The displacement outputs z_1 are also compared, between the reference system, where the output of the numerical subsystem is connected directly to the physical subsystem, and the H_∞ tuned compensators, as illustrated from Figure 4.15 to Figure 4.18.

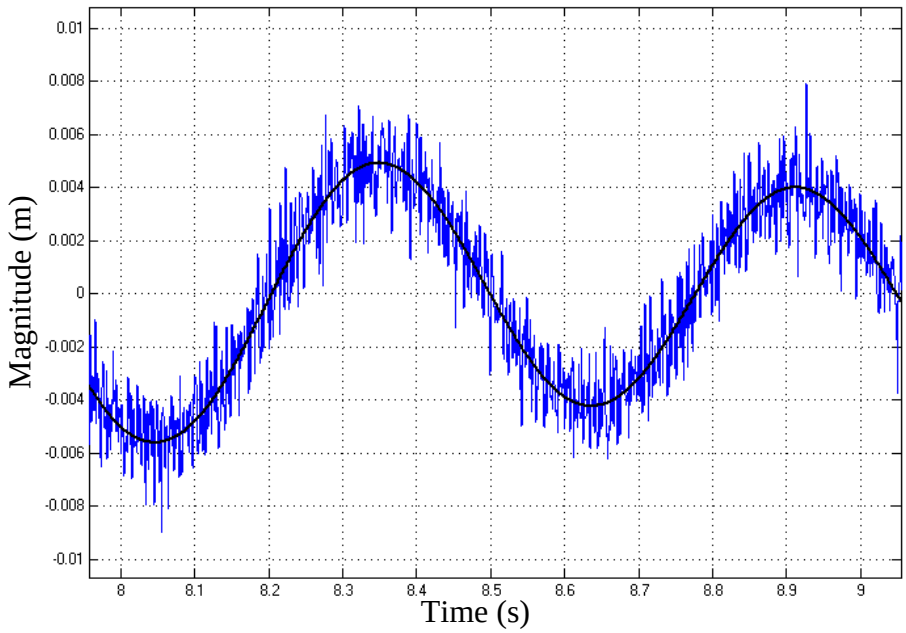

Figure 4.14 Compensated signal z_{1c} with and without the added noise using the H_∞ optimized compensator with $n_2 = 1.5$, zoomed in

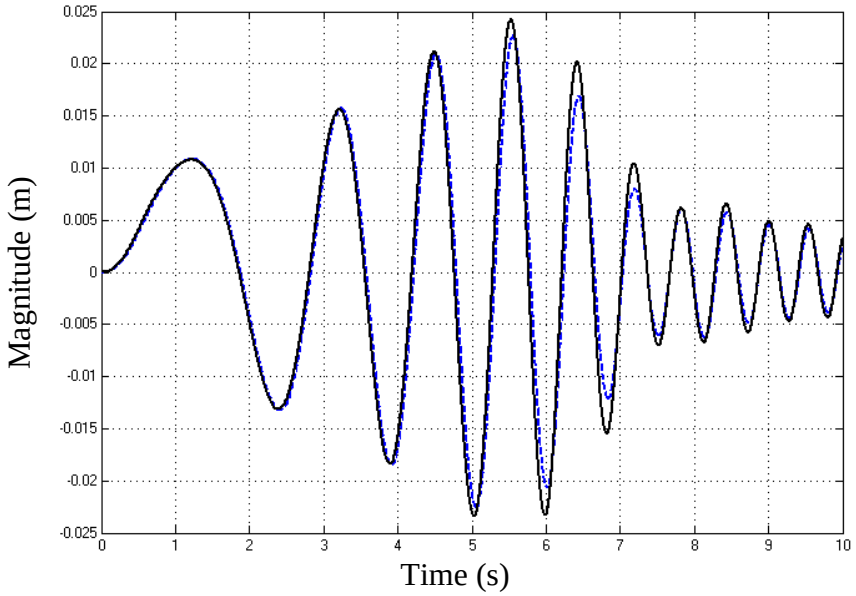

Figure 4.15 Comparison of the displacement z_1 in the reference system (black solid line) and in the system using the H_∞ optimized compensator with $n_2 = 1$ (blue dash line)

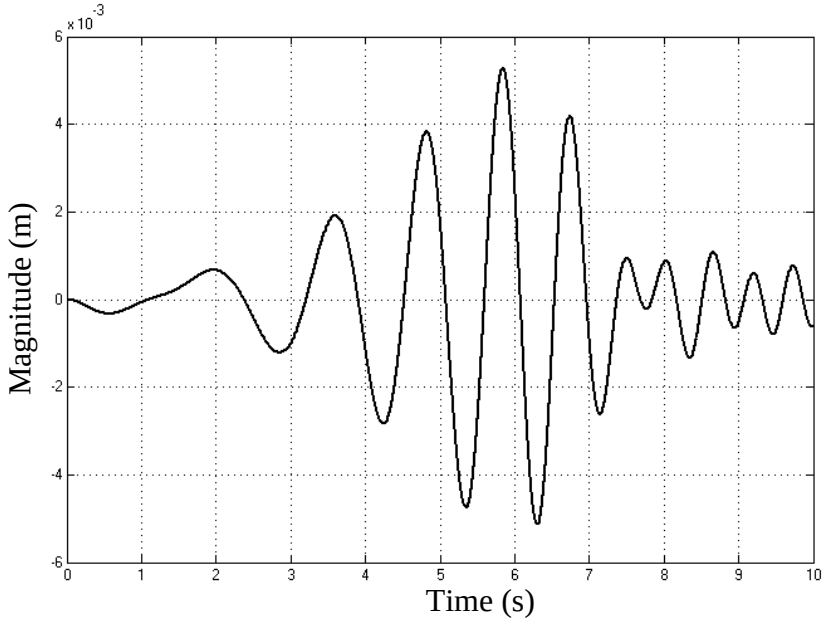

Figure 4.16 The error between z_1 in the reference system and that in the system using the H_∞ optimized compensator with $n_2 = 1$

It can be seen in Figure 4.15 that there is some error in the H_∞ optimized system with $n_2 = 1$, which has verified the increase of error in some frequency ranges after the H_∞ optimization, as already shown in Figure 4.6 and Figure 4.7.

The magnitude of the error between the displacement z_1 in the reference system and that in the H_∞ optimized system with n_2 =1 is illustrated in Figure 4.16.

From Figure 4.17, it is obvious that the error is even larger in the H_∞ optimized system with the parameter n_2 =1.5 than in the H_∞ optimized system with the parameter n_2 =1, which verified the conclusion that the error increases slightly with the increasing number of n_2.

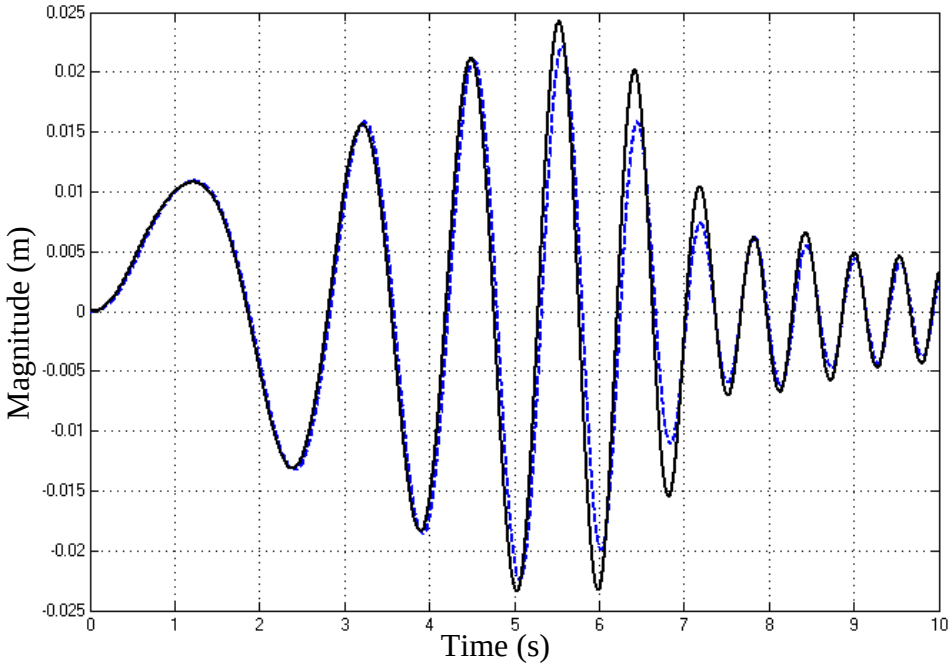

Figure 4.17 Comparison of the displacement z_1 in the reference system (black solid line) and in the system using the H_∞ optimized compensator with n_2 = 1.5 (blue dash line)

The magnitude of the error between the displacement z_1 in the reference system and that in the H_∞ optimized system with n_2 =1.5 is plotted in Figure 4.18.

The selection of the parameter n_2 depends on the situation. A balance needs to be made between how much high frequency noise in the compensated signal has to be attenuated and how much accuracy in the output displacement can be sacrificed.

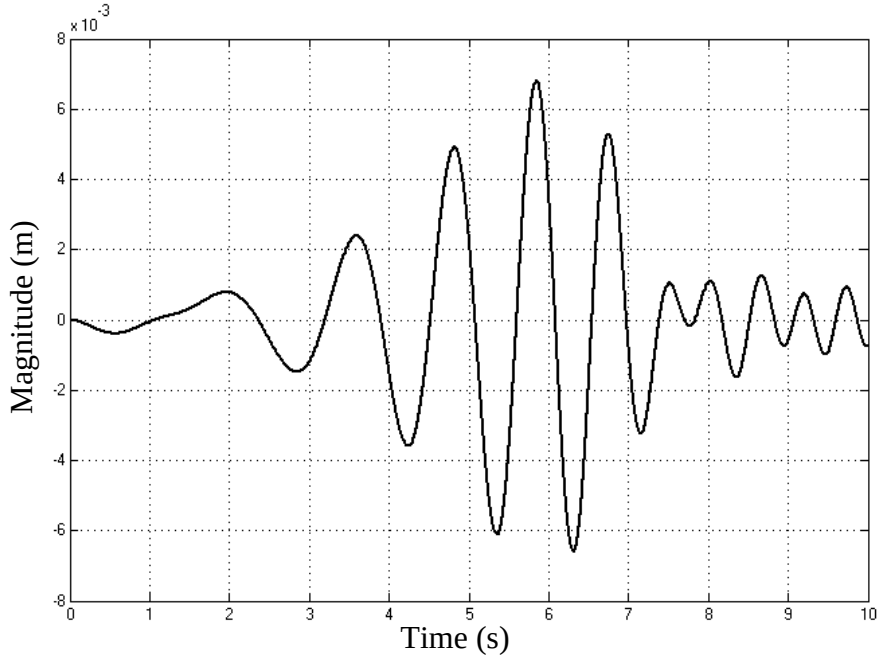

Figure 4.18 The error between z_1 in the reference system and that in the system using the H_∞ optimized compensator with $n_2 = 1.5$

4.4.2 Simulation Results for the Two DOF Mass-spring-damper MiL System

In this section, the H_∞ loop shaping method for the optimization of the compensator is verified by simulation results using the MiL system built from the two DOF mass-spring-damper example.

The parameters are set to: M_1 = 415 kg, C_1 = 1000 Ns/m, K_1 = 20000 N/m, M_2 = 100 kg, C_2 = 100 Ns/m, and K_2 = 20000 N/m.

In this example, the actuator chosen is a slowed down version of the MAST shaking table, the transfer function of which is:

$$A_2(s) = \frac{1}{(2\tau_1 s + 1)(2\tau_2 s + 1)(2\tau_3 s + 1)} \tag{4.34}$$

where $\tau_1 = 0.011$, $\tau_2 = 0.0053$, $\tau_3 = 0.0018$.

The initial configuration for the compensator is inverse model based:

$$C(s) = \frac{(2\tau_1 s+1)(2\tau_2 s+1)(2\tau_3 s+1)(\tau_n+1)}{(\tau_d s+1)^4} \tag{4.35}$$

It can be seen from equation (4.35) that the initial condition of the compensator C is the inverse model of the actuator $(2\tau_1 s+1)(2\tau_2 s+1)(2\tau_3 s+1)$ multiplied by one added zero and 4 additional poles. The same as the example in section 4.4.1, it is noticeable that the additional zero cancels one of the poles, and they are only there to define the order of the compensator. Additional zero and poles are added to the compensator model to make it 4th-order, just to give enough flexibility in the adjustment of the compensator. In this example, $\tau_n = \tau_d = 0.00001$, which means the additional zero and poles only come into effect in very high frequency range (10^5 rad/s).

The frequency response of the initial configuration of the compensator is shown in Figure 4.19 as the blue solid line, compared with the frequency response of the inverse model compensator, which is plotted in black dash line.

The MATLAB codes for the H_∞ optimization of the compensator can be found in Appendix 4.1.2, and the block diagram of the Simulink model used for the verification of the optimized compensators can be found in Appendix 4.2.2.

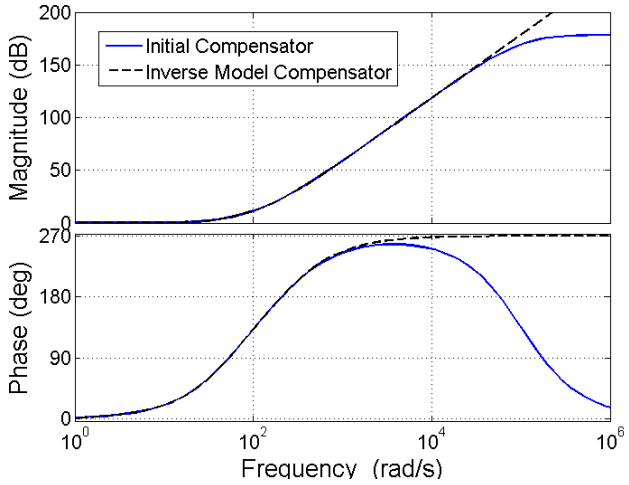

Figure 4.19 Comparison of the Initial Compensator and the Inverse Model Compensator

First of all, the frequency response of the transfer function of $\mathbf{T}_{11}$ (which is the transfer function from the input displacement z_0 to the error e) before and after the optimization is plotted in Figure 4.20 and Figure 4.21.

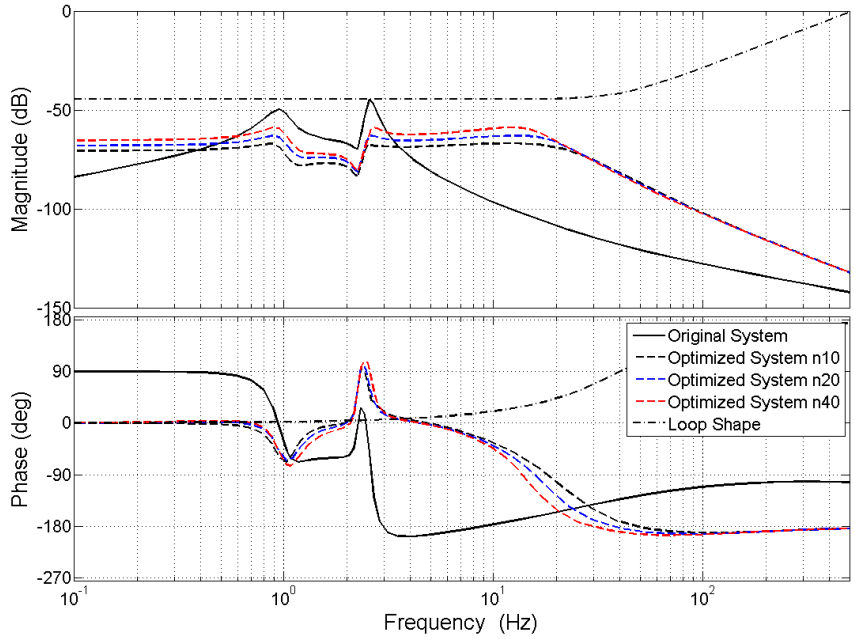

Figure 4.20 The H_∞ optimization results for $\mathbf{T}_{11}$ with different settings of n_2, loop shapes

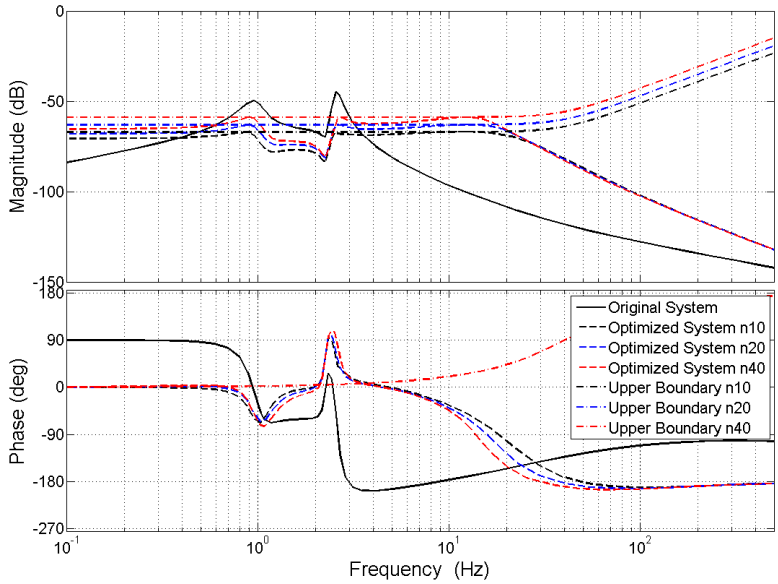

Figure 4.21 The H_∞ optimization results for $\mathbf{T}_{11}$ with different settings of n_2, real upper boundary limits

In Figure 4.20, the black solid line indicates the frequency response of $\mathbf{T}_{11}$ before the H_∞ optimization, the red dash-dotted line shows the frequency response of the inverse of the weighting function $\left|\frac{1}{\mathbf{W}_{11}}\right|$. $\mathbf{W}_{11}$ remains unchanged during the simulation. The black dash line, the blue dash line and the red dash line show the frequency response of $\mathbf{T}_{11}$ after the optimization, with n_2 equal to 10, 20, and 40 respectively.

It can be observed that, although $\mathbf{W}_{11}$ remains unchanged, the error increases with the increasing number of n_2. This is reasonable because with more high frequency signal attenuated in the compensated signal z_{1c}, it is inevitable that the error between the H_∞ optimized system and the reference signal will increase.

In Figure 4.21, the black solid line and all the dash lines are the same as those of Figure 4.20, while the black dash-dotted line, the blue dash-dotted line and the red dash-dotted line shows the frequency responses of real upper boundary limits $\left|\frac{\gamma}{\mathbf{W}_{11}}\right|$, with n_2 equal to 10, 20, and 40 respectively. It can be observed from Figure 4.22 that the supremum of $\mathbf{T}_{11}$ is located on the real upper boundary limit $\left|\frac{\gamma}{\mathbf{W}_{11}}\right|$ for each setting of n_2.

The frequency response of the transfer function of $\mathbf{T}_{22}$ (which is the transfer function from the vibration force v to the compensated signal z_{1c}) before and after the optimization is plotted in Figure 4.22 and Figure 4.23.

It is observable that, with larger number of n_2, the signal in high frequency domain will be more attenuated.

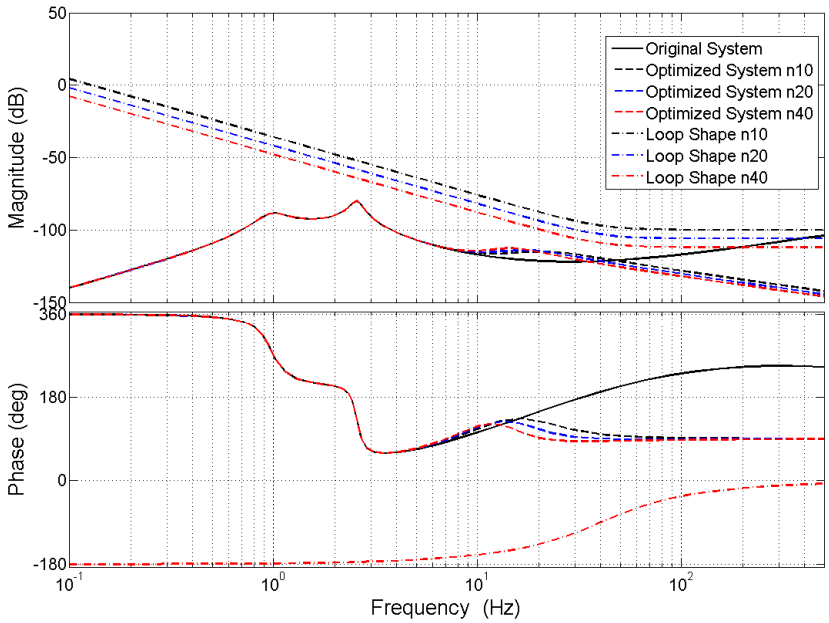

Figure 4.22 The H_∞ optimization results for T_{22} with different settings of n_2, loop shapes

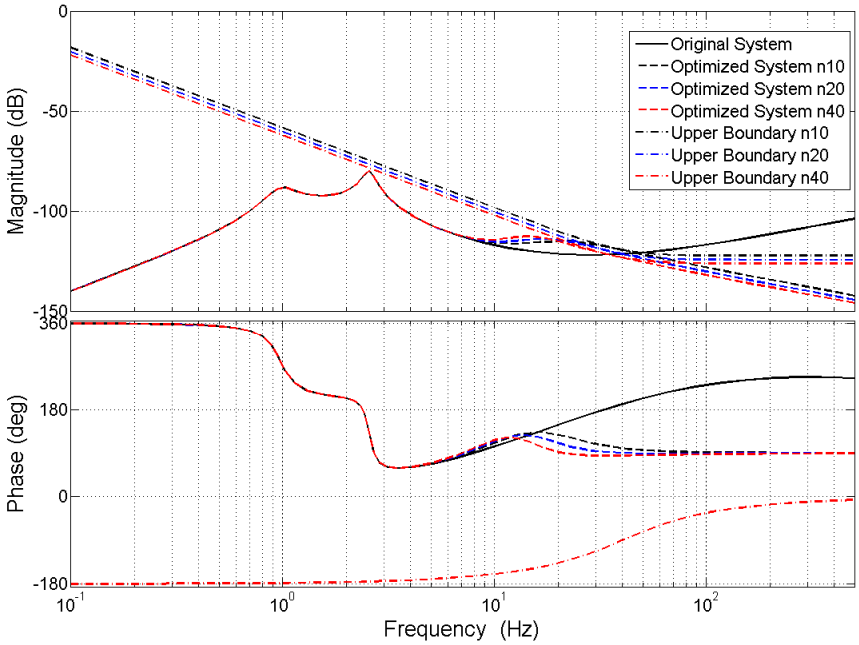

Figure 4.23 The H_∞ optimization results for T_{22} with different settings of n_2, real upper boundary limits

The frequency responses of the three H_∞ tuned compensators and the inverse model compensator are compared in Figure 4.24.

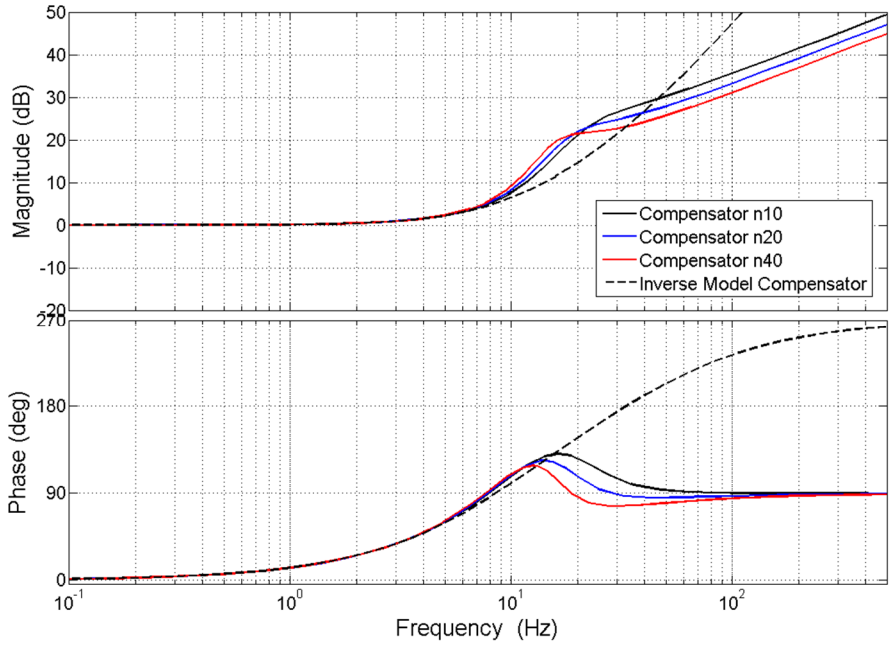

Figure 4.24 The frequency responses of the H_∞ tuned compensators

The effectiveness of the optimized compensators is examined with Simulink, compared with the initial compensator, the transfer function was shown in equation (4.35).

From Figure 4.25 to Figure 4.30, the black solid line shows the compensated signal z_{1c} using the initial compensator, the blue dash line shows the compensated signal z_{1c} using the H_∞ tuned compensator, where the user defined parameters are $n_2 = 10$, $n_2 = 20$, $n_2 = 40$ respectively.

It can be observed from Figure 4.25 to Figure 4.30 that with a larger value of n_2, the high frequency component excited by the additional vibration force will be further attenuated.

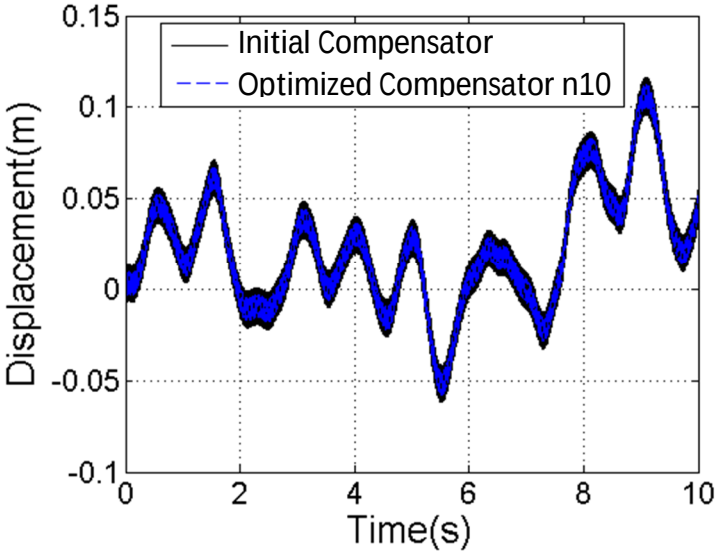

Figure 4.25 Comparison of the compensated signal using the initial compensator and the H_∞ optimized compensator, with $n_2 = 10$

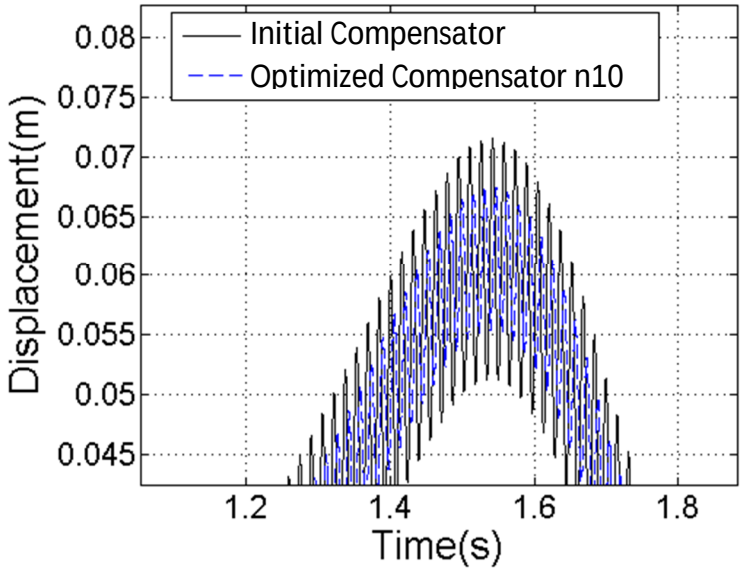

Figure 4.26 Comparison of the compensated signal using the initial compensator and the H_∞ optimized compensator, with $n_2 = 10$, zoomed in

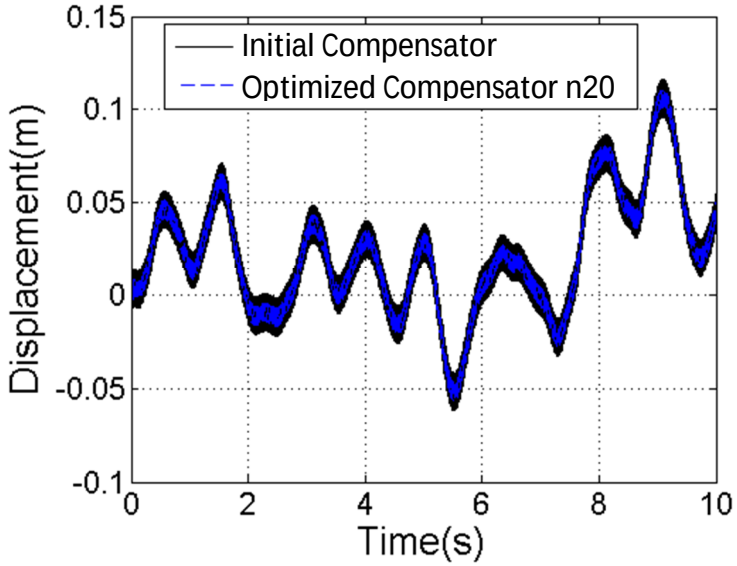

Figure 4.27 Comparison of the compensated signal using the initial compensator and the H_∞ optimized compensator, with $n_2 = 20$

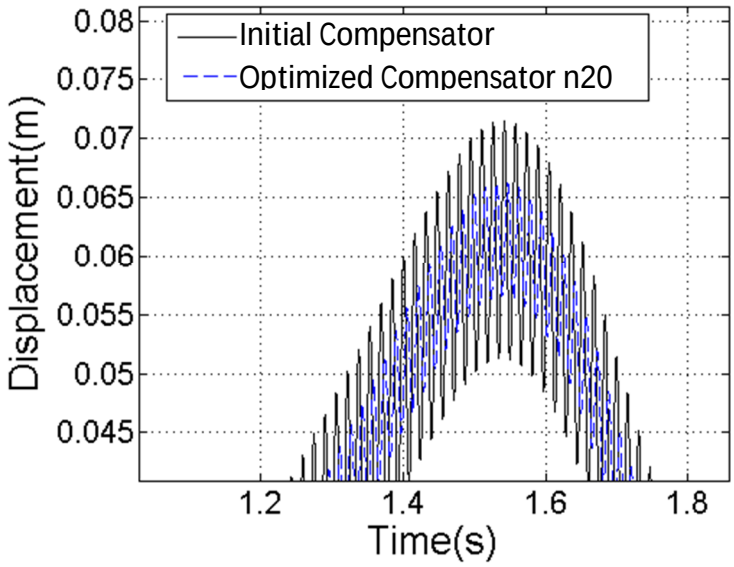

Figure 4.28 Comparison of the compensated signal using the initial compensator and the H_∞ optimized compensator, with $n_2 = 20$, zoomed in

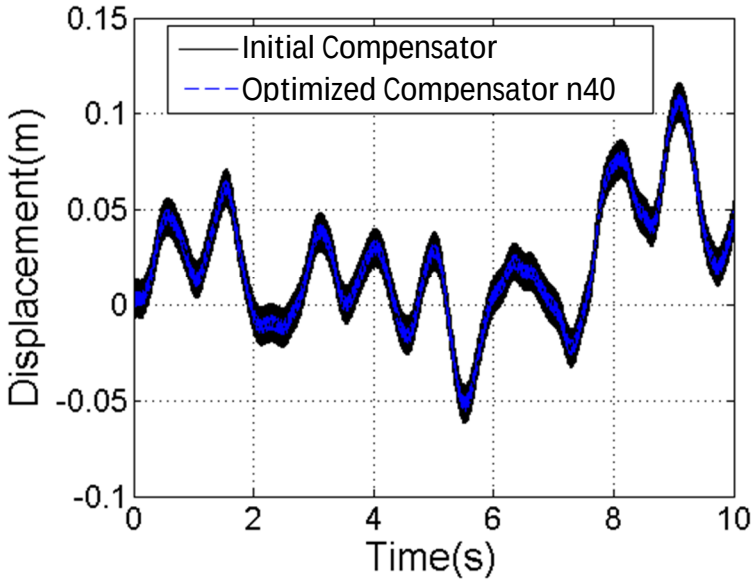

Figure 4.29 Comparison of the compensated signal using the initial compensator and the H_∞ optimized compensator, with $n_2 = 40$

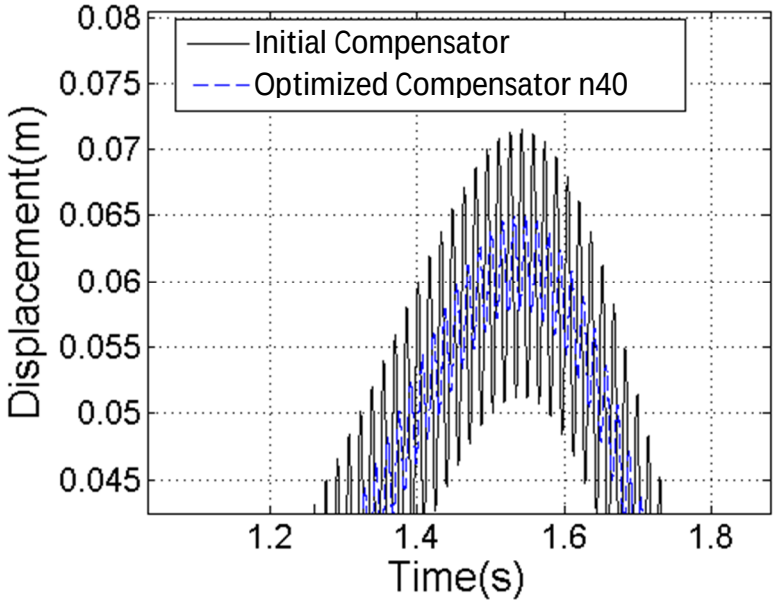

Figure 4.30 Comparison of the compensated signal using the initial compensator and the H_∞ optimized compensator, with $n_2 = 40$, zoomed in

The displacement output z_2 is also compared, between the reference system and the system with the H_∞ tuned compensators. Because with any values of n_2, the error is not discernible, thus only the simulation result with n_2 equal to 40 is shown, as illustrated in Figure 4.31 and Figure 4.32.

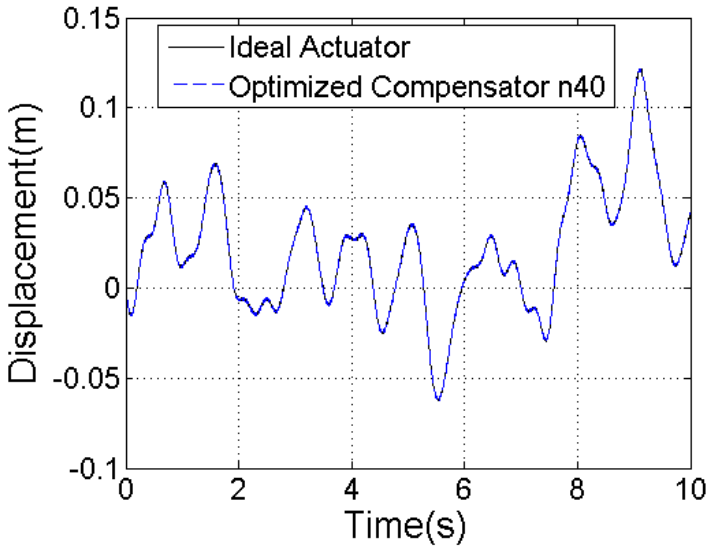

Figure 4.31 Comparison of the displacement z_2 in the reference system and in the system using the H_∞ optimized compensator with n_2 = 40

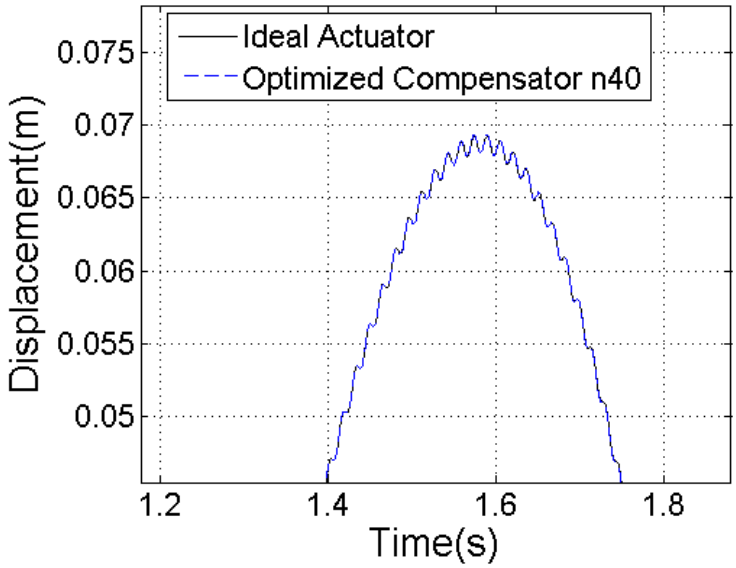

Figure 4.32 Comparison of the displacement z_2 in the reference system and in the system using the H_∞ optimized compensator with n_2 = 40, zoomed in

To see the difference more clearly, the error between the displacement z_2 with the ideal actuator and the H_∞ optimized compensator is plotted from Figure 4.33 to Figure 4.35, with different numbers of user defined parameter n_2. It can be observed that although the error increase with larger number of n_2, the error is below 4×10^{-5} meters, which is negligible.

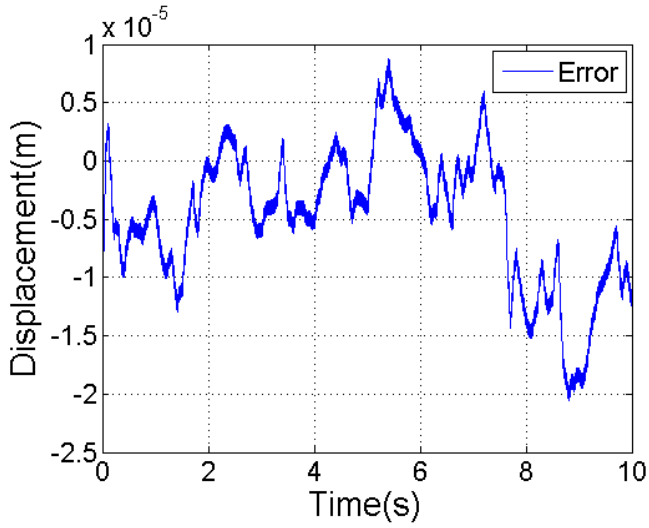

Figure 4.33 Error, $n_2 = 10$

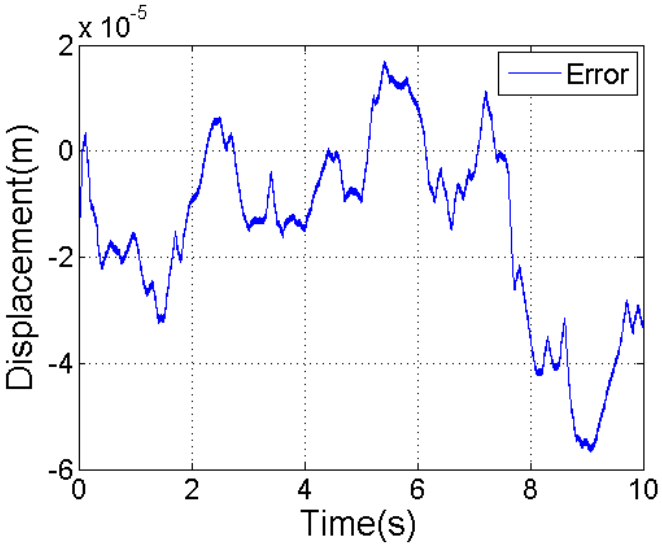

Figure 4.34 Error, $n_2 = 20$

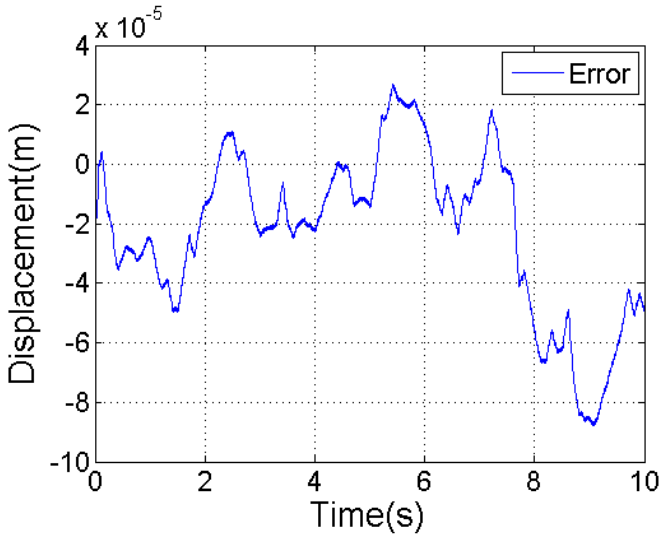

Figure 4.35 Error, $n_2 = 40$

With all settings of n_2, there is almost no observable difference in the vehicle body displacement output between the system using H_∞ tuned compensator and the system with the ideal compensator. Although the high frequency signal is attenuated in the compensated signal, it seems that the high frequency signal in the vehicle body displacement output is not significantly affected.

As stated previously, the H_∞ optimized compensator has better phase characteristics than the initial compensator $C(s) = \frac{(2\tau_1 s+1)(2\tau_2 s+1)(2\tau_3 s+1)(\tau_n+1)}{(\tau_d s+1)^4}$ ($\tau_n = \tau_d =$ 0.00001) in some of the frequency ranges. The proof is shown in Figure 4.36.

In Figure 4.36, the simulation result of the displacement z_2 is shown, in this case, the road profile input is a single frequency sine wave (the frequency is 2 Hz), and there's no engine vibration input.

It can be observed that there's a minor lag between the signal with the ideal actuator and the signal with the inverse model based compensator, however the time delay is even smaller using the H_∞ optimized compensator, making the system using the H_∞ compensator very close to the system with the ideal actuator.

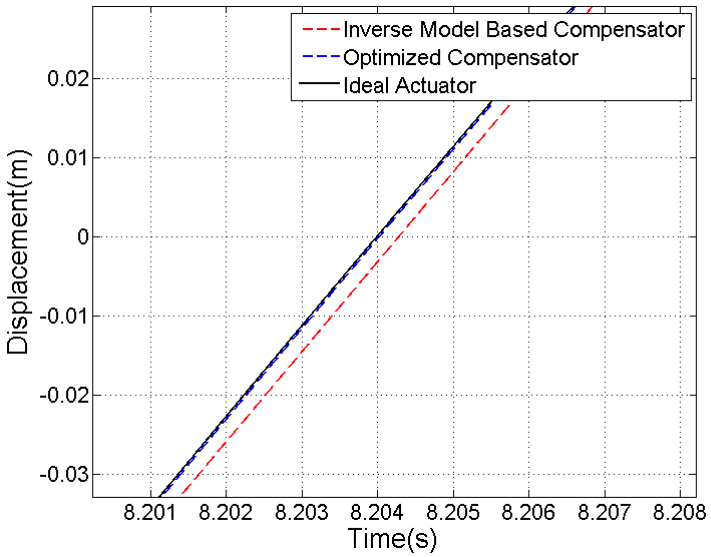

Figure 4.36 Comparing the displacement z_2 with the initial compensator, the H_∞ optimized compensator and the ideal actuator (reference)

It can be concluded from Figure 4.41 that, the phase lift effect of the H_∞ optimized compensator makes it better than the inverse model based compensator in certain frequency ranges.

4.5 Concluding Remarks

In this chapter, a compensator design approach based on H_∞ loop shaping is presented. For the optimization, a two-input two-output system is constructed, with the input position demand and the measurement noise as the two inputs, and the target testing result error and the compensated signal as the two outputs. It is shown with simulation results that the H_∞ optimized compensator not only compensates for the actuator dynamics accurately and effectively attenuates the high frequency response in the compensated signal excited by the measurement noise, but the phase lift effect of the H_∞ optimized compensator makes it even better than the implemented inverse model based compensator in reducing the time delay in certain frequency ranges.

Chapter 5

5 Experimental Verification

In this chapter, the compensator design method based on H_∞ optimization, which is proposed in Chapter 4, is verified with experimental results. A two-axis robotic arm based on a limb of the Italian Institute of Technology HyQ robot was used for the experiment.

This chapter is divided into 6 sections:

5.1 The Two-axis Robot Arm System

5.2 Generating a MiL Testing System with the Robot Arm

5.3 Results with no Compensator

5.4 Results with Inverse Model Compensator

5.5 Results with Low-Pass Filtered Inverse Model Compensator

5.6 Results with H_∞ Optimized Compensator

5.7 Concluding Remarks

5.1 The Two-axis Robot Arm System

The test rig used for the MiL test example is a two-axis robotic arm based on a limb of the Italian Institute of Technology HyQ robot [29]. The geometry of the robot arm is shown in Figure 5.1.

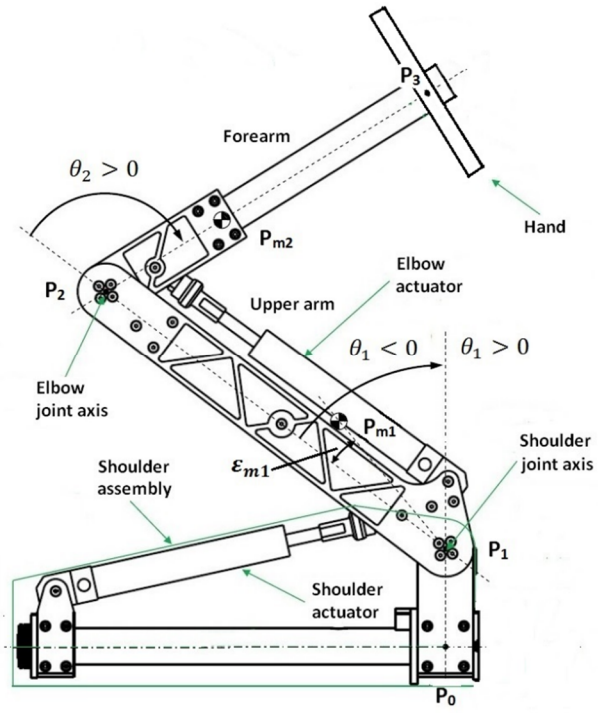

Figure 5.1 The geometry of the robot arm [30]

The hydraulic control system for the robot arm was built by Du et al. [30]. The hydraulic circuit is illustrated in Figure 5.2. The power source of the system is a fixed capacity pump, driven by an AC brushless servo motor. Two direct drive control valves receive analogue signals from the controller, and drive two unequal area actuators, which are for the shoulder joint and the elbow joint respectively.

The controller for the two-axis robot arm is implemented with an xPC environment. An xPC target and 2 NI PCI-6221 data acquisition cards are employed as the real-time control platform. The angular positions of the joints are measured by incremental encoders, and proportional-integral (PI) controllers are used for local position control of each joint. A load cell is attached to each of the actuators, and the measured shoulder force is used for the MiL test.

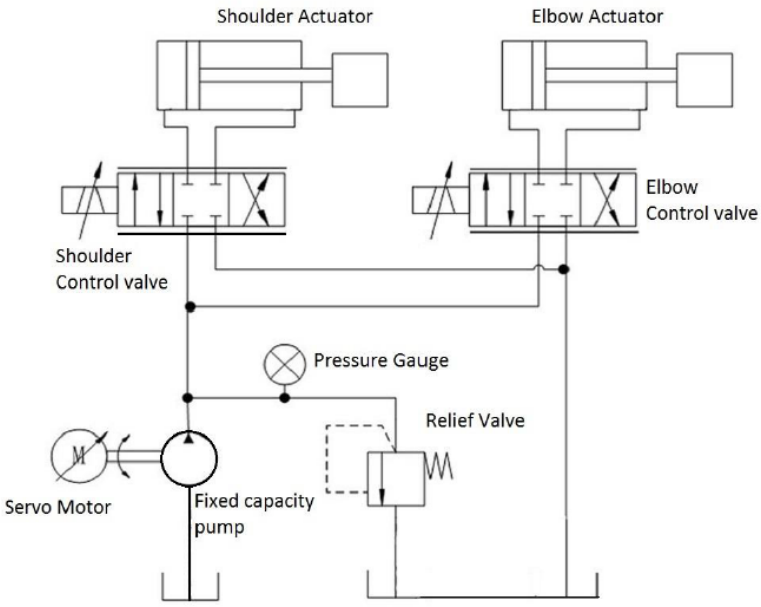

Figure 5.2 The hydraulic circuit of the two-axis robot arm [30]

More details about the xPC system can be found in [30] . The picture of the two-axis robot arm testing rig is shown in Figure 5.3.

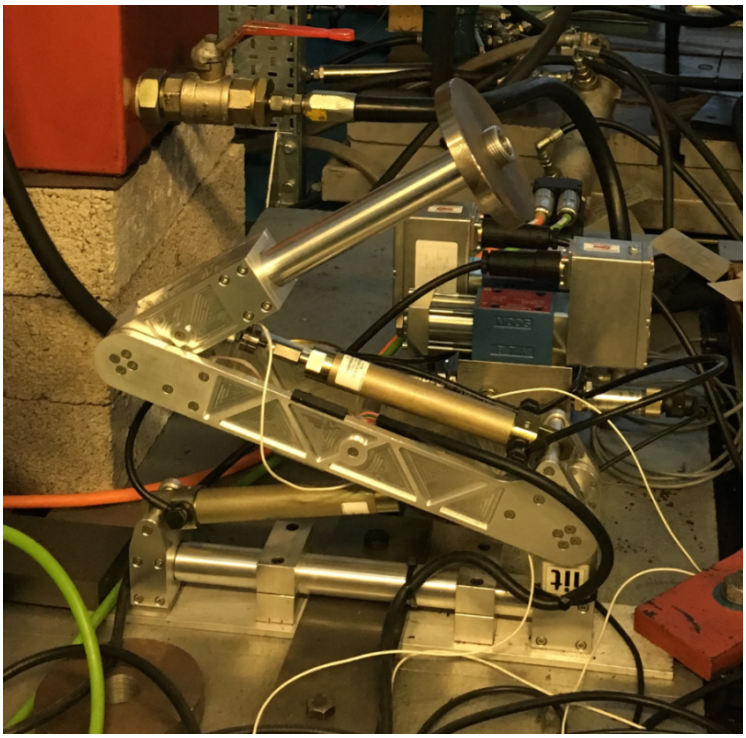

Figure 5.3 The two-axis robot arm testing rig

The dimensions and specifications of the robot arm is shown in Table 5.1:

Shoulder Assembly	
$P_0P_1(d_{13})$	0.08m
Mass M_{r0}	2.482 kg (including the shoulder actuator)
Inertia I_0	0.00745 kgm^2 (with respect to torso abduction/adduction axis, through P_0)
d_{11}	0.32 m
d_{12}	0.045 m
a_1	0.3219 m
b_1	0.045 m
ε_{11}	6.24 degree
Upper Arm	
P_1P_2	0.35 m
P_1P_{m1}	0.164 m
Mass M_{r1}	1.772 kg (including the elbow actuator)
Inertia I_1	0.0239 kgm^2 (with respect to upper arm gravity centre, through P_{m1})
d_{21}	0.3186 m
d_{22}	0.045 m
a_2	0.3218 m
b_2	0.045 m
ε_{m1}	7.9 degree
ε_{21}	8.04 degree
Forearm	
P_2P_3	0.33 m
P_2P_{m2}	0.103 m
Mass M_{r2}	0.739 kg
Inertia I_2	0.0035 kgm^2 (with respect to forearm gravity centre, through P_{m2})
ε_{22}	6.0 degrees

Table 5.1 The dimensions and specifications of the robot arm (excluding the hand)

5.2 Generating a MiL Testing System with the Robot Arm

When the robot arm stretches to an upright position, which means, the elbow joint is controlled to keep a constant angle (θ_2) of 30˚, and the shoulder is driven around a mean angle (θ_1) of zero, the robot arm can be approximated to an equivalent mass. The arrangement of the robot arm is as shown in Figure 5.4.

With the specified arrangement of the robot arm, a MiL testing system based on the single mass-spring-damper model can be generated. The shoulder force is measured by the load cell, and feedback to the target PC to simulate the motion of spring and damper, and the shoulder actuator is controlled to follow the simulated spring and damper motion.

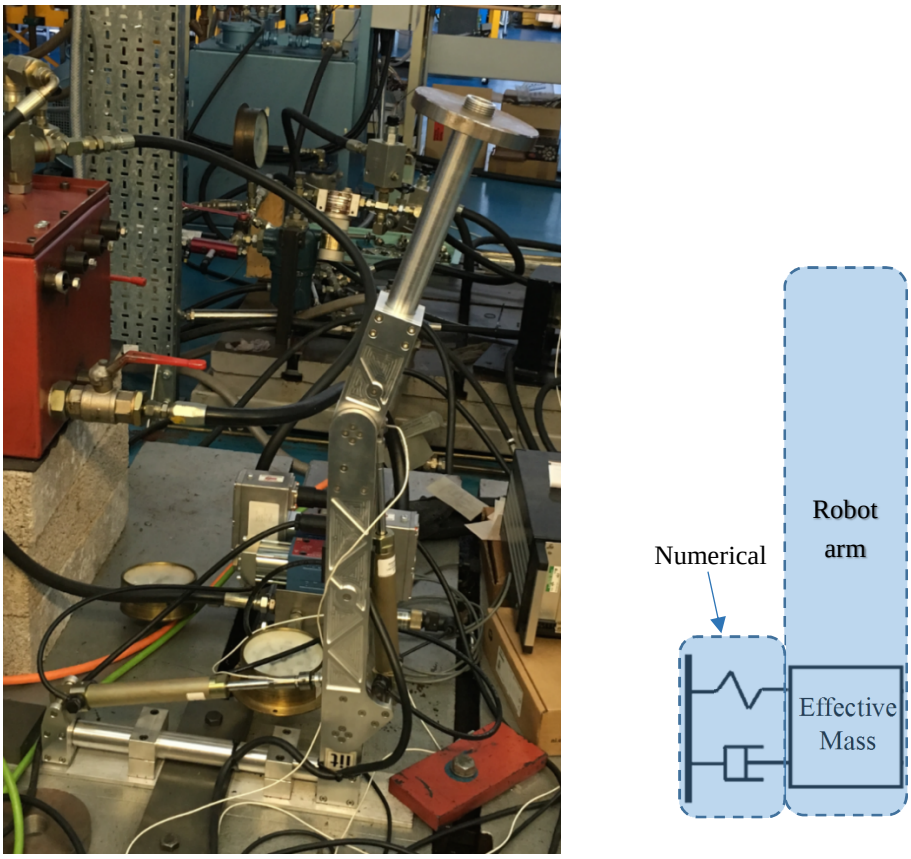

Figure 5.4 The outstretch robot arm

5.2.1 Calculation of the Equivalent Mass

The equivalent mass of the robot arm can be estimated as follows, using the geometry defined in Figure 5.1. The dimensions and the specifications of the robot arm are provided in Table 5.1.

The inertia for the upper arm with respect to point P_1 can be calculated by:

$$I_{11} = I_1 + M_{r1}\overline{P_1P_{m1}}^2 \cos^2\varepsilon_{m1} \tag{5.1}$$

The inertia for the forearm with respect to point P_1 can be calculated by:

$$I_{22} = I_2 + M_{r2}\left(\overline{P_2P_{m2}}\cos\theta_2 + \overline{P_1P_2}\right)^2 \tag{5.2}$$

The inertia for the hand with respect to point P_1 can be calculated by:

$$I_{33} = I_3 + M_{r3}\left(\overline{P_2P_3}\cos\theta_2 + \overline{P_1P_2}\right)^2 \tag{5.3}$$

Substitute with the dimensions and specifications given in Table 5.1, it can be shown that:

$$I_{11} = 0.0707 \text{ kgm}^2,\ I_{22} = 0.1461\,\text{kgm}^2,\ I_{33} = 0.3930\,\text{kgm}^2$$

The overall rotational inertia of the robot arm, with respect to point P_1 can then be calculated:

$$I_t = I_{11} + I_{22} + I_{33} = 0.6098 \text{ kgm}^2 \tag{5.4}$$

The detailed definition of the dimensions of the robot arm around the shoulder actuator area is illustrated in Figure 5.5. When θ_1 is equal to zero, the geometry around the shoulder assembly is plotted in Figure 5.6, where the direction of x is defined to be the direction of extension of the shoulder actuator, and l_1 is the distance from point P_1 to line on the direction of the shoulder actuator extension.

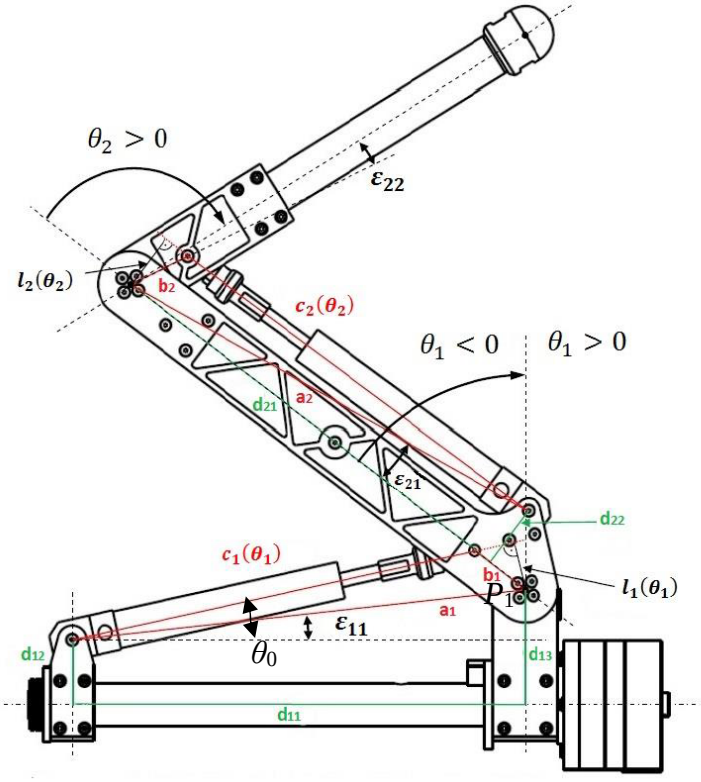

Figure 5.5 The geometry of the robot arm, with additional details of the dimensions around the shoulder actuator area [31]

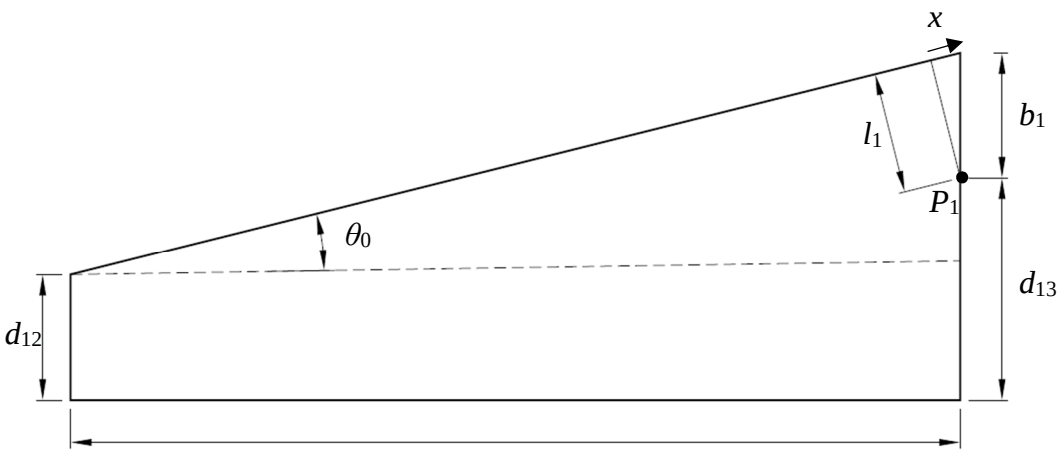

Figure 5.6 The geometry around the shoulder assembly when θ_1 is equal to zero

From Figure 5.5, it can be found that:

$$d_{13} - d_{12} = d_{11} \tan \varepsilon_{11} = 0.0350 \text{ m} \tag{5.5}$$

From Figure 5.6, it can be found that:

$$tan\theta_0 = \frac{d_{13} - d_{12} + b_1}{d_{11}} = 0.25 \tag{5.6}$$

$$\theta_0 = 14° \tag{5.7}$$

$$l_1 = b_1 cos\theta_0 = 0.0437 \text{ m} \tag{5.8}$$

Define p as the force applied to the vertically stretched out robot arm from the shoulder actuator, in the direction of the motion of the actuator:

$$pl_1 = I_t\ddot{\theta}_1 \tag{5.9}$$

When θ_1 is small ($-10^\circ \leq \theta_1 \leq 10^\circ$),

$$\theta_1 \approx \tan\theta_1 = \frac{x}{l_1} \tag{5.10}$$

$$\Rightarrow \ddot{\theta}_1 = \frac{\ddot{x}}{l_1} \tag{5.11}$$

Substitute equation (5.11) into equation (5.9):

$$p = \frac{I_t}{l_1^2}\ddot{x} \tag{5.12}$$

Substitute the calculated values of I_t and l_1 into equation (5.12):

$$p = 310\ddot{x} \tag{5.13}$$

So it can be concluded that the theoretical equivalent mass is 310 kg.

However, in this analysis, because firstly the weight of the electronic circuits attached to the robot arm and the oil inside the actuator is not taken into account, and secondly, due to the measurement error of the component mass, the actual equivalent mass is a little larger than the theoretical value.

The actual equivalent mass (M_{eq}) is measured experimentally as follows.

The shoulder actuator is controlled by the PI controller to follow a sine wave signal oscillating around the mean value of θ_1 is equal to zero, with the frequency of 1Hz. From the amplitude of the force measured by the load cell (F), and the amplitude of the displacement of the shoulder actuator (D), the equivalent mass can be calculated with equation (5.14):

$$M_{eq} = \frac{F}{4\pi^2 D} \tag{5.14}$$

The experimental measurement of the displacement of the shoulder actuator is shown in Figure 5.7, and the measurement of the force (which is low-pass filtered to filter out the high frequency noise) is illustrated in Figure 5.8. It is important to notice that the force is calibrated to be equal to zero when θ_1 is equal to zero, and the phase lag of the measured force in comparison with the displacement input is due to the low-pass filter. More details about the force calibration can be found in section 5.2.3. The actual equivalent mass can then be calculated to be 400 kg.

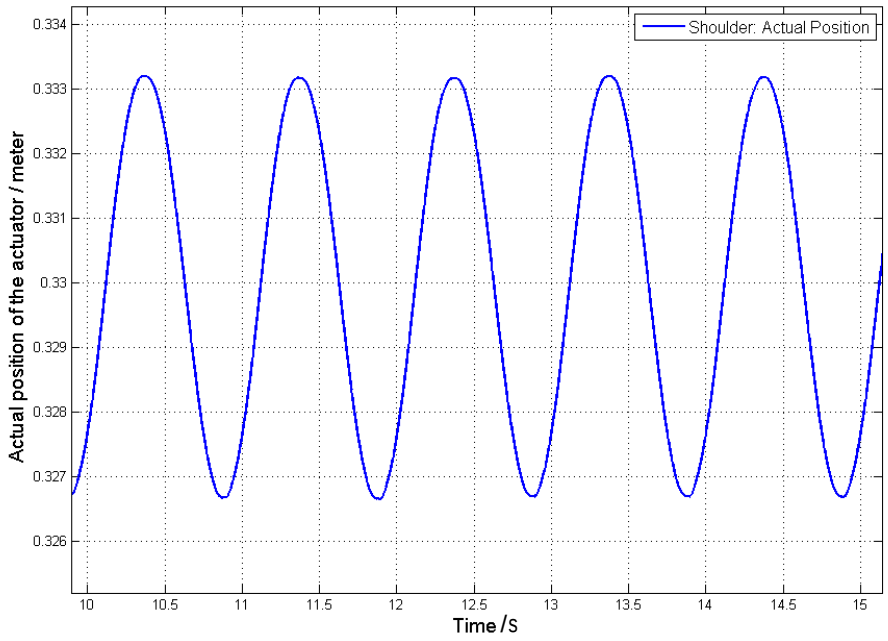

Figure 5.7 The experimental measurement of the displacement of the shoulder actuator

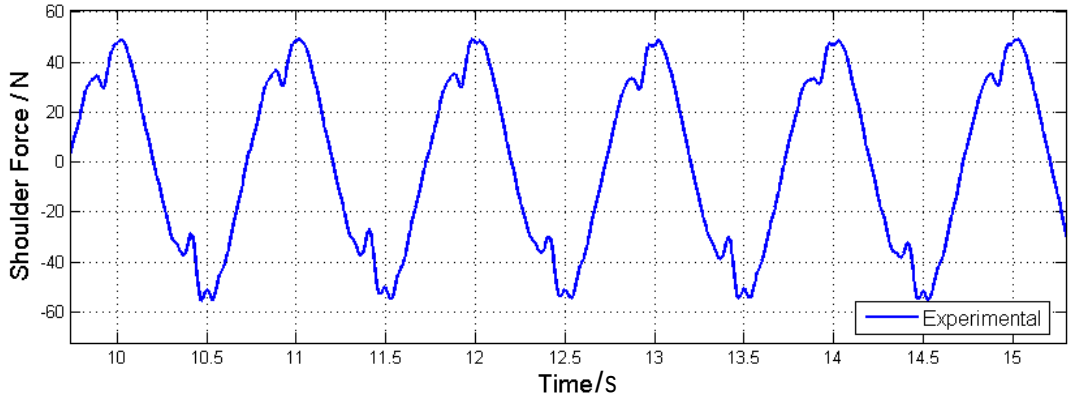

Figure 5.8 The experimental measurement of the force

5.2.2 Frequency Response Measurement

Before the actual MiL test was done, the frequency response of the shoulder actuator was measured, by testing the response of the actuator with a series of single frequency sine wave signals with amplitudes of 5° as the input position demand. The actual actuator position and the demand signal was compared, thus the magnitude and phase characteristics were calculated, shown by the black solid line in Figure 5.9.

A 3rd order transfer function is fitted to the measured frequency response by first estimating the the poles and gradually adjust the transfer function until a good fit is achieved by visual inspection. The fitted transfer function is shown as follows:

$$A(s) = \frac{1}{0.00006079s^3 + 0.005046s^2 + 0.0812s + 1} \tag{5.15}$$

The frequency response of the estimated transfer function is plotted in Figure 5.9 with blue dash line. It can be observed that the magnitude of the estimated transfer function fits to the experimentally measured magnitude rather well, but the estimated phase is not accurate, especially in the frequency range of 1 to 3 Hz. This could mean there are some nonlinear characteristics in the valve-actuator driving system.

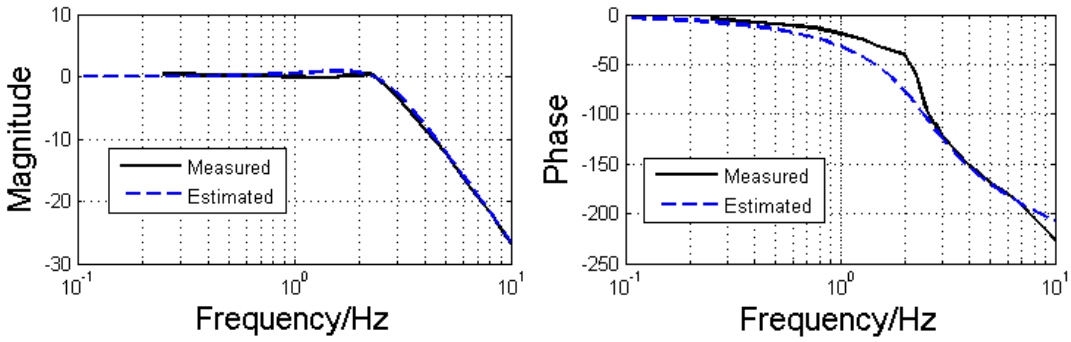

Figure 5.9 Comparison of the measured and estimated frequency response of the shoulder actuator

5.2.3 Force Calibration

For a MiL test as specified in the beginning of this chapter, the force is measured and fed back to the numerical model. Therefore, to make a valid MiL test, it is important to calibrate the force accurately.

In this case, the largest disturbance of the force measurement is the force applied to the load cell because of the weight of the robot arm. For the specified MiL testing, when the robot arm is in the middle point (that is, when θ_1 is equal to zero), the force should be zero, because the displacement of the simulated spring is also zero. However, because the centre of gravity of the outstretched robot arm is not on the line P_1P_2 (which is vertical when θ_1 is equal to zero), gravity will pull the robot arm away from the original position, and therefore apply a force on the load cell attached to the shoulder actuator.

It is necessary to calculate the additional force caused by the offset of the centre of gravity to compensate for it. The force can be calculated as follows, using the parameters given in Table 5.1. Define a coordinate system using point P_1 as the original point (0, 0), and define vertical up direction as the direction of the y axis, and

horizontal right direction as the direction of the x axis. The coordinates of the centre of gravity of the upper arm, the forearm, and the hand can be calculated respectively as:

$$P_{m1}(x_{m1}, y_{m1}) = P_{m1}(0.0225, 0.1624) \tag{5.16}$$

$$P_{m2}(x_{m2}, y_{m2}) = P_{m2}(0.0515, 0.4392) \tag{5.17}$$

$$P_{m3}(x_{m3}, y_{m3}) = P_{m3}(0.1516, 0.6126) \tag{5.18}$$

Therefore the overall centre of gravity of the outstretch robot arm can be calculated (Assume the point of the overall centre of gravity is $P_{mt}(x_{mt}, y_{mt})$):

$$x_{mt} = \frac{M_{r1}x_{m1} + M_{r2}x_{m2} + M_{r3}x_{m3}}{M_{r1} + M_{r2} + M_{r3}} = 0.0663 \tag{5.19}$$

$$y_{mt} = \frac{M_{r1}y_{m1} + M_{r2}y_{m2} + M_{r3}y_{m3}}{M_{r1} + M_{r2} + M_{r3}} = 0.3518 \tag{5.20}$$

The overall mass is:

$$M_t = M_{r1} + M_{r2} + M_{r3} = 3.55kg \tag{5.21}$$

The geometry and the state of loading is plotted in Figure 5.10.

It can be shown that:

$$\left|\overrightarrow{P_1P_{mt}}\right| = 0.358m \tag{5.22}$$

$$\varepsilon_{mt} = 10.68° \tag{5.23}$$

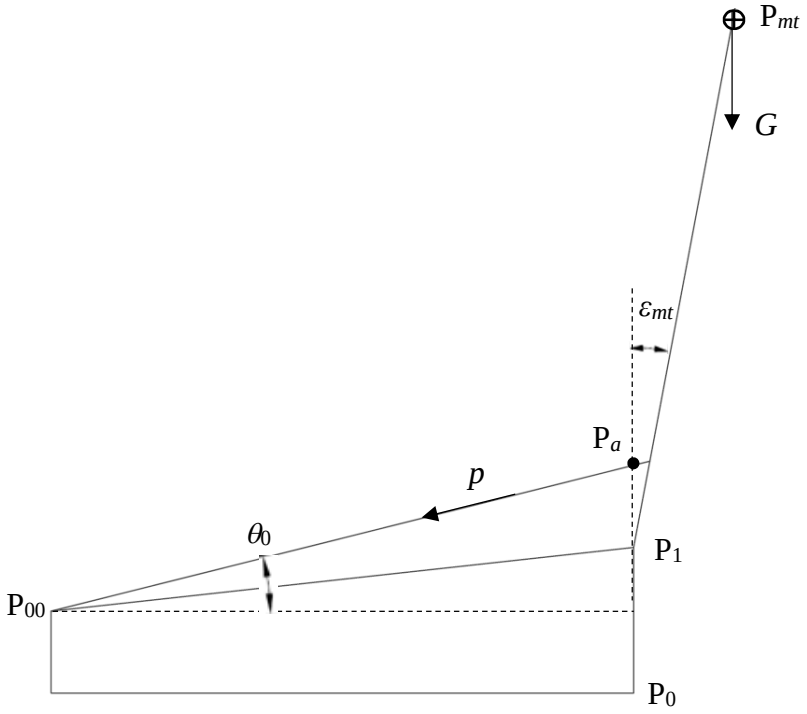

Figure 5.10 The geometry and the state of loading when θ_1 is equal to zero

Redefine point P_{00} as the original point (0, 0), and keep the directions of the x axis and y axis as they are. Assume that the robot arm rotates in θ_1 degrees from the vertical position.

It can be shown that:

$$\overrightarrow{P_{00}P_1} = (0.32, 0.035) \tag{5.24}$$

$$\overrightarrow{P_1P_a} = (0.045\sin\theta_1 \quad , \quad 0.045\cos\theta_1) \tag{5.25}$$

$$\overrightarrow{P_{00}P_a} = (0.32 + 0.045\sin\theta_1 \quad , \quad 0.035 + 0.045\cos\theta_1) \tag{5.26}$$

$$\theta_0 = \tan^{-1}\left(\frac{0.035 + 0.045\cos\theta_1}{0.32 + 0.045\sin\theta_1}\right) \tag{5.27}$$

The equation for line $P_{00}P_a$ can be written as:

$$(0.035 + 0.045\cos\theta_1)x - (0.32 + 0.045\sin\theta_1)y = 0 \tag{5.28}$$

The coordinate for point P_1 is P_1 (0.32, 0.035).

The distance between point P_1 and line $P_{00}P_a$ can be calculated:

$$d = \frac{|0.32A - 0.035B|}{\sqrt{A^2 + B^2}} \tag{5.29}$$

where $A = 0.035 + 0.045\cos\theta_1$, and $B = 0.32 + 0.045\sin\theta_1$.

The Force p can be calculated as follows (g is the gravitational acceleration):

$$p = \frac{M_t g\left|\overrightarrow{P_1P_{mt}}\right|\sin(10.68° + \delta\theta)}{d} \tag{5.30}$$

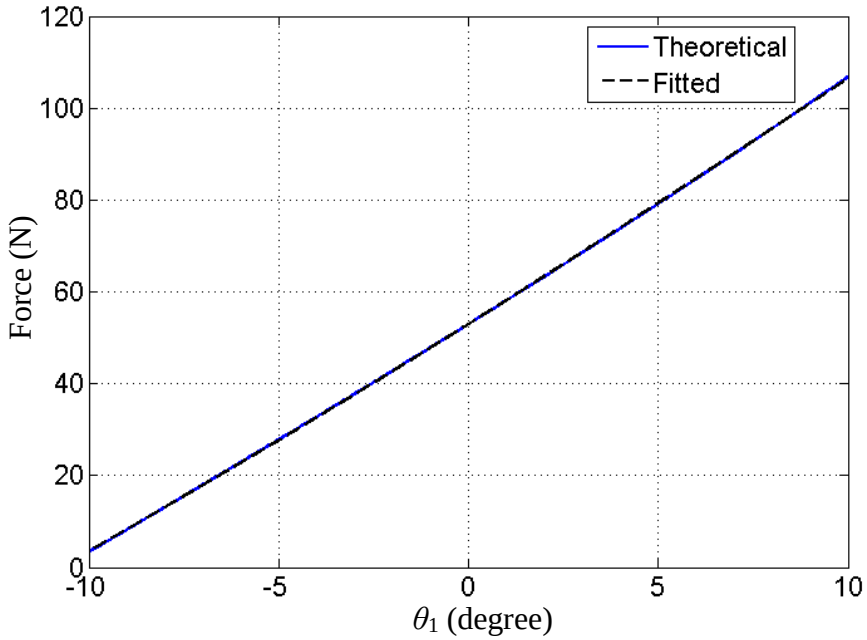

Figure 5.11 The unbalance force with the change of θ_1

The force applied to the load cell due to the offset of the centre of gravity is plotted against the rotation of the robot arm from the vertical position θ_1, as shown in Figure 5.11. The curve is fitted to a second order polynomial using Matlab's polyfit function, and the motivation for the fitting process is the fitted second order polynomial being less computational demanding than the original function. The fitted curve is shown in black dash line in Figure 5.11. It can be seen that the fitted curve is very close to the theoretical curve. Therefore in the experiment, the fitted second order polynomial will be used for the calibration, instead of the complicated theoretical one.

The effectiveness of the force calibration is checked with experiment. In the experiment, the motion of the actuator is controlled by a PI controller to follow the input signal, without any force feedback. A ramp signal is given to the actuator to rotate the robot arm slowly from -10° to +10°. The demand position and the actual position is plotted in Figure 5.12.

The calibrated force (which is low-pass filtered to filter out the high frequency noise) is illustrated in Figure 5.13. It can be observed that for all robot arm positions from -10° to +10°, the average value of the calibrated force remains at about zero, which has verified the force calibration is accurate.

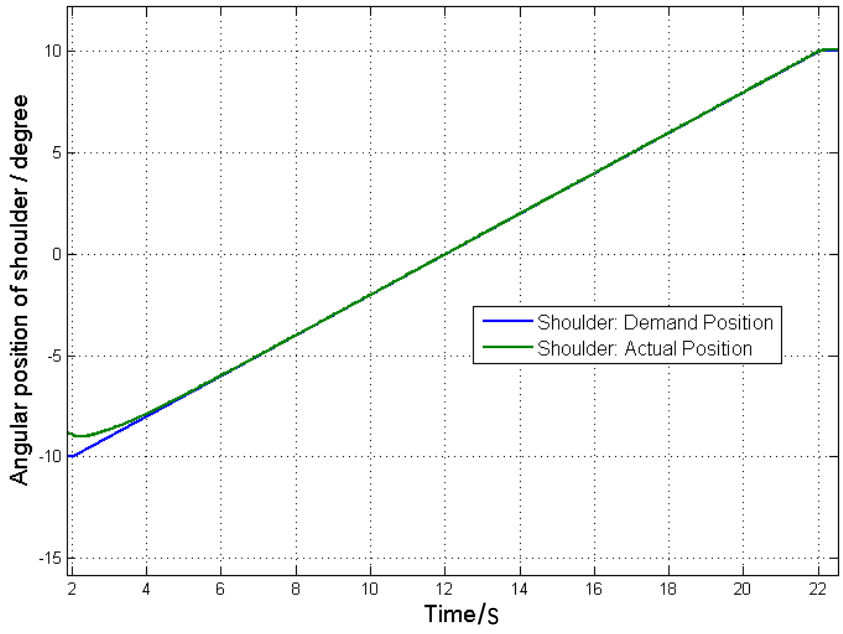

Figure 5.12 The demand position and the actual position with the ramp input

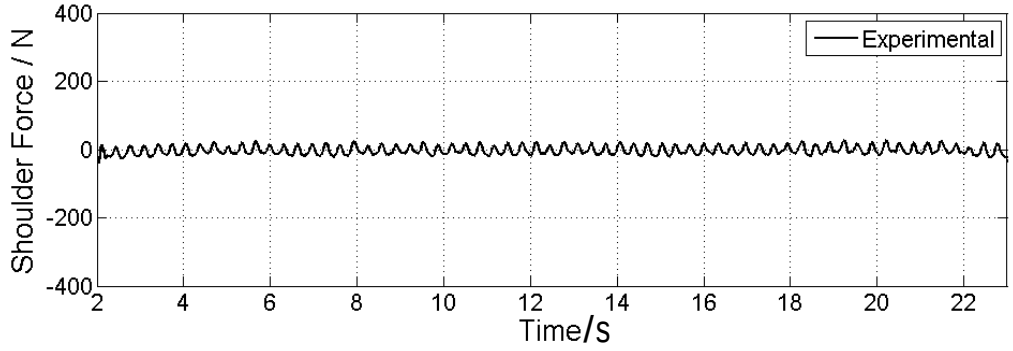

Figure 5.13 The experimentally measured force

5.3 Results with no Compensator

MiL testing can be implemented using the derived equations from section 3.1.1. The simulated damping is 4000 Ns/m, and the simulated stiffness is 16000 N/m, giving an expected natural frequency of 1.143Hz and damping ratio of 0.225. Notice that these are the same parameters and the same system as analysed in section 4.4.1. The input position z_0 is a chirp signal, the frequency of which increases from 0.5Hz to 2Hz.

Firstly, the MiL test was run without any compensator. The experimental result is shown in Figure 5.14, compared with the simulation result of the displacement of a 400kg mass vibrating on the spring and damper with the same parameters as in the MiL test. The simulation result with the actuator dynamics included is also shown, using the estimated transfer function shown in equation (5.15).

It can be seen from Figure 5.14 that, the experimental result is very close to the simulated result with actuator dynamics considered, which means that the estimated actuator transfer function shown in equation (5.15) is adequate. A big error is observed between the experimental result and the simulated result with no actuator dynamics considered, especially in the frequency range of 1Hz to 2Hz. The root mean square value of the error between the actual position and the simulated ideal position is 1.2136. It can be concluded from this example that the actuator lag can significantly affect the accuracy of the test.

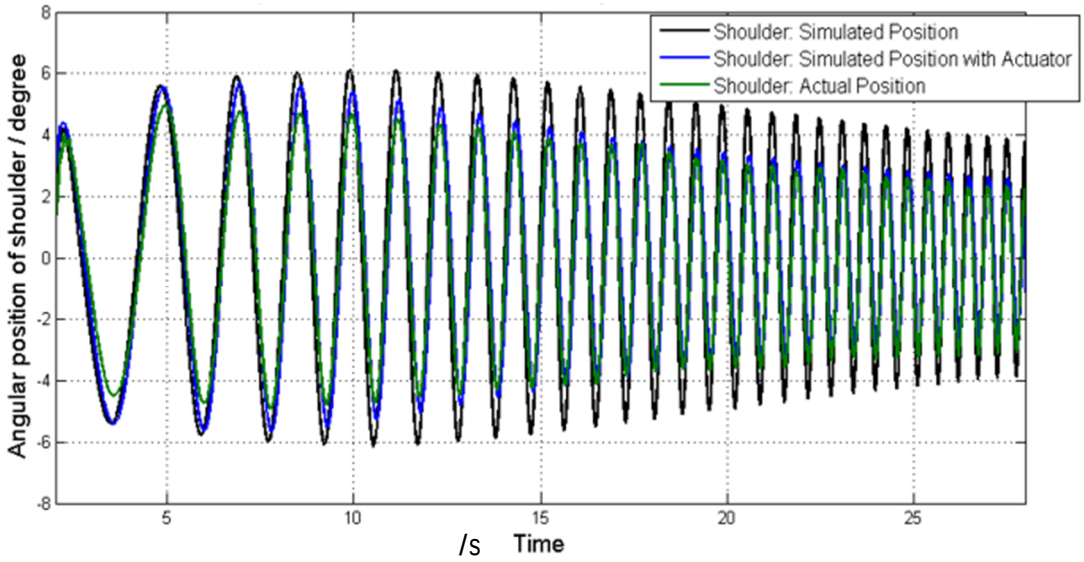

Figure 5.14 Experimental result without compensator

5.4 Results with Inverse Model Compensator

A MiL test was done using the same parameters, while an inverse model compensator is added to the system, so the demand position is filtered by the compensator, before the demand goes to the actuator. The transfer function of the compensator is (obtained by simply inverting the modelled actuator dynamics):

$$C_1(s) = \frac{1}{A(s)} = 0.00006079s^3 + 0.005046s^2 + 0.0812s + 1 \tag{5.31}$$

To make this realizable, the inverse model compensator was multiplied with 3 additional high frequency poles (all 3 poles are with break points of 1000 rad/s). These do not make an observable difference in the concerned frequency range. The experimental result using the inverse model compensator is shown in Figure 5.15.

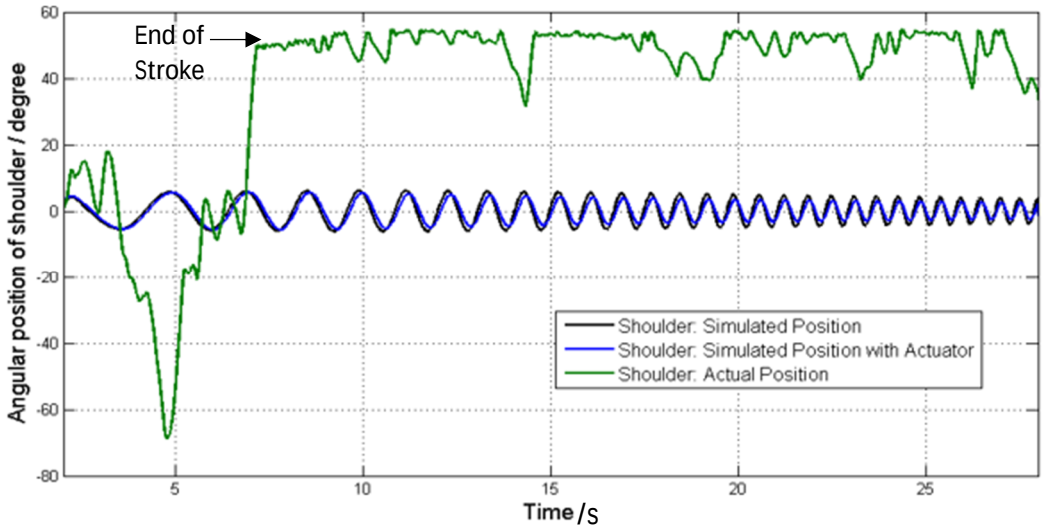

Figure 5.15 Experimental result with inverse model compensator

It can be observed that with the inverse model compensator added to the system, stable position control is no longer achieved. The reason for the poor result is the normalised driving signal of the control valve is saturated at ±1. The driving signal during the experiment swings between the saturation levels all the time in very high frequency. This is because the inverse model enormously amplifies the high frequency noise introduced to the closed-loop system by the load cell. Because of the signal saturation, motion is altered unpredictably.

5.5 Results with Low-Pass Filtered Inverse Model Compensator

Using the same parameters, a MiL test was implemented as it is described in section 5.3, with a low-pass filtered inverse model compensator added to the system. The transfer function of the compensator is (This transfer function is calculated with the algorithms provided in Chapter 4, the details of the MATLAB codes are given in Appendix 4.1.1):

$$C_2(s) = \frac{0.00006079s^3 + 0.005046s^2 + 0.0812s + 1}{0.00002783s^3 + 0.001837s^2 + 0.06061s + 1} \tag{5.32}$$

The frequency response of the low-pass filtered inverse model compensator (black solid line) is compared with the original inverse model compensator (blue dash line) in Figure 5.17.

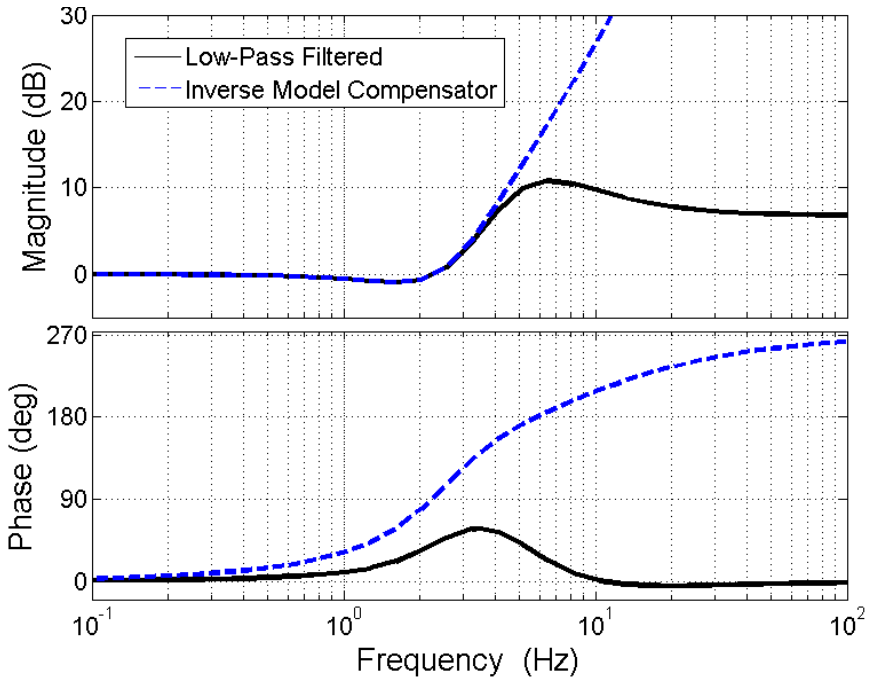

Figure 5.17 The frequency response of the low-pass filtered inverse model compensator and the original inverse model compensator

The experimental result using the filtered inverse model compensator is shown in Figure 5.18, and the normalised driving signal of the control valve is plotted in Figure 5.19. It can be concluded from Figure 5.19 that, because of the attenuation of the high frequency component caused by the additional low-pass filter, the signal is no longer saturating. The root mean square value of the error between the actual position and the simulated ideal position is 0.8849. From Figure 5.18, it can be observed that, compared with the testing result using no compensator at all, the compensator has clearly compensated for the inaccuracy caused by the lag of the actuator, especially in the frequency range of 1Hz to 2Hz (From 15s onwards). However, there's still a big error between the simulated position without any actuator dynamics and the actual position.

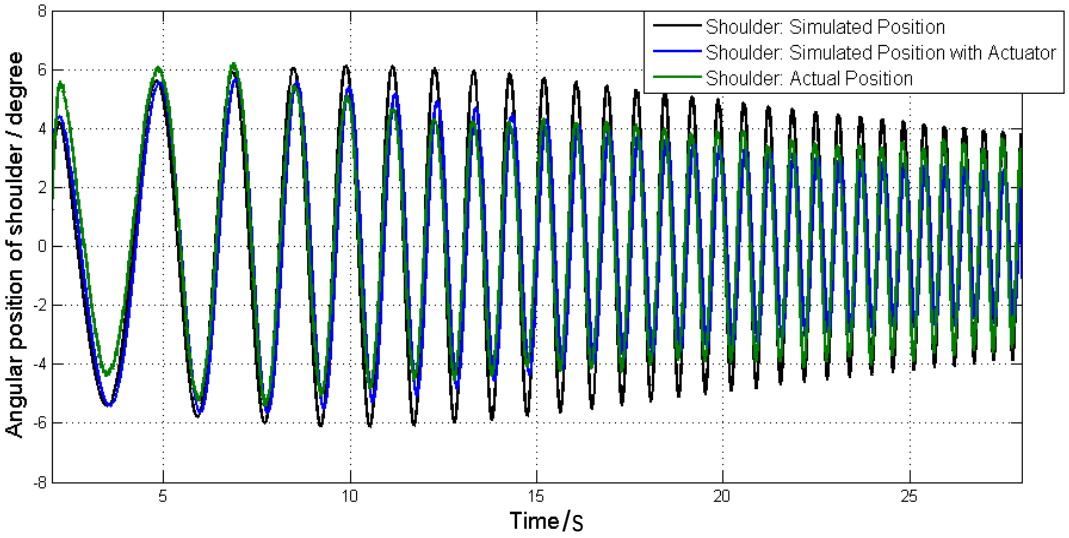

Figure 5.18 Experimental result with low-pass filtered inverse model compensator

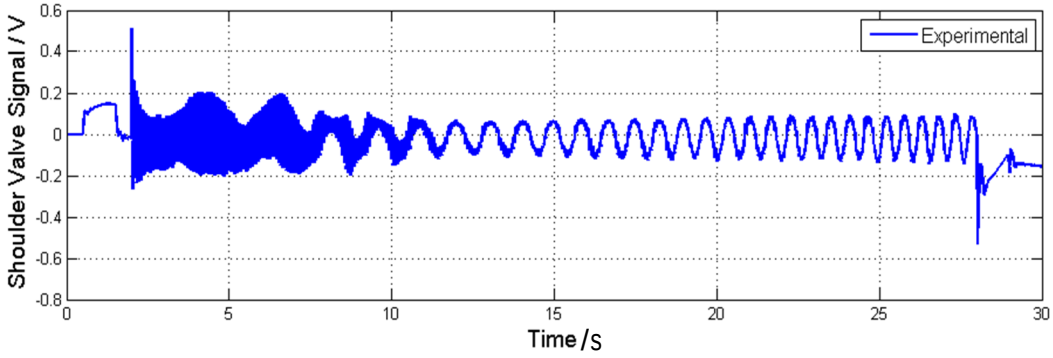

Figure 5.19 The driving signal, with low-pass filtered inverse model compensator

5.6 Results with H_∞ Optimized Compensator

Using the same parameters, a MiL test was implemented as described in section 5.3 and, with the H_∞ optimized compensator added to the system, designed as described in section 4.4.1. The transfer function of the compensator is:

$$C_3(s) = \frac{80.66s^4 + 1.219\times10^4 s^3 + 3.842\times10^5 s^2 + 8.988\times10^6 s + 10^8}{s^4 + 867.7s^3 + 4.43\times10^5 s^2 + 4.145\times10^6 s + 10^8} \quad (5.33)$$

The frequency response of the H_∞ optimized compensator is shown in Figure 5.20 (black solid line), compared with the frequency response of equation 5.31 (blue dash line).

The experimental result using the inverse model compensator is shown in Figure 5.21. It is observable that, the H_∞ optimized compensator accurately compensated for the error caused by the lag of the actuator, showing a close match between the simulated result and the experimentally measured result. The root mean square value of the error between the actual position and the simulated ideal position is 0.7115. It can be concluded that, in this specific case, the the H_∞ optimized compensator is more accurate than the low-pass filtered inverse model compensator.

The normalised driving signal of the control valve is illustrated in Figure 5.22. It can be seen that, although the high frequency component is amplified significantly, the signal is not saturating.

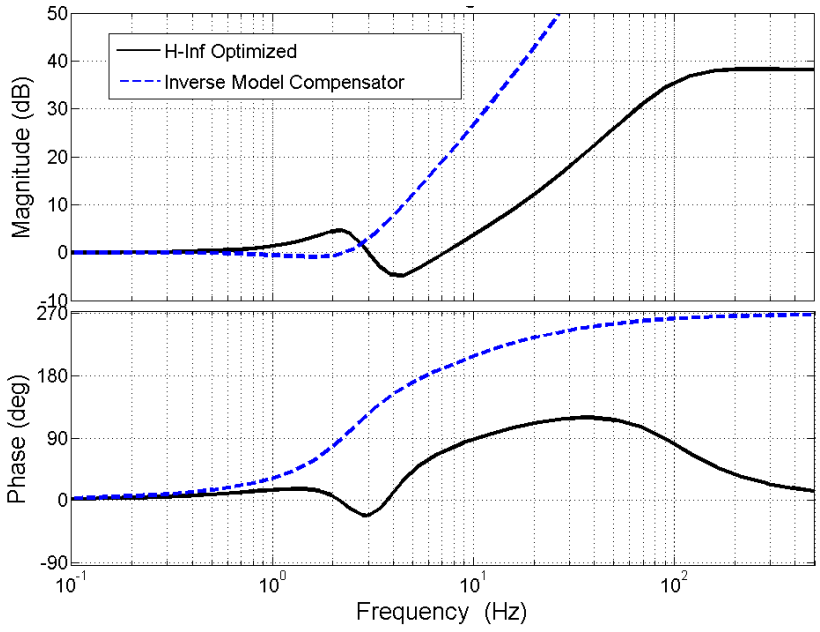

Figure 5.20 The frequency response of the H_∞ optimized compensator

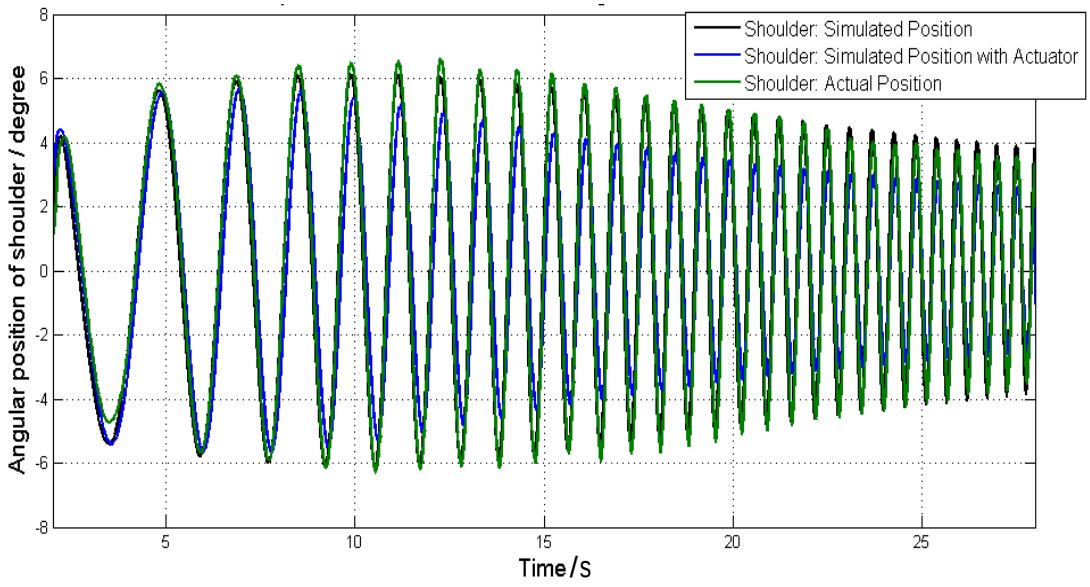

Figure 5.21 Experimental result with H_∞ optimized compensator

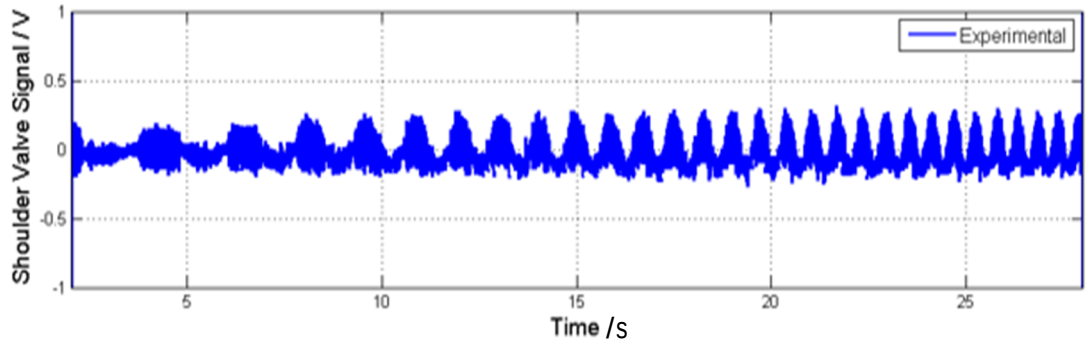

Figure 5.22 The driving signal, with low-pass filtered inverse model compensator

5.7 Concluding Remarks

In this chapter, MiL testing is experimentally investigated using the specified robot arm. It is shown that, for a non-compensated MiL test, the test results will be inaccurate due to the lag caused by actuator dynamics. Theoretically the inverse model compensator can perfectly compensate for any linearized actuator characteristics,

however, in reality, the inverse model compensator is unacceptable, because the inherent high order differentiation in the inverse model controller will greatly amplify the high frequency component in the compensated signal, thus the problem of saturation is very likely to occur in the compensated signal. The signal saturation problem can be solved by multiplying the inverse model compensator with a low-pass filter, however the additional phase lag introduced by the low-pass filter will affect the accuracy.

The effectiveness of the H_∞ optimized compensator calculated with the algorithm proposed in Chapter 4 is also studied experimentally using the robot arm system. The H_∞ optimized compensator has shown its clear advantage over the low-pass filtered inverse model compensator in terms of accuracy, and the H_∞ optimized compensator also succeeded in stabilizing the closed loop system and avoiding the signal saturation problem in the compensated signal.

It is also important to notice that, the proposed H_∞ optimization algorithm is not designed only for this example, it is a generalised optimization method for any MiL testing system.

Chapter 6

6 Performance Envelope and Actuator Selection

In this chapter, the concept of performance envelope will be introduced to indicate the maximum amplitude of sinusoidal motion of an actuator driven by a modulating valve in different frequency ranges, given the physical limitations of the system (i.e. saturation). In this chapter, the MiL test generated with the robotic arm as explained in Chapter 5 is used as an example to show the application of performance envelope. The performance envelope used in this chapter is a plot of velocity amplitude against frequency. The performance envelope is then utilized as guidance to judge if an actuator is suitable for a specific MiL test. The approach can also provide guidance for choosing a suitable actuator for any MiL test. It is shown that the H_∞ optimized compensator affects the relationship between the required performance envelope and the MiL test amplitude.

This chapter is divided into 3 sections:

6.1 The Performance Envelope of an Actuator

6.2 Performance Envelope and MiL Testing

6.3 Control Signal Saturation

6.4 Concluding Remarks

6.1 The Performance Envelope of an Actuator

The performance envelope is defined as the maximum sinusoidal motion amplitude, either position, velocity, or acceleration, for an actuator driven by a modulating valve in a range of frequencies. In this chapter, the performance envelope will be presented as the maximum velocity against frequency.

An example of a simple performance envelope for an actuator driven by a modulating valve is given in Figure 6.1.

The minimum of all the three lines is the speed an actuator can achieve at any particular frequency. The three lines represent three different limits affecting the maximum speed of the actuator. The blue solid line is the stroke limit, which is the speed limited by the maximum stroke of an actuator. The green solid line is the flow limit, meaning the speed limited by the maximum flow rate a valve/actuator system can provide. The red solid line shows the force limit, which is the speed limited by the maximum pressure a valve/actuator system can achieve.

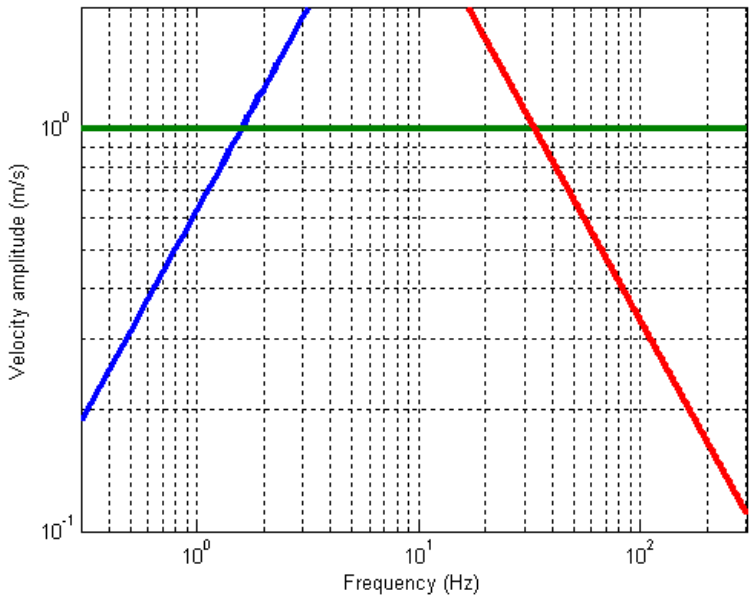

Figure 6.1 An example performance envelope

The equations to calculate the stroke limit, the flow limit, and the force limit are given below.

For the stroke limit:

$$V \leq \frac{S\omega}{2} \tag{6.1}$$

where S is the full stroke of the actuator, ω is the frequency of the motion, and V is the achievable velocity amplitude.

For the flow limit:

$$V \leq \frac{Q}{A} \tag{6.2}$$

where Q is the maximum flow rate of the valve/actuator system, and A is the driving area of the actuator.

For the force limit:

$$V \leq \frac{PA}{M_{eq}\omega} \tag{6.3}$$

where P is the maximum pressure the valve/actuator system can achieve, and M_{eq} is the equivalent mass of the load.

It is quite easy to calculate the stroke limit according to the maximum stroke of the actuator, but for the calculation of the flow limit and the force limit, it is important to calculate the flow rate and the pressure accurately, considering the pressure drop in the valve and in the hydraulic cylinder.

The calculation of the flow limit is shown as follows, for extension and retraction respectively.

`

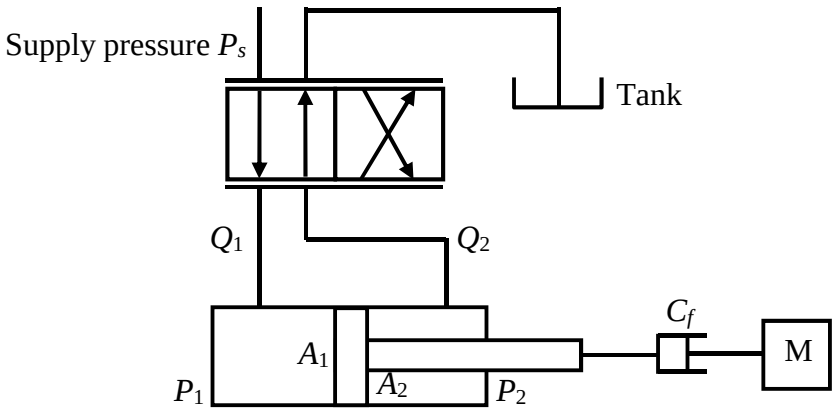

Figure 6.2 The valve/actuator system in extension

Considering extension first, Figure 6.2 shows the valve/actuator system while extending. In this research, the friction inside the hydraulic cylinder as well as fluid friction in pipes is approximated as viscous friction force only, which is proportional to the velocity. In Figure 6.2, C_f is the factor of the viscous friction force, and the friction force can be calculated as follows:

$$F_f = C_f v \tag{6.4}$$

The equations for the valve/actuator system in extension are:

$$Q_1 = \frac{Q_r}{\sqrt{P_r}}\sqrt{P_s - P_1} \tag{6.5}$$

$$Q_2 = \frac{Q_r}{\sqrt{P_r}}\sqrt{P_2} \tag{6.6}$$

$$\frac{Q_1}{A_1} = \frac{Q_2}{A_2} = v \tag{6.7}$$

$$P_1 A_1 - P_2 A_2 = C_f v \tag{6.8}$$

In equations (6.5) and (6.6), Q_r is the rated flow rate of the hydraulic valve, and P_r is the pressure at which that flow is measured. Both of the parameters are provided by the manufacturer. For determining the flow limit, we are concerned with the maximum velocity condition which occurs with an acceleration of zero, so no inertial term has been included in equation (6.8).

Substitute equations (6.5) and (6.6) in equation (6.7):

$$\frac{Q_r}{\sqrt{P_r}}\frac{\sqrt{P_s - P_1}}{A_1} = \frac{Q_r}{\sqrt{P_r}}\frac{\sqrt{P_2}}{A_2} = v \tag{6.9}$$

It can be shown that:

$$\frac{P_s - P_1}{A_1^2} = \frac{P_2}{A_2^2} \tag{6.10}$$

Define R as the ratio of the piston area to the annulus area:

$$R = \frac{A_1}{A_2} \tag{6.11}$$

Substitute equation (6.11) into equation (6.10):

$$P_s - P_1 = R^2 P_2 \tag{6.12}$$

Substitute equations (6.9) and (6.12) into equation (6.8):

$$A_1\left(P_s - R^2 P_2\right) - A_2 P_2 = \frac{C_f Q_r}{\sqrt{P_r}}\frac{\sqrt{P_2}}{A_2} \tag{6.13}$$

It can be shown that:

$$\left(A_1 R^2 + A_2\right)P_2 + \frac{C_f Q_r}{\sqrt{P_r}}\frac{\sqrt{P_2}}{A_2} - A_1 P_s = 0 \tag{6.14}$$

Solve equation (6.14) to find P_2, then equations (6.6) and (6.7) can be used to calculate Q_1. In extension, Q_1 is used to calculate the flow limit, and the maximum pressure achievable P_s is used to calculate the force limit.

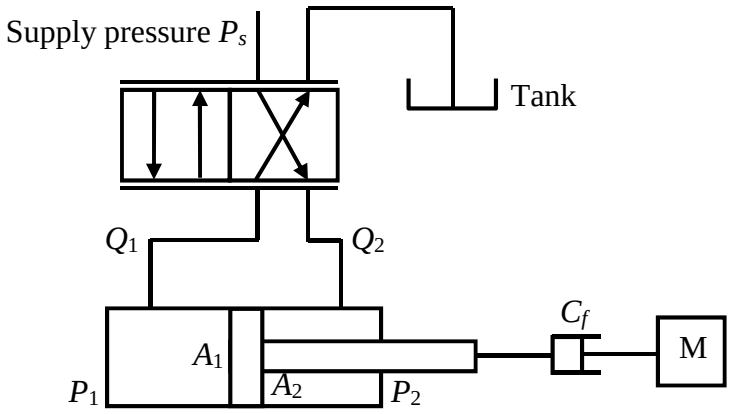

Figure 6.3 The valve/actuator system in retraction

Now consider retraction, as shown in Figure 6.3. The equations for the valve/actuator system in retraction are:

$$Q_1 = \frac{Q_r}{\sqrt{P_r}}\sqrt{P_1} \tag{6.15}$$

$$Q_2 = \frac{Q_r}{\sqrt{P_r}}\sqrt{P_s - P_2} \tag{6.16}$$

$$\frac{Q_1}{A_1} = \frac{Q_2}{A_2} = v \tag{6.17}$$

$$P_2 A_2 - P_1 A_1 = C_f v \tag{6.18}$$

Similar to the derivation of equation (6.14), it can be shown that:

$$\left(A_1 + \frac{A_2}{R^2}\right)P_1 + \frac{C_f Q_r}{\sqrt{P_r}}\frac{\sqrt{P_1}}{A_1} - A_2 P_s = 0 \tag{6.19}$$

Solve equation (6.19) to find P_1, then Q_2 can be calculated with equations (6.15) and (6.16). In retraction, Q_2 is used to calculate the flow limit, and the maximum pressure achievable P_s is used to calculate the force limit.

The parameter values for the valve/actuator system for the shoulder joint of the robot arm are provided in Table 6.1.

A_1	2.01 cm^2
A_2	1.23 cm^2
P_s	38 bar
C_f (in extension)	2800 N/(m/s)
C_f (in retraction)	2400 N/(m/s)
Q_r	0.005 m^3/min
P_r	35 bar
M_{eq}	400 kg

Table 6.1 The parameters for the real valve/actuator system

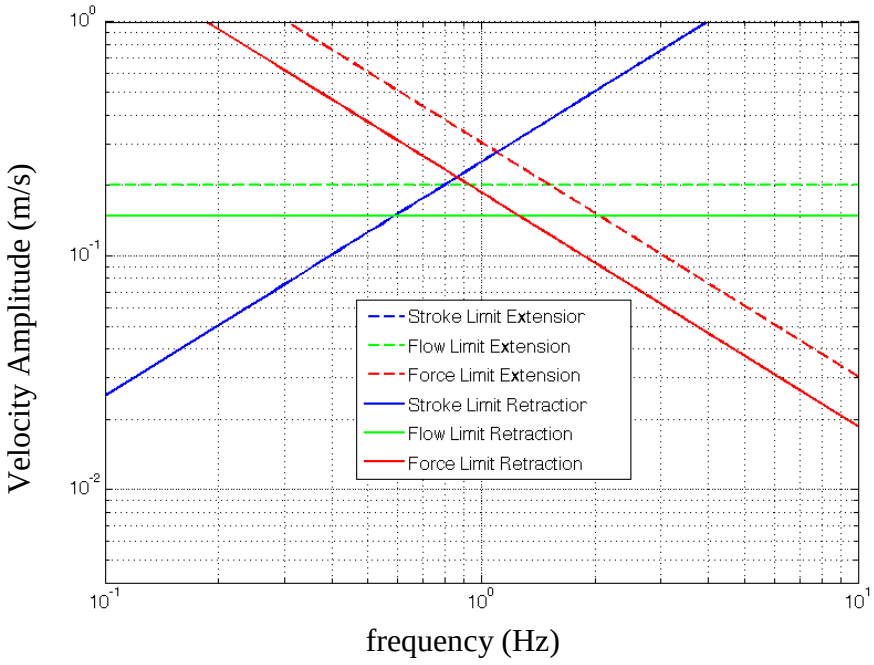

Figure 6.4 The performance envelope when the actuator is extending

The performance envelope when the actuator is extending is plotted in Figure 6.4 in dash lines, and the performance envelope when the actuator is retracting is also shown in Figure 6.4, in solid lines. Comparing the performance envelope in extension and that in retraction, it can be found that in this example, when the actuator is retracting, the speed limit is lower than when it is extending. So in this case, the performance envelope in retraction will be used as the speed limit.

6.2 Performance Envelope and MiL Testing

As stated in section 6.1, the performance envelope defines the maximum sinusoidal speed of an actuator driven by a modulating valve in different frequency ranges. If the maximum speed requirements for the actuator in a specific MiL test is drawn and compared to the performance envelope of the actuator-valve system in the same graph, the conclusion can be drawn whether the actuator-valve system is suitable for the MiL test.

To study the saturation of the valve-actuator system, the block diagram of the realistic MiL testing system as described in Chapter 5 is illustrated in Figure 6.5, where C is the compensator model, A is the actuator model, P is the physical subsystem, and S_2 is the numerical subsystem

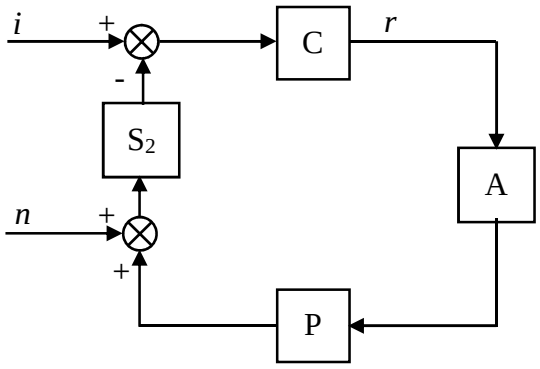

Figure 6.5 The block diagram of the realistic MiL testing system

The transfer function from the input signal *i* to the demand position *r* can be derived.

$$R(s)=\frac{r}{i}=\frac{C(s)}{1+C(s)A(s)P(s)S_2(s)} \tag{6.20}$$

The amplitude of the transfer function (6.20) $|R(j\omega)|$ indicates the amplification of signal from the input *i* to demand position *r*. Thus the amplitude of the transfer function $|R(j\omega)|$ multiplied by the input maximum velocity $|i(j\omega)|\omega$ will be the maximum speed requirement for the valve-actuator system.

The performance envelope and the maximum speed requirements with the same parameters as provided in Table 6.1 and section 5.3 are plotted in Figure 6.6, using no compensator ($C(s)=1$). In Figure 6.6, the solid lines form the performance envelope, the black dash line shows the input maximum velocity $|i(j\omega)|\omega$ (the input position amplitude is 3.8mm), and the blue dash line shows the input maximum velocity multiplied by the amplitude of the transfer function, $|i(j\omega)|\omega|R(j\omega)|$. As stated in section 6.1, only the performance envelope in retraction is used.

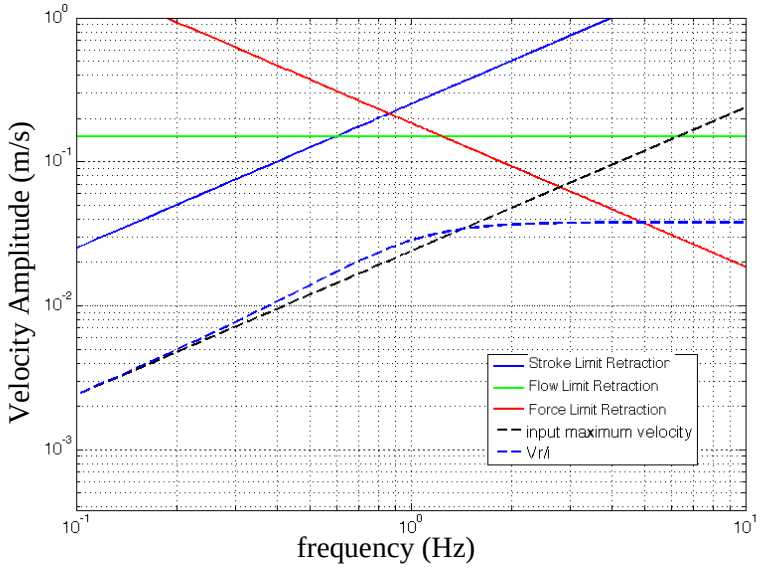

Figure 6.6 The performance envelope and maximum speed requirement

As illustrated in Figure 6.6, the maximum speed requirement crosses the performance envelope at about 4.8Hz. Thus for this example, with the input amplitude of 3.8 mm, the MiL system is able to test up to 4.8Hz. However, it is important to point out that, since the actuator dynamic is not compensated, the testing result is inaccurate in this case.

The performance envelope and the maximum speed requirement are plotted in Figure 6.7, for the MiL system when the inverse model compensator is applied.

As plotted in Figure 6.7, the maximum speed requirement crosses the performance envelope at about 3.2Hz. Thus for this example, with the input maximum velocity $|i(j\omega)|\omega$, the MiL system is able to test up to 3.2Hz. Nevertheless, as already proved in the previous experiment, the inverse model compensator will cause signal saturation in the driving signal of the direct control valve and hence make the testing result very inaccurate. The saturation of the signal will be analysed in the next section.

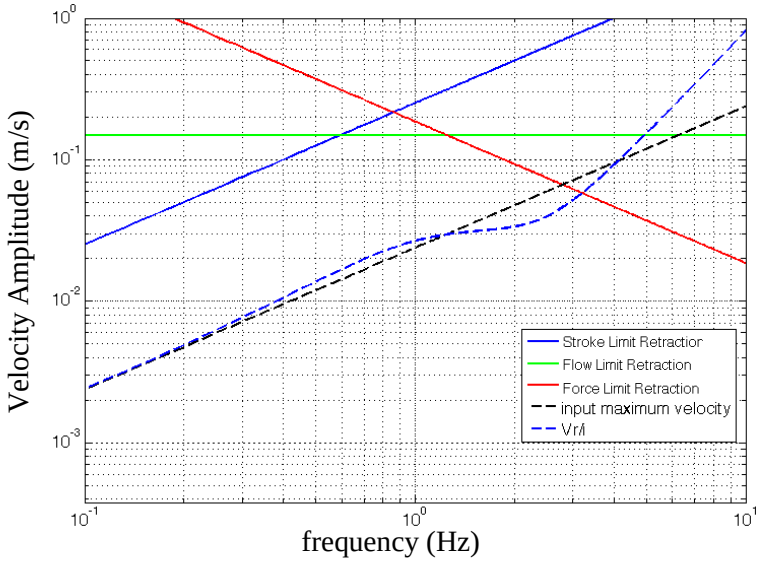

Figure 6.7 The performance envelope and maximum speed requirement, with inverse model compensator

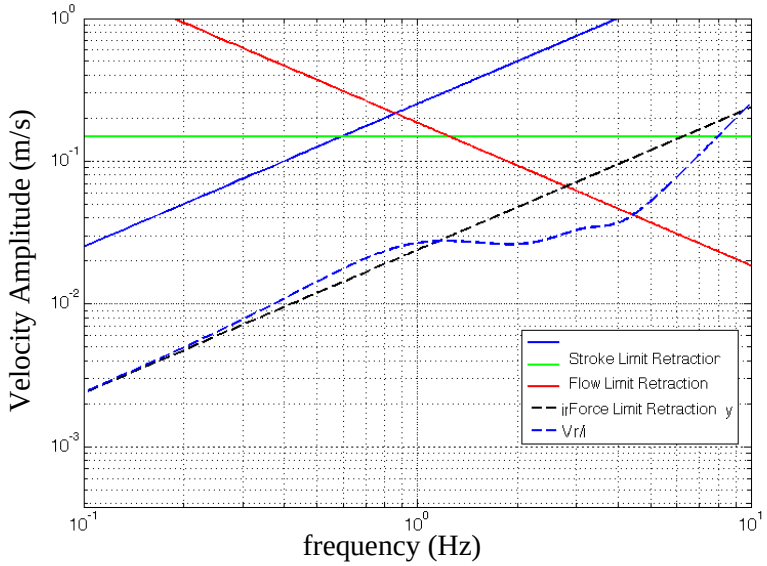

Figure 6.8 The performance envelope and maximum speed requirement, with H_∞ optimized compensator

The performance envelope and the maximum speed requirement are plotted in Figure 6.8, for the MiL system when the H_∞ optimized compensator is applied. As presented in Figure 6.8, the maximum speed requirement crosses the performance envelope at about 4.4Hz. Thus for this example, with the input amplitude $\left|i(j\omega)\right|\omega$, the MiL system is able to test up to 4.4Hz, which is very close to the uncompensated limit, and of course, the H_∞ compensated system will give a much more accurate testing result.

In conclusion, by comparing the performance envelope and the maximum speed requirement, whether the valve-actuator system is suitable for the specific MiL test can be judged. If the maximum speed requirement line fails to fall under the performance envelope in the desired frequency range, a faster actuator is required.

6.3 Control Signal Saturation

To study the saturation of the control signal in the valve-actuator system, the block diagram of the control structure of the realistic MiL testing system as described in Chapter 5 is illustrated in Figure 6.9.

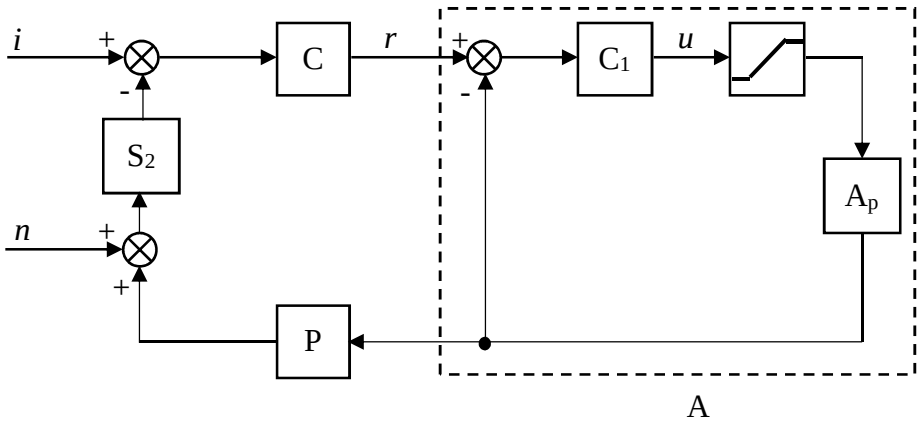

Figure 6.9 The control structure of the realistic MiL testing system

The necessity of doing an analysis as described in this section is that, although in Section 6.2, the performance envelope analysis has already given a limit to the speed of the actuator, however, it is merely a physical limit, and it fails to take the signal amplification in the controller into account. Because of the compensator and the PID controller as shown in Figure 6.9, the actual signal is much larger than the position demand estimated using the performance envelope analysis, and therefore may cause saturation in the control signal.

In Figure 6.9, A is the overall model of the valve-actuator system, and the more detailed structure is also shown, considering the PID controller used in the system. Inside the model, C_1 is the model of the PID controller, and A_p represents the actual dynamics of the valve-actuator combination. With the measured dynamic characteric A and the known PI controller model C_1, the actual dynamics of the valve-actuator combination A_1 can be calculated. When control signal *u* does not saturate, it can be shown that:

$$A(s) = \frac{C_1(s)A_p(s)}{1 + C_1(s)A_p(s)} \tag{6.21}$$

$$A_p(s) = \frac{A(s)}{(1 - A(s))C_1(s)} \tag{6.22}$$

The transfer function from the input signal *i* to the signal *u* can then be derived.

$$U_i(s) = \frac{u}{i} = \frac{C(s)A(s)}{A_p(s)(1 + C(s)A(s)P(s)S_2(s))} = \frac{C(s)C_1(s)(1 - A(s))}{1 + C(s)A(s)P(s)S_2(s)} \tag{6.23}$$

It is concluded from Chapter 5 that the measurement noise introduced in the feedback path may be greatly amplified in the compensated signal and thus leads to saturation, so it is also necessary to check the transfer function from the measurement noise *n* to the control signal *u*. It can be shown that:

$$U_n(s) = \frac{u}{n} = \frac{C(s)S_2(s)A(s)}{A_p(s)(1 + C(s)A(s)P(s)S_2(s))} = \frac{C(s)C_1(s)S_2(s)(1 - A(s))}{1 + C(s)A(s)P(s)S_2(s)} \tag{6.24}$$

Assume that the saturation level for the control signal *u* is λ, the amplitude of the input position demand is $i(j\omega)$, and the amplitude of the measurement noise is $n(j\omega)$. The criterion for the signal not going saturation at point *u* is:

$$\|i(j\omega)U_i(j\omega)\|_\infty + \|n(j\omega)U_n(j\omega)\|_\infty \le \lambda \tag{6.25}$$

Because $\|n(j\omega)U_n(j\omega)\|_\infty \le \|n(j\omega)\|_\infty \|U_n(j\omega)\|_\infty$ assume the following criterion is satisfied:

$$\|i(j\omega)U_i(j\omega)\|_\infty + \|n(j\omega)\|_\infty \|U_n(j\omega)\|_\infty \le \lambda \tag{6.26}$$

If equation (6.26) is satisfied, it is sufficient to guarantee equation (6.25) is satisfied too.

So for a MiL test with a determined input *i*, the maximum noise level for the signal not going saturation is:

$$\|n(j\omega)\|_\infty \le \frac{\lambda - \|i(j\omega)U_i(j\omega)\|_\infty}{\|U_n(j\omega)\|_\infty} \tag{6.27}$$

An example is given to examine whether the noise level is above the saturation level. To measure the actual noise level in the experiment with the rig described in Chapter

5, another experiment is done, the input position demand is a single frequency sine wave signal, the frequency of which is 1 Hz. Without any force feedback to the closed loop, the unfiltered force information is collected, and plotted in Figure 6.10. To analyse the composition of the noise, the force information is Fourier transformed and illustrated in Figure 6.11.

It can be seen from Figure 6.11 that, in the FFT result of the force analysis, except for the peak at 1Hz (which is obviously the main signal that needs to be reproduced), there's a sharp peak at 100Hz, with the amplitude of 110N. And the harmonics at 200Hz, 300Hz and 400Hz are also observed. This suggests that the main composite of the noise is a 100Hz single frequency sine wave signal.

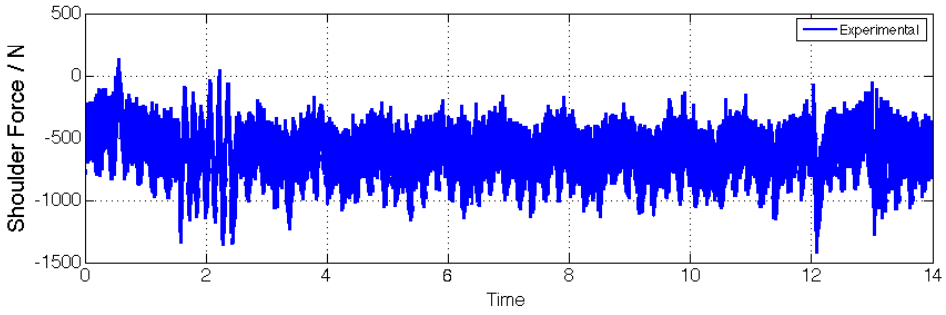

Figure 6.10 The unfiltered force information

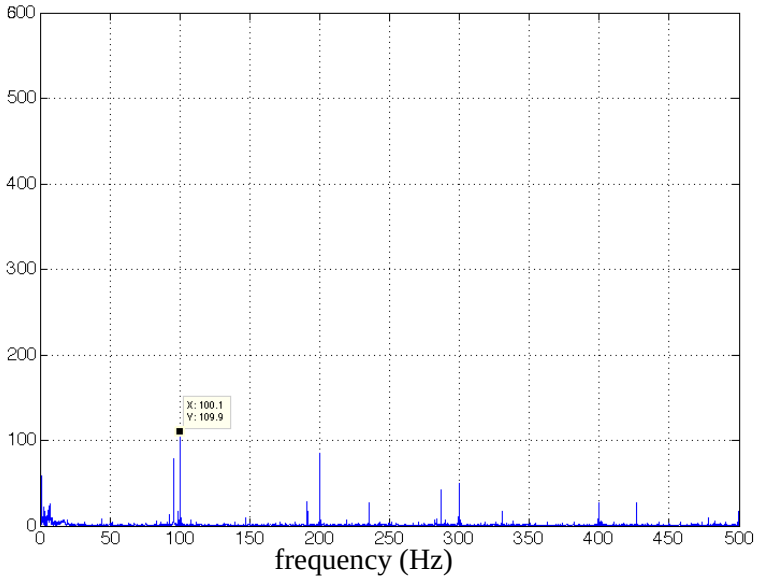

Figure 6.11 The FFT of the force information

For the experiment as described in Chapter 5, the input position is a chirp signal, the frequency of which increases from 0.5Hz to 2Hz, and the displacement amplitude is 0.0077m.

So for the specified input *i*, $\|i(j\omega)U_i(j\omega)\|_\infty$ can be calculated, for the MiL system with inverse model compensator and H_∞ optimized compensator respectively. The amplitude of $i(j\omega)U_i(j\omega)$ with different compensators are plotted Figure 6.12.

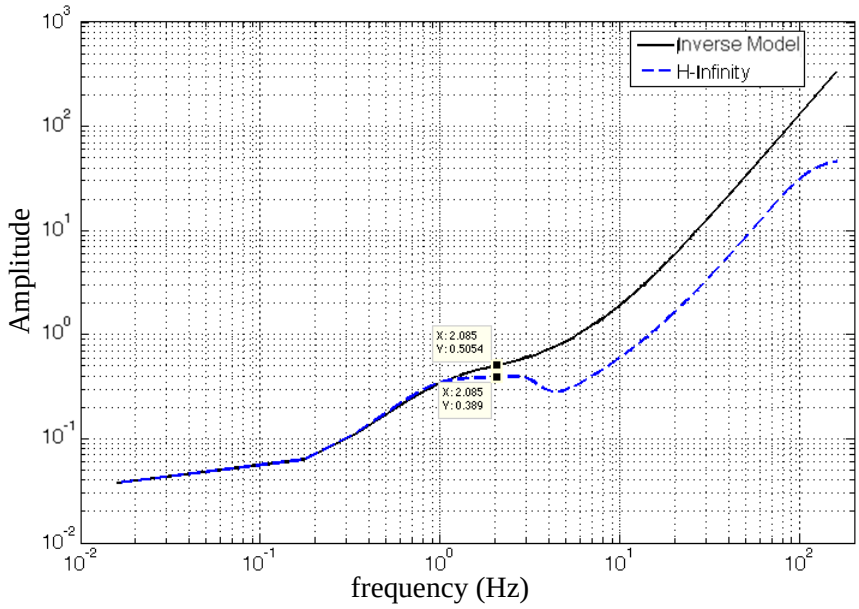

Figure 6.12 $i(j\omega)U_i(j\omega)$ with different compensators

It can be seen from Figure 6.12, for the MiL system with inverse model compensator, $\|i(j\omega)U_i(j\omega)\|_\infty = 0.5054$, and for the MiL system with H_∞ optimized compensator, $\|i(j\omega)U_i(j\omega)\|_\infty = 0.389$. These maxima occur at the upper end of the frequency range, i.e. 2Hz. They are the maximum normalised control signal amplitudes, where the saturation limit is λ=1.

The maximum noise level requirements can then be calculated with equation (6.26), and is illustrated in Figure 6.13. (λ=1)

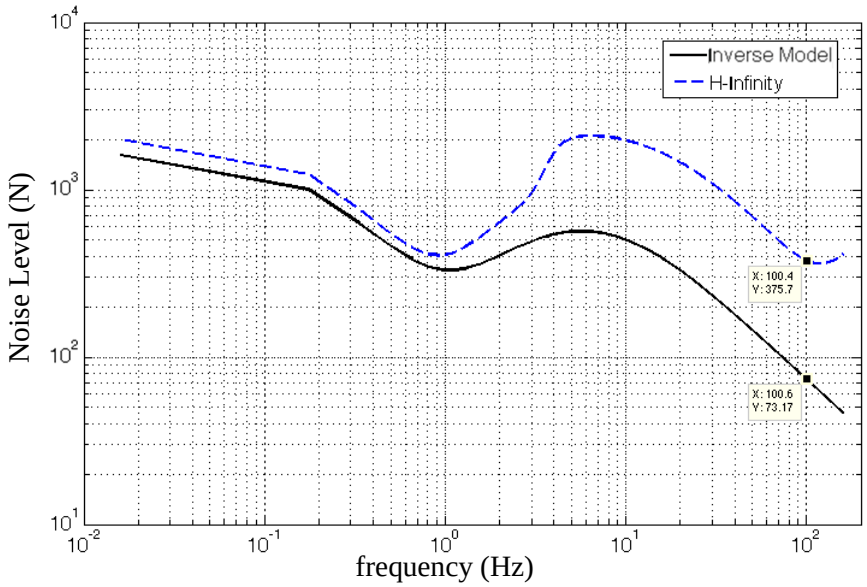

Figure 6.13 The maximum noise level requirements

Recall that according to the FFT analysis, the actual experimental measurement noise level is 110N, which is higher than the maximum noise level for the system with inverse model compensator. As a result, the signal saturate as shown in the experiment, and the saturation made the testing result very inaccurate. However, it can be observed from Figure 6.13 that the system using the H_∞ optimized compensator has a much higher margin, and the actual noise level falls under the safe margin. This has been verified in the experiment results in Chapter 5 that when using the H_∞ optimized compensator, no saturation is observed.

6.4 Concluding Remarks

In conclusion, in this chapter, an method based on the performance envelope of the valve/actuator system and the maximum control signal level is introduced to give a guide about choosing suitable hydraulic actuators and valves for a specific MiL test.

The analysis with the experimental results shows that the demonstrated method can be used as a way to choose the viable actuators and valves and to judge if the problem of saturation will occur in the control signal before actually building the testing system.

It can also be concluded from the performance envelope analysis that, the H_∞ optimized compensator can effectively broaden the usable frequency range of the valve/actuator system, and will provide a larger margin for the input signal level and the measurement noise level before saturation of the signal, thus reducing the performance levels needed by the actuation system.

Chapter 7

7 Conclusions and Future Work

7.1 Conclusions

Model-in-the-Loop (MiL) testing is a method in which the test object is split into a physical part and a simulated part, and these are connected with interfaces to form a combined physical-numerical system. It is a method that combines the advantages of physical testing and computer simulation: the feasibility of physically testing the hard-to-model characteristics of the test specimen, and the economy and flexibility of the computer simulation for other parts. It is a method being used in various areas, such as seismic test, automotive industry, and aerospace industry, and has a growing popularity.

In this thesis, a general procedure for analysing and implementing a MiL test is proposed.

Firstly, the structure and the characteristics of MiL systems are analysed with two example systems: a single mass-spring-damper MiL system, and a two DOF mass-spring-damper MiL system. Although only these two examples are used for the analysis, the method can be generalised, and so systems with more degrees of freedom can be analysed with the same approach. In the analysis, the method of building a MiL test system based on the mathematical model of the whole system is shown: where to split the system, and what signals to use to link the physical subsystem and the numerical subsystem back together. The process of stability analysis is presented for checking the stability margin of the MiL system. The problems introduced by the actuator dynamics and measurement noise are examined. It is shown in simulation that with a relatively slow actuator and realistic measurement noise level, the design of the compensator is challenging.

Secondly, a compensator design approach based on H_∞ loop shaping is presented. For the optimization, a two-input two-output system is constructed, with the input position demand and the measurement noise as the two inputs, and the target testing result error and the compensated signal as the two outputs. It is notable that the structure of comparing the target testing result and that of the ideal reference model is unique, and it is the core of the proposed compensator design method. It is shown with simulation results that the H_∞ optimized compensator not only compensates for the actuator dynamics accurately and effectively attenuates the high frequency response in the compensated signal excited by the measurement noise, but the phase lift effect of the H_∞ optimized compensator makes it even better than the implemented inverse model based compensator in reducing the time delay in certain frequency ranges. The effectiveness of the H_∞ optimized compensator is then verified with experimental results. A MiL test is generated on the basis of a two-axis robotic arm used as a limb of the Italian Institute of Technology HyQ robot. The experimental system exhibited typical practical constraints in terms of limited actuator dynamics and structural vibration issues, but the H_∞ optimized compensator clearly shows its advantages in terms of accuracy and saturation rejection when compared with inverse model based compensators.

Thirdly, a general approach is introduced to give a guide about choosing suitable hydraulic actuators and valves for a specific MiL test based on the performance envelope of the valve/actuator system and the maximum control signal level. The analysis with the experimental results shows that the described method can be used as a way to choose the viable actuators and valves and to judge if the problem of saturation will occur in the control signal before actually building the testing system. It can also be concluded from the performance envelope analysis that, the H_∞ optimized compensator can broaden the usable frequency range of the valve/actuator system, and will provide a larger margin for control signal saturation, thus reducing the performance levels needed by the actuation system.

7.2 Recommendations for Future Work

The research presented in this thesis could be further investigated in the following areas in the future:

1. The proposed compensator optimization method based on H_∞ loop shaping could be experimentally tested with more applications and more types of input demands, for example vehicle engine vibration test, and wave energy convertor test, with inputs of square waves or triangular waves.
2. The proposed compensator optimization method based on H_∞ loop shaping could be analysed and experimentally tested in systems with higher degrees of freedom and multiple actuators.
3. The mechanism of signal saturation and how exactly the MiL system is affected when signal saturation occurs need further investigation.
4. More research could be done about improving the robustness of the optimized compensator.

References

[1] A. R. Plummer, "Model-in-the-loop testing," *Proceedings of the Institution of Mechanical Engineers, Part I: Journal of Systems and Control Engineering,* vol. 220, no. 3, pp. 183-199, 2006.

[2] H. K. Fathy, Z. S. Filipi, J. Hagena and J. L. Stein, "Review of Hardware-in-the-Loop Simulation and Its Prospects in the Automotive Area," *SPIE Proceedings,* vol. 6228, 2006.

[3] M. Montazeri-Gh, M. Nasiri, M. Rajabi and M. Jamshidfard, "Actuator-based hardware-in-the-loop testing of a jet engine fuel control unit in flight conditions," *Simulation Modelling Practice and Theory,* vol. 21, pp. 65-77, 2012.

[4] T. Börner and M.-R. Alam, "Real time hybrid modeling for ocean wave energy converters," *Renewable and Sustainable Energy Reviews,* vol. 43, pp. 784-795, 2015.

[5] V. Chabaud, "Real-Time Hybrid Model Testing of Floating Wind Turbines," 2016.

[6] T. Horiuchi, M. Inoue, T. Konno and Y. Namita, "Real-time hybrid experimental system with actuator delay compensation and its application to a piping system with energy absorber," *EARTHQUAKE ENGINEERING AND STRUCTURAL DYNAMICS,* vol. 28, pp. 1121-1141, 1999.

[7] T. Horiuchi and T. Konno, "A new method for compensating actuator delay in real-time hybrid experiments," *Dynamic testing of structures: compiled by M. S. Williams,* vol. 359, no. 1786, 2001.

[8] C. Chen and J. M. Ricles, "Analysis of actuator delay compensation methods for real-time testing," *Engineering Structures,* vol. 31, pp. 2643-2655, 2009.

[9] R.-Y. Jung and P. B. Shing, "Performance evaluation of a real-time pseudodynamic test," *EARTHQUAKE ENGINEERING AND STRUCTURAL DYNAMICS,* vol. 35, pp. 789-810, 2006.

[10] C. Chen and J. M. Ricles, "Improving the inverse compensation method for real-time hybrid simulation through a dual compensation scheme," *EARTHQUAKE ENGINEERING AND STRUCTURAL DYNAMICS,* vol. 38, pp. 1237-1255, 2009.

[11] C. Chen and J. M. Ricles, "Tracking Error-Based Servohydraulic Actuator Adaptive Compensation for Real-Time Hybrid Simulation," *JOURNAL OF STRUCTURAL ENGINEERING,* vol. 136, pp. 432-440, 2010.

[12] J. L. d. Bois, B. Titurus and N. A. J. Lieven, "Transfer Dynamics Cancellation in Real-Time Dynamic Substructuring," in *ISMA 2010 International Conference on Noise and Vibration Engineering*, 2010.

[13] A. P. Darby, A. Blakeborough and M. S. Williams, "Improved control algorithm for real-time substructure testing," *EARTHQUAKE ENGINEERING AND STRUCTURAL DYNAMICS,* vol. 30, pp. 431-448, 2001.

[14] A. P. Darby, M. S. Williams and A. Blakeborough, "Stability and Delay Compensation for Real-Time Substructure Testing," *Journal of Engineering Mechanics,* vol. 128, pp. 1276-1284, 2002.

[15] M. Ahmadizadeh, G. Mosqueda and A. M. Reinhorn, "Compensation of actuator delay and dynamics for real-time hybrid structural simulation," *EARTHQUAKE ENGINEERING AND STRUCTURAL DYNAMICS,* vol. 37, pp. 21-42, 2007.

[16] F. Zhu, J.-T. Wang, F. Jin and Y. Gui, "Comparison of explicit integration algorithms for real-time hybrid simulation," *Bulletin of Earthquake Engineering,* vol. 14, no. 1, pp. 89-114, 2016.

[17] A. Maghareh, J. P. Waldbjoern, S. J. Dyke, A. Prakash and A. I. Ozdagli, "Development of Adaptive Multi-Rate Interface for Real-time Hybrid Simulation," in *6th International Conference on Advances in Experimental Structural Engineering*, 2015.

[18] K. Nikzad, J. Ghaboussi and S. L. Paul, "Actuator Dynamics and Delay Compensation Using Neurocontrollers," *Journal of Engineering Mechanics,* vol. 122, no. 10, pp. 966-975, 1996.

[19] D. J. Wagg and D. P. Stoten, "Substructuring of dynamical systems via the adaptive minimal control synthesis algorithm," *EARTHQUAKE ENGINEERING AND STRUCTURAL DYNAMICS,* vol. 30, pp. 865-877, 2001.

[20] D.P.Stoten, "An overview of the minimal control synthesis algorithm," 1993.

[21] S. A. Neild, D. Drury and D. P. Stoten, "An Improved Substructuring Control Strategy based on the Adaptive Minimal Control Synthesis Control Algorithm," *Proceedings of the Institution of Mechanical Engineers, Part I: Journal of Systems and Control Engineering,* vol. 219, no. 5, pp. 305-317, 2005.

[22] B. A. Bonnet, C. N. Lim, M. S. Williams, A. Blakeborough, S. A. Neild, D. P. Stoten and C. A. Taylor, "Real-time hybrid experiments with Newmark integration, MCSmd outer-loop control and multi-tasking strategies," *EARTHQUAKE ENGINEERING AND STRUCTURAL DYNAMICS,* vol. 36, pp. 119-141, 2007.

[23] G. Li, D. P. Stoten and J. -Y. Tu, "Model predictive control of dynamically substructured systems with application to a servohydraulically actuated mechnical plant," *IET Control Theory and Applications,* vol. 4, no. 2, pp. 253-264, 2009.

[24] G. Li, G. Herrmann, D. P. Stoten, J. Tu and M. C. Turner, "Application of Robust Antiwindup Techniques to Dynamically Substructured Systems," *IEEE/ASME TRANSACTIONS ON MECHATRONICS,* vol. 18, no. 1, pp. 263-272, 2013.

[25] G. Ou, A. I. Ozdagli, S. J. Dyke and B. Wu, "Robust integrated actuator control: experimental verification and real-time hybrid simulation implementation," *EARTHQUAKE ENGINEERING & STRUCTURAL DYNAMICS,* vol. 44, no. 3, pp. 441-460, 2014.

[26] A. R. Plummer, "Integrating virtual components into mechanical systems: some actuator control issues," in *IMechE Seminar on Recent advances in control techniques for actuators*, London, 2002.

[27] A. Ghorashi, "Linear Decentralised Modelling for H∞ Control of a Multi-Axis Simulation Table," Thesis (Doctor of Philosophy (PhD)), University of Bath, 2009.

[28] S. Skogestad and I. Postlethwaite, Multivariable Feedback Control: Analysis and Design, WILEY, 2005.

[29] C. Semini, "Information Package on the Robot Leg HyQ-Leg V2.1".

[30] C. Du, A. R. Plummer and D. N. Johnston, "Performance Analysis of a New Energy-efficient Variable Supply Pressure Electrohydraulic Motion Control Method," *Control Engineering Practice,* vol. 48, pp. 10-21, 2016.

[31] C. Du, "Variable Supply Pressure Electrohydraulic System for Efficient Multi-axis Motion Control," Thesis (Doctor of Philosophy (PhD)), University of Bath, 2014.

[32] N. M. Newmark, "A method of computation for structural dynamics," *Journal of Engineering Mechanics (ASCE),* vol. 85, no. 3, pp. 67-94, 1959.

[33] A. M. El-Nagar and M. El-Bardini, "Hardware-in-the-loop simulation of interval type-2 fuzzy PD controller for uncertain nonlinear system using low cost microcontroller," *Applied Mathematical Modelling,* vol. 40, no. 3, pp. 2346-2355, 2015.

Appendix

Appendix 3 Analysis of MiL Systems

Appendix 3.1 Models in Simulink

Appendix 3.1.1 Simulink model to verify the stability of the single mass-spring-damper based MiL system

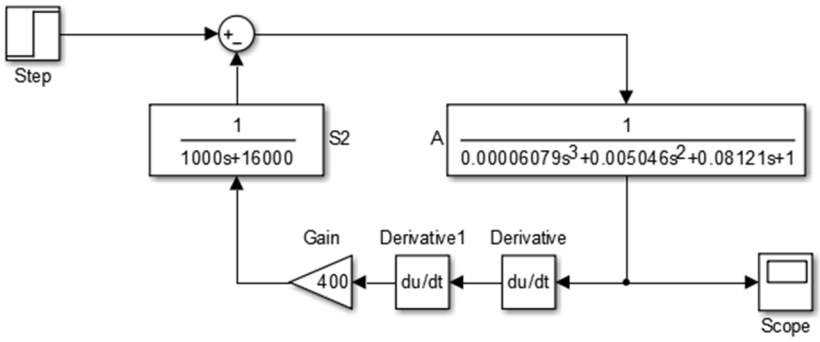

Figure A.1 The diagram of the one DOF MiL system in Simulink

Appendix 3.1.2 Simulink model to verify the stability of the two DOF mass-spring-damper based MiL system

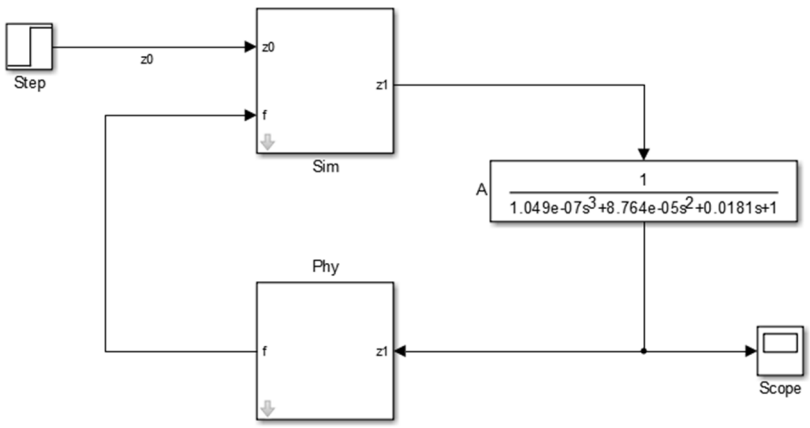

Figure A.2 The diagram of the two DOF MiL system in Simulink

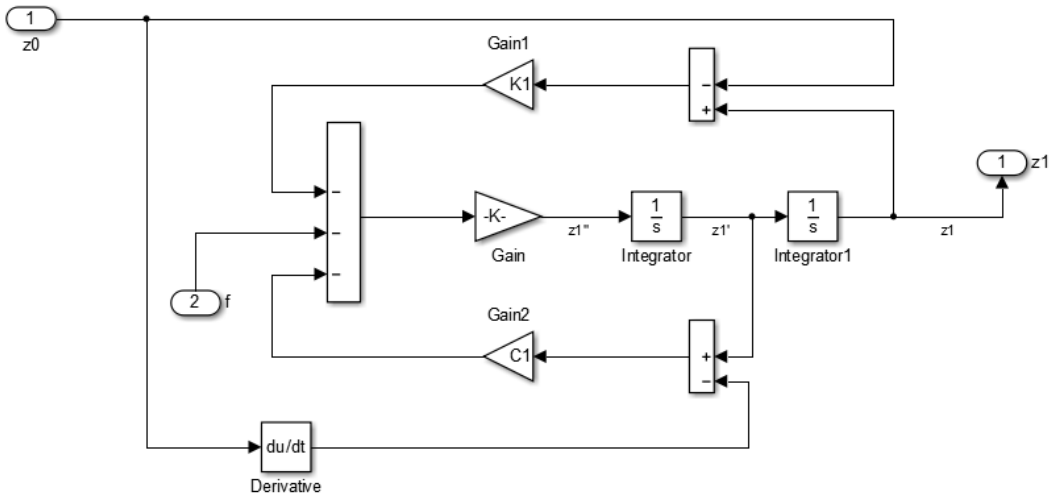

Figure A.3 The diagram of the simulation subsystem in Simulink

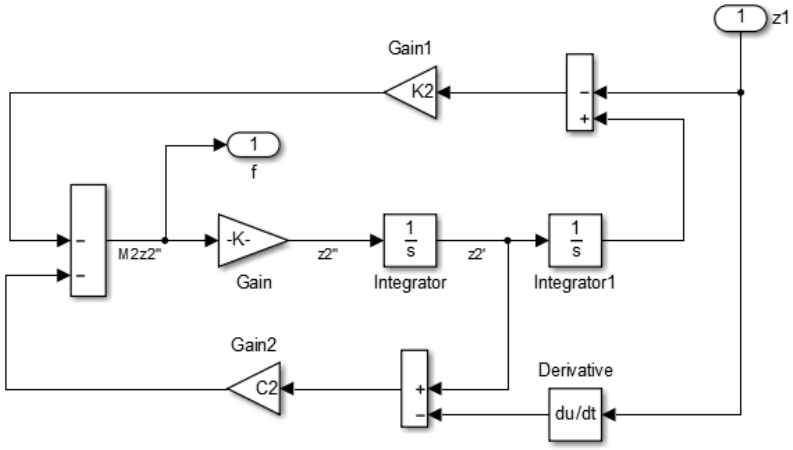

Figure A.4 The diagram of the physical subsystem in Simulink

Appendix 3.1.3 Simulink model to check the influence of the measurement noise to the compensated signal in the one DOF MiL system

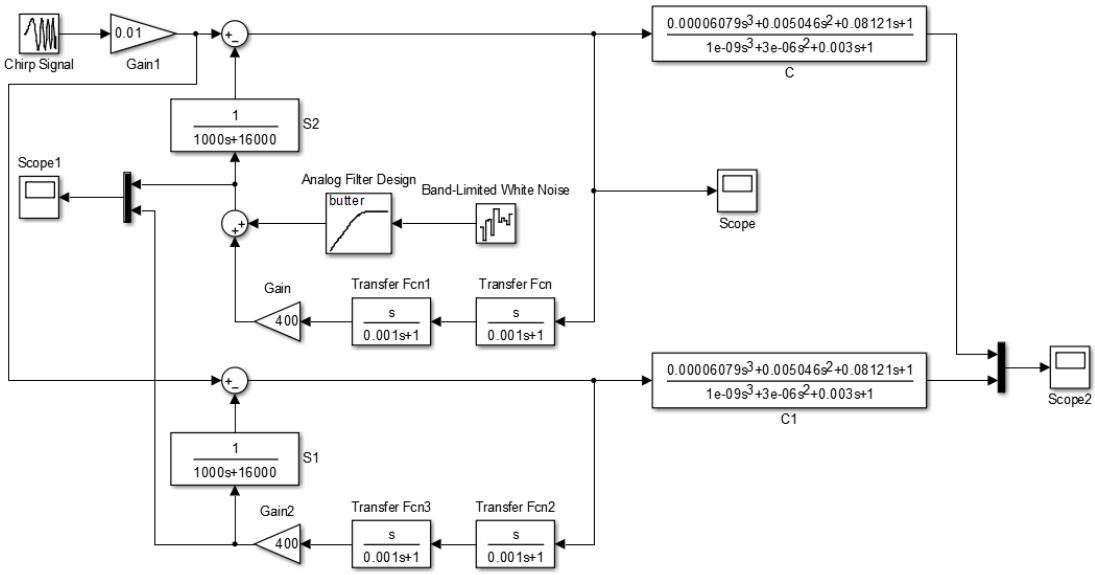

Figure A.5 The diagram of the MiL systems with and without the added noise in Simulink

Appendix 3.1.4 Simulink model to check the influence of the disturbance force to the compensated signal in the two DOF MiL system

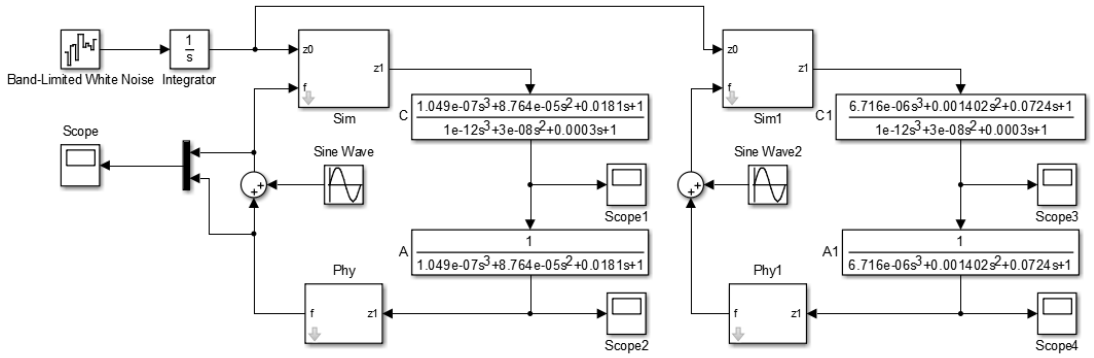

Figure A.6 The diagram of the MiL systems with and without the added disturbance force in Simulink

Appendix 3.2 Derivation of Equations

Appendix 3.2.1 Derivation of the transfer function from the vibration force *v* to the displacement z_1

The equations for the described MiL system is listed as follows.

$$-f-(C_1 s+K_1)(z_{1d}-z_0)=M_1 s^2 z_{1d} \tag{A.3.1}$$

$$-(C_2 s+K_2)(z_2-z_1)-v=M_2 s^2 z_2=f \tag{A.3.2}$$

$$\frac{z_1}{z_{1d}}=A(s) \tag{A.3.3}$$

To find the transfer functions from the engine vibration force *v* to the displacement z_1, let $z_0 = 0$:

$$-f-(C_1 s+K_1)z_{1d}=M_1 s^2 z_{1d} \tag{A.3.4}$$

It can be shown that:

$$-(C_2 s+K_2)(z_2-z_1)-v=M_2 s^2 z_2 \tag{A.3.5}$$

$$(C_2 s+K_2)z_1-v=(M_2 s^2+C_2 s+K_2)z_2 \tag{A.3.6}$$

$$z_2=\frac{(C_2 s+K_2)z_1-v}{M_2 s^2+C_2 s+K_2} \tag{A.3.7}$$

$$f=M_2 s^2\frac{(C_2 s+K_2)z_1-v}{M_2 s^2+C_2 s+K_2} \tag{A.3.8}$$

Substitute equations (A.3.3) and (A.3.8) into equation (A.3.4).

$$-M_2 s^2 \frac{(C_2 s + K_2) z_1 - v}{M_2 s^2 + C_2 s + K_2} = \frac{M_1 s^2 + C_1 s + K_1}{A(s)} z_1 \tag{A.3.9}$$

$$\frac{M_2 s^2}{M_2 s^2 + C_2 s + K_2} v = \frac{M_1 s^2 + C_1 s + K_1}{A(s)} z_1 + \frac{M_2 s^2 (C_2 s + K_2)}{M_2 s^2 + C_2 s + K_2} z_1 \tag{A.3.10}$$

$$M_2 s^2 v = \frac{A(s) M_2 s^2 (C_2 s + K_2) + (M_1 s^2 + C_1 s + K_1)(M_2 s^2 + C_2 s + K_2)}{A(s)} z_1 \tag{A.3.11}$$

$$\frac{z_1}{v} = \frac{A(s) M_2 s^2}{(M_1 s^2 + C_1 s + K_1)(M_2 s^2 + C_2 s + K_2) + A(s) M_2 s^2 (C_2 s + K_2)} \tag{A.3.12}$$

Compared with the transfer function from the measurement noise n to the displacement z_1:

$$\frac{z_1}{n} = -\frac{A(s)(M_2 s^2 + C_2 s + K_2)}{(M_1 s^2 + C_1 s + K_1)(M_2 s^2 + C_2 s + K_2) + A(s) M_2 s^2 (C_2 s + K_2)} \tag{A.3.13}$$

$$\frac{z_1}{v} = -\frac{M_2 s^2}{M_2 s^2 + C_2 s + K_2} \frac{z_1}{n} \tag{A.3.14}$$

Appendix 3.2.2 Derivation of the transfer function from the measurement noise n to the compensated signal z_{1c}

The equations for the MiL system built from a two DOF mass-spring-damper system are shown as follows:

$$-(f + n) - (C_1 s + K_1)(z_{1d} - z_0) = M_1 s^2 z_{1d} \tag{A.3.15}$$

$$-(C_2 s + K_2)(z_2 - z_1) = M_2 s^2 z_2 = f \tag{A.3.16}$$

$$\frac{z_{1c}}{z_{1d}} = \frac{1}{A(s)} \tag{A.3.17}$$

$$\frac{z_1}{z_{1c}} = A(s) \tag{A.3.18}$$

To find the transfer functions from the noise n to the desired displacement z_{1d} and the compensated signal z_{1c}, let $z_0 = 0$:

$$-(f+n)-(C_1 s + K_1) z_{1d} = M_1 s^2 z_{1d} \tag{A.3.19}$$

It can be shown that:

$$z_2 = \frac{C_2 s + K_2}{M_2 s^2 + C_2 s + K_2} z_1 \tag{A.3.20}$$

Substitute equation (3.66) into equation (3.69):

$$-(M_2 s^2 z_2 + n)-(C_1 s + K_1) z_{1d} = M_1 s^2 z_{1d} \tag{A.3.21}$$

$$-n = (M_1 s^2 + C_1 + K_1) z_{1d} + M_2 s^2 z_2 \tag{A.3.22}$$

Substitute equation (3.70) into equation (3.72):

$$-n = (M_1 s^2 + C_1 + K_1) z_{1d} + \frac{M_2 s^2 (C_2 s + K_2)}{M_2 s^2 + C_2 s + K_2} z_1 \tag{A.3.23}$$

Notice that $z_1 = z_{1d}$:

$$-n = \frac{(M_1 s^2 + C_1 s + K_1)(M_2 s^2 + C_2 s + K_2) + M_2 s^2 (C_2 s + K_2)}{M_2 s^2 + C_2 s + K_2} z_{1d} \tag{A.3.24}$$

$$\frac{z_{1d}}{n} = -\frac{M_2 s^2 + C_2 s + K_2}{\left(M_1 s^2 + C_1 s + K_1\right)\left(M_2 s^2 + C_2 s + K_2\right) + M_2 s^2 \left(C_2 s + K_2\right)} \tag{A.3.25}$$

$$\frac{z_{1c}}{n} = -\frac{M_2 s^2 + C_2 s + K_2}{\left(\left(M_1 s^2 + C_1 s + K_1\right)\left(M_2 s^2 + C_2 s + K_2\right) + M_2 s^2 \left(C_2 s + K_2\right)\right) A(s)} \tag{A.3.26}$$

Appendix 3.2.3 Derivation of the transfer function from the vibration force *v* to the compensated signal z_{1c}

The equations for the MiL system in this example is listed as follows.

$$-f - \left(C_1 s + K_1\right)\left(z_{1d} - z_0\right) = M_1 s^2 z_{1d} \tag{A.3.27}$$

$$-\left(C_2 s + K_2\right)\left(z_2 - z_1\right) - v = M_2 s^2 z_2 = f \tag{A.3.28}$$

$$\frac{z_{1c}}{z_{1d}} = \frac{1}{A(s)} \tag{A.3.29}$$

$$\frac{z_1}{z_{1c}} = A(s) \tag{A.3.30}$$

To find the transfer functions from the engine vibration force v to the desired displacement z_{1d} and the compensated signal z_{1c}, let $z_0 = 0$:

$$-f - \left(C_1 s + K_1\right) z_{1d} = M_1 s^2 z_{1d} \tag{A.3.31}$$

It can be shown that:

$$-\left(C_2 s + K_2\right)\left(z_2 - z_1\right) - v = M_2 s^2 z_2 \tag{A.3.32}$$

$$\left(C_2 s + K_2\right) z_1 - v = \left(M_2 s^2 + C_2 s + K_2\right) z_2 \tag{A.3.33}$$

$$z_2 = \frac{(C_2 s + K_2) z_1 - v}{M_2 s^2 + C_2 s + K_2} \tag{A.3.34}$$

$$f = M_2 s^2 \frac{(C_2 s + K_2) z_1 - v}{M_2 s^2 + C_2 s + K_2} \tag{A.3.35}$$

Substitute equation (A.3.21) into equation (A.3.17):

$$-M_2 s^2 \frac{(C_2 s + K_2) z_1 - v}{M_2 s^2 + C_2 s + K_2} = (M_1 s^2 + C_1 s + K_1) z_{1d} \tag{A.3.36}$$

Notice that $z_1 = z_{1d}$:

$$\frac{M_2 s^2}{M_2 s^2 + C_2 s + K_2} v = (M_1 s^2 + C_1 s + K_1) z_{1d} + \frac{M_2 s^2 (C_2 s + K_2)}{M_2 s^2 + C_2 s + K_2} z_{1d} \tag{A.3.37}$$

$$M_2 s^2 v = (M_1 s^2 + C_1 s + K_1)(M_2 s + C_2 + K_2) z_{1d} + M_2 s^2 (C_2 s + K_2) z_{1d} \tag{A.3.38}$$

$$\frac{z_{1d}}{v} = \frac{M_2 s^2}{(M_1 s^2 + C_1 s + K_1)(M_2 s + C_2 + K_2) + M_2 s^2 (C_2 s + K_2)} \tag{A.3.39}$$

$$\frac{z_{1c}}{v} = \frac{M_2 s^2}{((M_1 s^2 + C_1 s + K_1)(M_2 s + C_2 + K_2) + M_2 s^2 (C_2 s + K_2)) A(s)} \tag{A.3.40}$$

Comparing the transfer functions $\frac{z_{1c}}{n}$ and $\frac{z_{1c}}{v}$:

$$\frac{z_{1c}}{n} = -\frac{M_2 s^2 + C_2 s + K_2}{((M_1 s^2 + C_1 s + K_1)(M_2 s^2 + C_2 s + K_2) + M_2 s^2 (C_2 s + K_2)) A(s)} \tag{A.3.41}$$

$$\frac{z_{1c}}{v} = -\frac{M_2 s^2}{M_2 s^2 + C_2 s + K_2} \frac{z_{1c}}{n} \tag{A.3.42}$$

Appendix 4 Compensator Design with H_∞ Loop Shaping

Appendix 4.1 MATLAB Codes for H_∞ Optimization

Appendix 4.1.1 MATLAB Codes for the H_∞ Optimization of the single mass-spring-damper based MiL system

```
clear all;

%Define the compensator and the actuator
A= tf(1, [0.00006079, 0.005046, 0.08121, 1]);

AR = tf([0.00006079, 0.005046, 0.08121, 1], 1);
POLE = tf(1, [0.01, 1]);
ZERO = tf([0.01, 1], 1);
C = ltiblock.tf('C', AR*(ZERO)*(POLE^4));


%Define the blocks
M = 400;
C1 = 4000;
K = 16000;

S1 = tf(1);
S2 = -tf(1, [C1, K]);
S1R = tf(1);
S2R = -tf(1, [C1, K]);

P = tf([M 0 0], 1);
PR = tf([M 0 0], 1);

NOISE = tf(1);


%Label the block I/Os
NOISE.u = 'n';   NOISE.y = 'ny';

S1.u = 'z0';   S1.y = 's1y';
S2.u = 'ff';   S2.y = 's2y';

S1R.u = 'z0';   S1R.y = 's1yr';
S2R.u = 'fr';   S2R.y = 's2yr';

P.u = 'z1';   P.y = 'f';
PR.u = 'z1r';   PR.y = 'fr';
```

```
C.u = 'z1d';   C.y = 'z1c';
A.u = 'z1c';   A.y = 'z1';


%Specify summing junctions
Sum1 = sumblk('z1d = s1y+s2y');
Sum2 = sumblk('ff = f+ny');
Sum3 = sumblk('z1r = s1yr+s2yr');
Sum4 = sumblk('e = z1r-z1');

%Connect the blocks together
T0 = connect(S1,S2,P,C,A,S1R,S2R,PR,NOISE,Sum1,Sum2,Sum3,Sum4,
{'z0','n'},{'e','z1c'});

T0(2,1) = 0;
T0(1,2) = 0;

FILTER = tf(1, [0.01, 1]);
M_FILTER = blkdiag(FILTER, FILTER);
T0F = T0*M_FILTER;

UB1 = 1/norm(T0F(1,1), inf);
UB2 = 1/norm(T0F(2,2), inf);


%Define the weighting functions
s = tf('s');

n0 = 1;
wl0 = 4*2*pi;
whd0 = 4*2*pi;
whn0 = 1*2*pi;
LS101 = 1*UB1/(((s/wl0)^2 + 2*0.7*(s/wl0) + 1)*(s+0.001));
LS201 = n0*UB2*(s^2 + 2*0.7*s*whn0 + (whn0^2))/(s^2 + 2*0.5*s*whd0 +
(whd0^2));

LS10 = LS101*FILTER;
LS20 = LS201*FILTER;


%Weight the system
T1 = blkdiag(LS10, LS20) * T0;


%Random initial value to avoid being caught in local minimums
opts = hinfstructOptions('RandomStart',20);


%Tune the compensator with hinfstruct function
[T_0,gamma0,info0] = hinfstruct(T1,opts);
C0 = tf(T_0.Blocks.C);
N = T_0.Blocks.C.num.Value;
D = T_0.Blocks.C.den.Value;
%Unweight the system to get the actual tuned system
FO0 = blkdiag(LS10, LS20);
```

```
Ta = FO0\T_0;

Original = tf(T0);
Weighted_n1 = tf(T1);
Hinf_weighted_n1 = tf(T_0);
Hinf_actual_n1 = tf(Ta);

RLS10 = gamma0/LS10;
RLS20 = gamma0/LS20;


%Optimization for another value of n2
n1 = 1.5;
wl1 = 4*2*pi;
whd1 = 4*2*pi;
whn1 = 1*2*pi;
LS111 = 1*UB1/(((s/wl1)^2 + 2*0.7*(s/wl1) + 1)*(s+0.001));
LS211 = n1*UB2*(s^2 + 2*0.7*s*whn1 + (whn1^2))/(s^2 + 2*0.5*s*whd1 +
(whd1^2));

LS11 = LS111*FILTER;
LS21 = LS211*FILTER;

T11 = blkdiag(LS11, LS21) * T0;

opts = hinfstructOptions('RandomStart',20);
[T_1,gamma1,info1] = hinfstruct(T11,opts);
C1 = tf(T_1.Blocks.C)
N1 = T_1.Blocks.C.num.Value;
D1 = T_1.Blocks.C.den.Value;

FO1 = blkdiag(LS11, LS21);
Ta1 = FO1\T_1;

Weighted_n2 = tf(T11);
Hinf_weighted_n2 = tf(T_1);
Hinf_actual_n2 = tf(Ta1);

RLS11 = gamma1/LS11;
RLS21 = gamma1/LS21;

%Plot the results
figure
bode(Original(1,1),'k', Hinf_actual_n1(1,1),'k--',
Hinf_actual_n2(1,1),'b--', 1/LS10,'k-.', 1/LS11,'k-.', opts1);
legend('Original System','Optimized System n1','Optimized System
n1.5','Loop Shape');
h = findobj(gcf, 'Type','line');
set(h, 'LineWidth', 2);
set(findall(gcf,'Type','text'),'FontSize',20);
set(findall(gcf,'Type','axes'),'FontSize',16,'XColor','black','YColo
r','black');

figure
```

```
bode(Original(2,2),'k', Hinf_actual_n1(2,2),'k--',
Hinf_actual_n2(2,2),'b--', 1/LS20,'k-.', 1/LS21,'b-.', opts1);
legend('Original System','Optimized System n1','Optimized System
n1.5','Loop Shape n1','Loop Shape n1.5');
h = findobj(gcf, 'Type','line');
set(h, 'LineWidth', 2);
set(findall(gcf,'Type','text'),'FontSize',20);
set(findall(gcf,'Type','axes'),'FontSize',16,'XColor','black','YColo
r','black');

figure
bode(C0,'k', C1,'b', opts1);
legend('Compensator n1','Compensator n1.5');
h = findobj(gcf, 'Type','line');
set(h, 'LineWidth', 2);
set(findall(gcf,'Type','text'),'FontSize',20);
set(findall(gcf,'Type','axes'),'FontSize',16,'XColor','black','YColo
r','black');
```

Appendix 4.1.2 MATLAB Codes for the H_∞ Optimization of two DOF mass-spring-damper based MiL system

```
clear all;


%Define the compensator and the actuator
C = ltiblock.tf('C', tf([8.395e-11, 8.746e-07, 0.0003542, 0.0363,
1], [6.25e-18, 5e-13, 1.5e-08, 0.0002, 1]));

A= tf(1, [8.395e-07, 0.0003506, 0.0362, 1]);


%Define the blocks
M1 = 415;
C1 = 1000;
K1 = 20000;
M2 = 100;
C2 = 100;
K2 = 20000;

S1 = tf([C1 K1], [M1 C1 K1]);
S2 = -tf(1, [M1 C1 K1]);
S1R = tf([C1 K1], [M1 C1 K1]);
S2R = -tf(1, [M1 C1 K1]);

P1 = tf([M2*C2 M2*K2 0 0],[M2 C2 K2]);
P2 = tf([C2 K2],[M2 C2 K2]);
P1R = tf([M2*C2 M2*K2 0 0],[M2 C2 K2]);
P2R = tf([C2 K2],[M2 C2 K2]);

NOISE = tf([M2 0 0],[M2 C2 K2]);
% Label the block I/Os
```

```
NOISE.u = 'n';   NOISE.y = 'ny';

S1.u = 'z0';   S1.y = 's1y';
S2.u = 'ff';   S2.y = 's2y';

S1R.u = 'z0';   S1R.y = 's1yr';
S2R.u = 'ffr';   S2R.y = 's2yr';

P1.u = 'z1';   P1.y = 'f';
P2.u = 'z1';   P2.y = 'z2';

P1R.u = 'z1r';   P1R.y = 'fr';
P2R.u = 'z1r';   P2R.y = 'z2r';

C.u = 'z1d';   C.y = 'z1c';
A.u = 'z1c';   A.y = 'z1';


% Specify summing junctions
Sum1 = sumblk('z1d = s1y+s2y');
Sum2 = sumblk('ff = f+ny');
Sum3 = sumblk('z1r = s1yr+s2yr');
Sum4 = sumblk('ffr = fr+ny');
Sum5 = sumblk('e = z2r-z2');

%Connect the blocks together
T0 =
connect(S1,S2,P1,P2,C,A,S1R,S2R,P1R,P2R,NOISE,Sum1,Sum2,Sum3,Sum4,Su
m5, {'z0','n'},{'e','z1c'});

T0(2,1) = 0;
T0(1,2) = 0;

UB1 = 1/norm(T0(1,1), inf);
UB2 = 1/norm(T0(2,2), inf);

s = tf('s');

%Define the weighting functions
n0 = 20;
wl0 = 40*2*pi;
wh0 = 40*2*pi;
LS10 = 1*UB1/((s/wl0)^2 + 2*0.7*(s/wl0) + 1);
LS20 = n0*UB2*((s/wh0)^2)/((s/wh0)^2 + 2*0.7*(s/wh0) + 1);


%Weight the system
T10 = blkdiag(LS10, LS20) * T0;


%Random initial value to avoid being caught in local minimums
opts = hinfstructOptions('RandomStart',10);


%Tune the compensator with hinfstruct function
```

```
[T_0,gamma0,info0] = hinfstruct(T10,opts);
C0 = tf(T_0.Blocks.C)
N = T_0.Blocks.C.num.Value;
D = T_0.Blocks.C.den.Value;

FO0 = blkdiag(LS10, LS20);
Ta0 = FO0\T_0;


%Unweight the system to get the actual tuned system
Original = tf(T0);
Weighted_n2 = tf(T10);
Hinf_weighted_n2 = tf(T_0);
Hinf_actual_n2 = tf(Ta0);

RLS10 = gamma0/LS10;
RLS20 = gamma0/LS20;


%Optimization for another value of n2
n1 = 40;
wl1 = 40*2*pi;
wh1 = 40*2*pi;
LS11 = 1*UB1/((s/wl1)^2 + 2*0.7*(s/wl1) + 1);
LS21 = n1*UB2*((s/wh1)^2)/((s/wh1)^2 + 2*0.7*(s/wh1) + 1);

T11 = blkdiag(LS11, LS21) * T0;

opts = hinfstructOptions('RandomStart',10);
[T_1,gamma1,info1] = hinfstruct(T11,opts);
C1 = tf(T_1.Blocks.C)
N1 = T_1.Blocks.C.num.Value;
D1 = T_1.Blocks.C.den.Value;

FO1 = blkdiag(LS11, LS21);
Ta1 = FO1\T_1;

Weighted_n4 = tf(T11);
Hinf_weighted_n4 = tf(T_1);
Hinf_actual_n4 = tf(Ta1);

RLS11 = gamma1/LS11;
RLS21 = gamma1/LS21;


%Optimization for another value of n2
n2 = 100;
wl2 = 40*2*pi;
wh2 = 40*2*pi;
LS12 = 1*UB1/((s/wl2)^2 + 2*0.7*(s/wl2) + 1);
LS22 = n2*UB2*((s/wh2)^2)/((s/wh2)^2 + 2*0.7*(s/wh2) + 1);

T12 = blkdiag(LS12, LS22) * T0;

opts = hinfstructOptions('RandomStart',10);
```

```
[T_2,gamma2,info2] = hinfstruct(T12,opts);
C2 = tf(T_2.Blocks.C)
N2 = T_2.Blocks.C.num.Value;
D2 = T_2.Blocks.C.den.Value;

FO2 = blkdiag(LS12, LS22);
Ta2 = FO2\T_2;

Weighted_n8 = tf(T12);
Hinf_weighted_n8 = tf(T_2);
Hinf_actual_n8 = tf(Ta2);

RLS12 = gamma2/LS12;
RLS22 = gamma2/LS22;


%Plot the results
opts1 = bodeoptions('cstprefs');
opts1.FreqUnits = 'Hz';
opts1.Xlim = [0.1, 500];
opts1.Grid = 'on';

figure
bode(Original(1,1),'k', Hinf_actual_n2(1,1),'k--',
Hinf_actual_n4(1,1),'b--', Hinf_actual_n8(1,1),'r--', 1/LS10,'k-.',
1/LS11,'b-.', 1/LS12,'r-.', opts1);
legend('Original System','Optimized System n10','Optimized System
n20','Optimized System n40','Loop Shape');
h = findobj(gcf, 'Type','line');
set(h, 'LineWidth', 2);
set(findall(gcf,'Type','text'),'FontSize',20);
set(findall(gcf,'Type','axes'),'FontSize',16,'XColor','black','YColo
r','black');

figure
bode(Original(2,2),'k', Hinf_actual_n2(2,2),'k--',
Hinf_actual_n4(2,2),'b--', Hinf_actual_n8(2,2),'r--', 1/LS20,'k-.',
1/LS21,'b-.', 1/LS22,'r-.', opts1);
legend('Original System','Optimized System n10','Optimized System
n20','Optimized System n40','Loop Shape n10','Loop Shape n20','Loop
Shape n40');
h = findobj(gcf, 'Type','line');
set(h, 'LineWidth', 2);
set(findall(gcf,'Type','text'),'FontSize',20);
set(findall(gcf,'Type','axes'),'FontSize',16,'XColor','black','YColo
r','black');

figure
bode(C0,'k', C1,'b', C2,'r', opts1);
legend('Compensator n10','Compensator n20','Compensator n40');
h = findobj(gcf, 'Type','line');
set(h, 'LineWidth', 2);
set(findall(gcf,'Type','text'),'FontSize',20);
set(findall(gcf,'Type','axes'),'FontSize',16,'XColor','black','YColo
r','black');
```

Appendix 4.2 Simulink Models for the Verification of the H_∞ Optimized Compensators

Appendix 4.2.1 Simulink Models for the Verification of the H_∞ Optimized Compensators in the single mass-spring-damper based MiL system

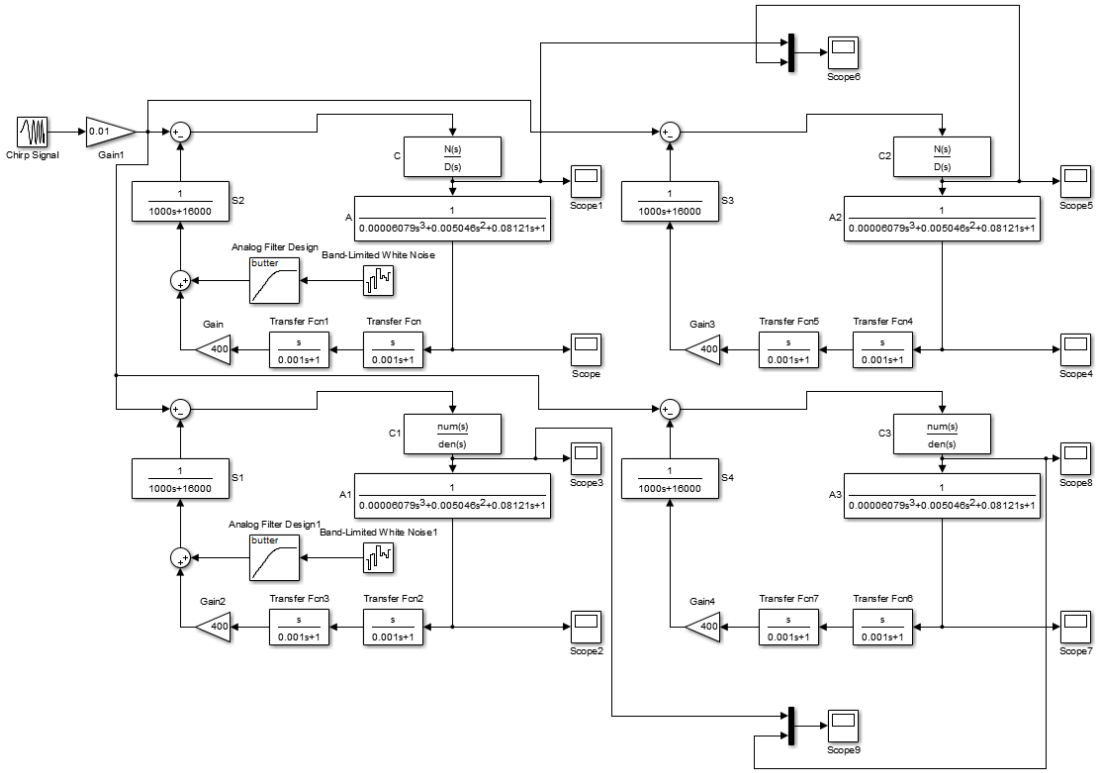

Figure A.7 The diagram of the Simulink model to verify the high frequency noise attenuation in the compensated signal z_{1c}

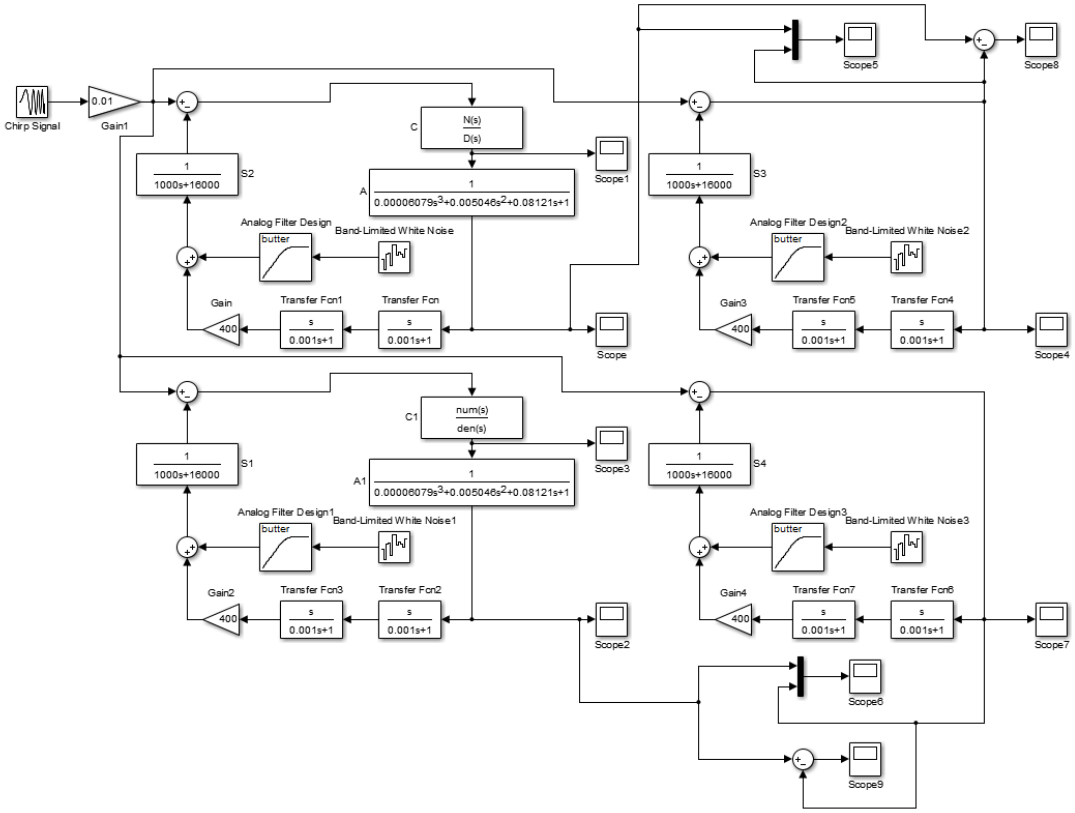

Figure A.8 The diagram of the Simulink model to verify the accuracy of the displacement z_1